Journal of Asian Earth Sciences 160 (2018) 460–489

Contents lists available at ScienceDirect

Journal of Asian Earth Sciences

journal homepage: www.elsevier.com/locate/jseaes

Full length article

Metasomatized asthenospheric mantle contributing to the generation of Cu-Mo deposits within an intracontinental setting: A case study of the ~128 Ma Wangjiazhuang Cu-Mo deposit, eastern North China Craton

Ting-Guang Lan[a,b,*], Rui-Zhong Hu[a,b], Xian-Wu Bi[a,b], Guang-Jian Mao[c], Bo-Jie Wen[d], Liang Liu[a], Ying-Hua Chen[b]

[a] State Key Laboratory of Ore Deposit Geochemistry, Institute of Geochemistry, Chinese Academy of Sciences, Guiyang 550081, China
[b] College of Earth Sciences, University of Chinese Academy of Sciences, Beijing 100049, China
[c] State Key Laboratory of Safe Ming and Clean Utilization of Coal Resources, Beijing 100013, China
[d] Research Center for Strategy of Global Mineral Resources, Chinese Academy of Geological Sciences, Beijing 100037, China

ARTICLE INFO

Keywords:
Cu-Mo deposit
LA-ICP-MS analysis of fluid inclusion
Asthenospheric mantle
Intracontinental setting
North China Craton

ABSTRACT

Cu-Mo deposits are commonly associated with calc-alkaline porphyries and derived from subduction-modified lithosphere in magmatic arcs. Here we report the Wangjiazhuang Cu-Mo deposit, which is peculiarly associated with an alkaline quartz monzonite that originated from a metasomatized asthenospheric mantle within an intracontinental setting in the eastern North China Craton (NCC). The deposit was formed at ca. 128.3 ± 0.7 Ma (2σ), basically coincident with the emplacement of the host quartz monzonite (128.8 ± 1.0 Ma, 2σ). Pegmatitic vein-type and stockwork-/disseminated-type mineralizations were identified in the deposit, of which the former is shallowly situated and characterized by coarse and well-crystallized Cu- and Mo-bearing sulfides + quartz + biotite + K-feldspar assemblages, whereas the latter is deeply situated and characterized by stockworks or Cu- and Mo-bearing sulfides disseminated in the altered quartz monzonite. Separation between Cu-rich and Mo-rich ore bodies at shallow depth was also observed. The Cu-Mo mineralization is typically associated with potassic-silicic alteration. High-temperature fluid inclusions with halite/sylvite daughter minerals (having homogenization temperatures of 287–466 °C and salinities of 33.8–55.3 wt% NaCl equivalent) suggest a magmatic origin of the ore-forming fluids. Differentiation of the fluids into vapor-rich and liquid-rich phases occurred during the magmatic-hydrothermal processes, as indicated by the coexistence of vapor-rich, liquid-rich and daughter mineral-rich fluid inclusions with similar homogenization temperatures. LA-ICP-MS analysis of the fluid inclusions shows that Cu is highly partitioned into the vapor-rich fluid inclusions, whereas Mo is mainly concentrated in the daughter mineral-rich fluid inclusions. This implies that phase differentiation of the ore-forming fluids was likely responsible for the separation of Cu-rich and Mo-rich ore bodies. The presence of hematite in the fluid inclusions also suggests high oxidation state of the ore-forming fluids. Based on the variations of $\delta^{34}S$ in sulfides and Al contents in quartz, continuous reduction of the oxidized ore-forming fluids, coupled with pH change of the fluids during water-rock interaction, led to the deposition of the ore-forming metals.

The host quartz monzonite shows adakitic geochemical signatures. Fractional crystallization of low-Mg amphiboles contributed to the adakitic signatures. According to the mixing modeling using Sr-Nd isotopes, the quartz monzonite was mainly derived from asthenospheric mantle-derived magma mixed by ~15–20% lower crust components at the base of the lower crust. Zircon saturation thermometry and Ti-in-quartz thermobarometer suggest that the rock was emplaced at the temperature of ~746 °C and the depth of ~4 km. High water ($H_2O \geq 4$ wt%) and metal (Cu is up to 840 ppm and Mo is up to 11.9 ppm) contents as well as high oxidation state (f_{O2} > fayalite-magnetite-quartz oxygen buffer) are featured in the quartz monzonite, indicating that the asthenospheric mantle source had been hydrated and oxidized by the water released from the stagnant Paleo-Pacific slab in the transition zone (410–610 km). Such modification by the deep stagnant oceanic slab beneath the eastern NCC thus not only triggered the remarkable thinning of the Archean lithospheric keel (loss

* Corresponding author at: State Key Laboratory of Ore Deposit Geochemistry, Institute of Geochemistry, Chinese Academy of Sciences, Guiyang 550081, China.
E-mail address: lantingguang@126.com (T.-G. Lan).

http://dx.doi.org/10.1016/j.jseaes.2017.07.014
Received 11 April 2017; Received in revised form 8 July 2017; Accepted 11 July 2017
Available online 14 July 2017

of > 120 km), but also promoted the asthenospheric mantle to become the favorable magma and metal source for the Cu-Mo deposits in the study region.

1. Introduction

The mineralizations of valuable metals such as Cu and Mo have long been the focus of geological studies. However, because of the complex magmatic to hydrothermal processes and the variable geological settings associated with the ore deposits, their origins remain controversial. As the most important holders of Cu and Mo reserves, porphyry Cu (Mo) deposits were broadly considered to be associated with calc-alkaline rocks that were derived from subduction-modified lithosphere and thus they typically occur in magmatic arcs (Richards, 2003, 2011a; Cooke et al., 2005; Sillitoe, 2010; Wilkinson, 2013). It has been well understood that in subduction settings the subducted oceanic slabs can effectively transport water and oxidative seafloor materials into the mantle wedge, which metasomatize the mantle wedge and thus facilitate the generation of calc-alkaline magmas with high metal, water and sulfur contents as well as high oxidation state (f_{O2}) (Mungall, 2002; Richards, 2011a, 2015a, 2015b; Wilkinson, 2013). Such magmas are favored for producing porphyry Cu (Mo) deposits. It is questioned that, however, since more and more porphyry or porphyry-like Cu (Mo) deposits were identified in non-arc settings, such as in collisional (e.g., Richards, 2009, 2011a, 2015a, 2015b; Qin et al., 2012; Hou et al., 2015; Hou and Zhang, 2015), post-collisional (e.g., Berzina et al., 2011; Qin et al., 2012; Mao et al., 2014; Yang et al., 2014; Hou and Zhang, 2015; Chen et al., 2017) and intracontinental extensional environments (e.g., Wang et al., 2006; Mao et al., 2011; Dong et al., 2013; Li and Santosh, 2014; Pirajno and Zhou, 2015), how did these non-arc related deposits originate? What were the essential factors controlling the generation of these Cu (Mo) deposits? Former studies revealed that the non-arc related metallogeny is quite complex, probably involving various processes or sources such as partial melting of the orogenically thickened crust, the previously subduction-modified lithosphere and the upwelling asthenosphere (Richards, 2009, 2011a, 2015a, 2015b). Therefore, while the formation of the arc-related Cu (Mo) deposits is well constrained, the non-arc related metallogeny is less understood and needs more attentions.

Lithospheric thinning is one of the most remarkable geological events occurring in North China Craton (NCC) during the Mesozoic (Gao et al., 2009; Xu et al., 2009; Zhu et al., 2012a, 2012b), which not only led to the significant loss of the Archean lithospheric keel (loss of > 120 km, Menzies et al., 1993; Griffin et al., 1998; Fan et al., 2000), but also resulted in extensive magmatism (Wu et al., 2005; Yang et al., 2008; Zhang et al., 2013) and abundant mineralizations (Mao et al., 2011, 2014; Zhai and Santosh, 2013; Li and Santosh, 2014; Pirajno and Zhou, 2015). The mineralizations include hydrothermal Au deposits, skarn Fe deposits, porphyry and porphyry-skarn Cu ± Mo ± Au and Mo deposits and hydrothermal Pb-Zn deposits (Yang et al., 2003; Mao et al., 2011, 2014; Li et al., 2012; Li and Santosh, 2014; Pirajno and Zhou, 2015). It is noted that the mineralizations mainly took place during the early Cretaceous, which were coeval with the developments of I- to A-type granites, alkaline rocks, bimodal volcanics, mafic dike

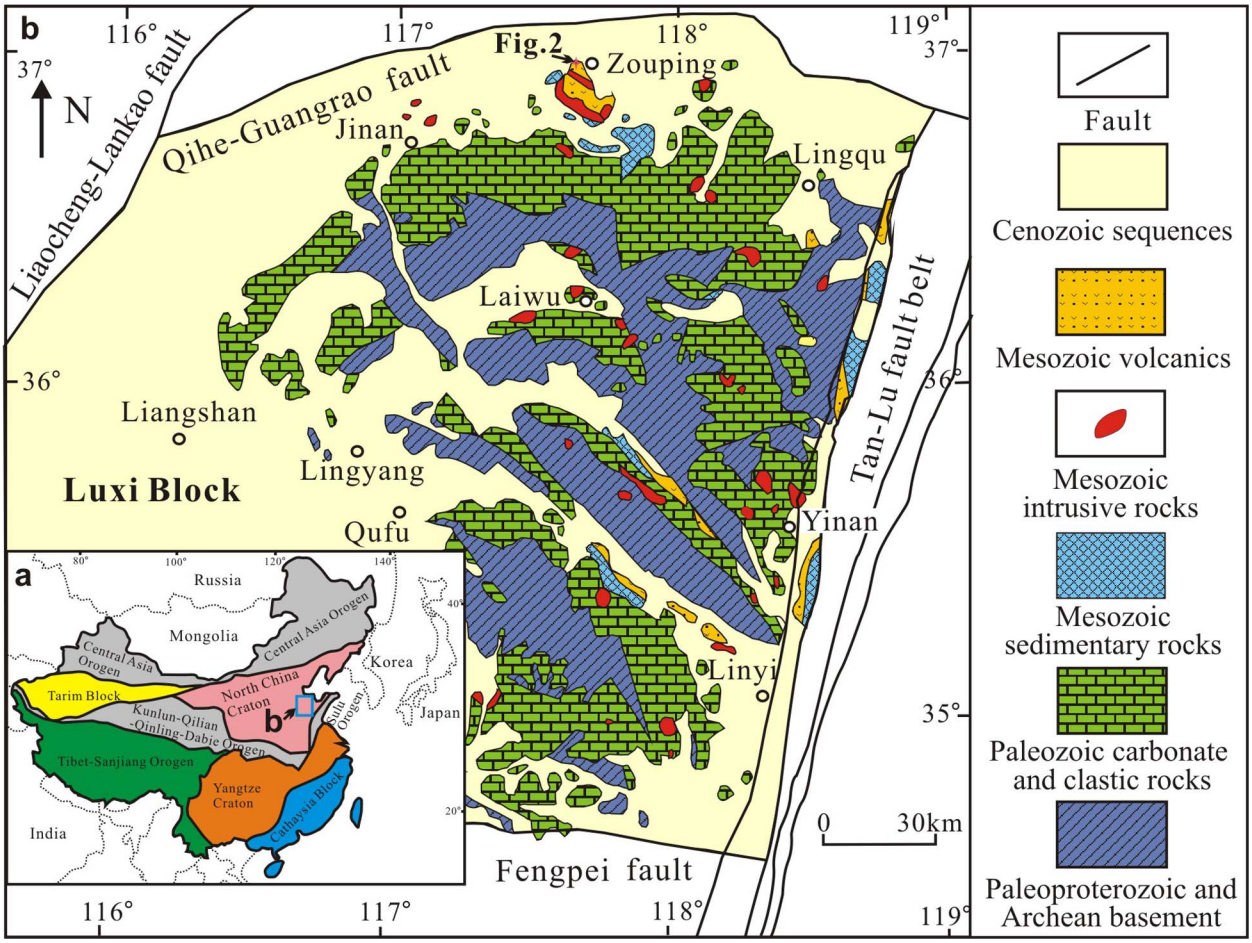

Fig. 1. (a) Tectonic subdivision of China (modified after Mao et al., 2011) and (b) Geological map of the Luxi Block (modified after Zhang et al., 2007).

swarms, carbonatite dikes, metamorphic core complexes and rift basins, strongly indicating an intracontinental extension (Ren et al., 2002; Wu et al., 2005; Windley et al., 2010; Li et al., 2012; Pirajno and Zhou, 2015). Therefore, the mineralizations have been referred to the products of lithospheric thinning within an intracontinental setting (Yang et al., 2003; Li et al., 2012; Zhai and Santosh, 2013; Li and Santosh, 2014; Pirajno and Zhou, 2015), although the geodynamic force was commonly considered to be associated with the westward subduction of the Paleo-Pacific (or Izanagi) plate (Gao et al., 2013; Mao et al., 2011, 2014; Ouyang et al., 2013; Li and Santosh, 2014; Pirajno and Zhou, 2015). In recent years, the porphyry and porphyry-skarn deposits in the NCC attracted more and more attentions due to their wide distribution in such a unique tectocnic setting. However, their genesis are still hotly debated, with various sources or processes such as continental crust, oceanic slab, enriched lithospheric mantle and crust-mantle interaction proposed for them (e.g., Mao et al., 2011, 2014; Gao et al., 2013; Ouyang et al., 2013; Li and Santosh, 2014; Pirajno and Zhou, 2015; Wang et al., 2015).

The early Cretaceous Wangjiazhuang Cu-Mo deposit is a porphyry-like Cu-Mo deposit situated at the Luxi Block of the eastern NCC (Fig. 1). It is interesting that this deposit shows similarities to porphyry deposits in aspects of alteration types (such as potassic, silicic, sericitic and kaolinitic alterations), mineralization styles (stockwork-/disseminated-type mineralization) and ore-forming fluids (characterized by high temperature, salinity and oxidation state), but has distinctive characteristics of being associated with an alkaline quartz monzonite (not a calc-alkaline porphyry) and containing pegmatitic vein-type mineralization. Several studies have been conducted on the deposit geology (e.g., Yuan and Li, 1988; Tang, 1990; Li and Yuan, 1991; Kong et al., 2006), the ore-forming fluids (e.g., Zhang et al., 2008a; Liu et al., 2013b), the mineralization age (e.g., Liu et al., 2013a; Wang et al., 2015) and the geochemistry of the host granitoid (e.g., Zhang et al., 2008b; Wang et al., 2015). However, the lack of systematic studies on the magma and metal sources as well as on the physico-chemical conditions of the magmatic-hydrothermal systems leaves the genetic processes of the deposit poorly constrained. Therefore, in this contribution, we carried out comprehensive and integrated studies on geochronology (zircon U-Pb and molybdenite Re-Os dating), geochemistry (major and/or trace element analyses on whole rock, zircon and quartz), radioactive and stable isotopes (Sr-Nd-Hf-He-Ar-S) and fluid inclusions (Raman spectroscopy, microthermometry and LA-ICP-MS analyses) of the ore-forming granitoid as well as the ore bodies, with aims to: (1) constrain the source and physico-chemical conditions (e.g., temperature, pressure and oxidation state) of the ore-forming granitoid; (2) investigate the characteristics of the ore-forming fluids and the sources of the metals; (3) discuss the specific magmatic-hydrothermal processes giving rise to the Cu-Mo mineralization; and (4) finally reveal the basic factors controlling the generation of the Cu-Mo deposits within an intracontinental setting.

2. Regional geology

The North China Craton (NCC), having Archean cores of 2.5–3.8 Ga and covering an area of 1,500,000 km^2, is the oldest and largest craton in China (Zhao et al., 2001) (Fig. 1a). The craton is mainly constituted by a basement of Archean to Paleoproterozoic tonalitic-trondhjemitic-granodioritic (TTG) gneisses and greenschist to granulite facies volcano-sedimentary rocks and a cover of Paleo-Mesoproterozoic to Ordovician volcano-sedimentary rocks, Carboniferous to Permian terrestrial clastic rocks, and Mesozoic basin sediments. Amalgamation among Archean micro-continental blocks before the Mesoproterozoic led to the final cratonization of the NCC (Zhai and Santosh, 2011; Zhao et al., 2012). After its cratonization, the NCC remained largely stable until the Mesozoic, prior to the remarkable thinning and large-scale replacement of the lithosphere (also referred to craton destruction, Gao et al., 2009; Xu et al., 2009; Zheng, 2009; Zhang et al., 2013; Zhu et al., 2012a, 2012b). Multiple subduction and collisional events surrounding the NCC, such as the northward subduction of the Paleo-Tethys ocean below the southern margin of the NCC during Devono-Carboniferous and Permo-Triassic (Meng and Zhang, 2000), the southward subduction of the Paleo-Asian Ocean below the northern margin of the NCC during Ordovician and Permo-Triassic (Xiao et al., 2003), and the westward subduction of the Paleo-Pacific Plate underneath the eastern Asian continent during Mesozoic, probably contributed to the craton destruction, of which the last one was considered to play the dominant role (Xu et al., 2009; Windley et al., 2010; Zhu et al., 2012a, 2012b).

The Luxi Block is located at the eastern part of the NCC and is bounded by the Tan-Lu fault to the east, the Liaocheng-Lankao fault to the west, the Qihe-Guangrao fault to the north, and the Fengpei fault to the south (Fig. 1b). The Tan-Lu fault, extending deeply into the mantle and acting as a conduit for asthenospheric upwelling (Chen et al., 2006, 2008; Xiao et al., 2010), not only contributed to the remarkable thinning of the lithosphere (Chen et al., 2006, 2008), but also controlled the emplacement of the widespread igneous rocks in the study area (Qiu et al., 2000; Ren et al., 2002). Various late Mesozoic intrusive rocks (Fig. 1b), including gabbros, high-Mg diorites, high-K calc-alkaline to alkaline rocks, granites, mafic dykes and carbonatites, widely occurred in the Luxi Block (Ying et al., 2004; Liu et al., 2008a; Xu et al., 2008; Lan et al., 2011b, 2013; Yang et al., 2012; Yang et al., 2012a, 2012b). Contemporaneous basalts to rhyolites were also developed (Qiu et al., 2000; Zhang et al., 2002; Li et al., 2008), mainly distributed in the Mesozoic volcanic basins and within the Tan-Lu fault belt (Fig. 1b). The high-Mg diorites and alkaline rocks commonly originated from crust-mantle interaction (Xu et al., 2008; Lan et al., 2011b, 2013; Yang et al., 2012; Yang et al., 2012a, 2012b; Chen et al., 2013), which were prone to produce Fe, Au and REE mineralizations (Qiu et al., 2000; Kong et al., 2006; Lan et al., 2011a).

3. Deposit geology

The Wangjiazhuang Cu-Mo deposit is located at the Zouping volcanic basin, northern Luxi Block (Fig. 1b). Early Cretaceous volcanic strata, which cover an area of ~400 km^2 and mainly consist of K-rich basalts to andesites (thickness > 5 km), occurred in the volcanic basin (Yuan and Li, 1987; Li et al., 2008). At least three independent eruption centers have been identified, in which ringed and radial faults were developed (Yuan and Li, 1987). The Wangjiazhuang deposit is situated at one of the calderas and hosted by a zoned intrusive complex which shows lithologies varying from diorite (~1 km^2) and monzonite (~0.5 km^2) to quartz monzonite (~5.5 km^2) (Fig. 2a) (Yuan and Li, 1987; Kong et al., 2006). Cu-Mo orebodies exclusively occur in the altered quartz monzonite (Fig. 2). The fresh quartz monzonite has an off-white color and a moderate-grained texture (Fig. 3a). It is mainly composed of plagioclase (~45 vol%), K-feldspar (~35 vol%), quartz (~15 vol%) and biotite (~5 vol%) with accessory zircon, magnetite and sphene (Fig. 3b). Notably, from the diorite and the monzonite towards the quartz monzonite, the timing of the intrusions becomes younger while the Cu and Mo concentrations in the corresponding rocks increase (Li and Yuan, 1991; Kong et al., 2006).

Hydrothermal alterations overprinting on the quartz monzonite are intense, mainly including potassic, potassic-silicic and silicic alterations (Fig. 2a). Sericitization, chloritization and kaolinitization occur locally (Fig. 2b). The potassic alteration (early potassic alteration), characterized by potassic feldspathization with a typical red[1] color (Fig. 3c), is the most widespread alteration in the central domain of the quartz monzonite (Fig. 2). Micro- to fine-grained pyrite is sporadically disseminated in this type of alteration. In addition, the alteration is in places overprinted by sericitic alteration, leading to the breakdown of

[1] For interpretation of color in Figs. 3 and 12, the reader is referred to the web version of this article.

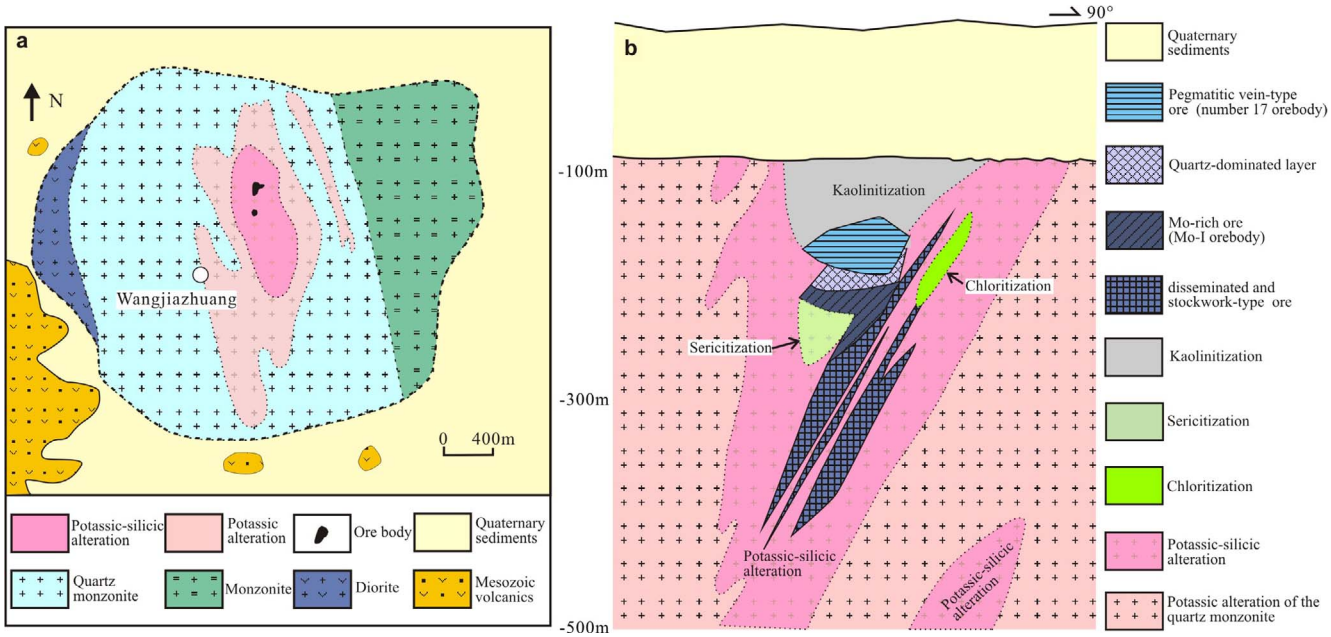

Fig. 2. (a) Geological map of the Wangjiazhuang deposit (modified after Yuan and Li, 1988) and (b) the Geological section along the No. 15 Exploration Line (modified after Tang, 1990).

K-feldspar (Fig. 3d). Potassic-silicic alteration (late potassic alteration) mainly shows as K-feldspar + quartz + biotite ± sulfides assemblages/veins, cutting or metasomatizing the early potassic alteration (Fig. 3e). The appearance of abundant quartz and biotite distinguishes it from the early K-feldspar-dominated potassic alteration. Silicic alteration is characterized by quartz ± sulfides stockworks or veins (Fig. 3f), overprinting on the potassic or potassic-silicic alteration. Kaolinitization is situated at the uppermost part of the intrusion (Fig. 2b) and seems to be produced by supergene processes (Yuan and Li, 1988). It is noted that the potassic-silicic alteration is the most important alteration associated with the Cu-Mo mineralization.

Twenty-eight orebodies divided into two types of mineralization have been observed, of which the number 17 orebody represents the pegmatitic vein-type mineralization while the others represent stockwork-/disseminated-type mineralization (Fig. 2b). The pegmatitic vein-type mineralization is characterized by coarse and well-crystallized chalcopyrite + molybdenite + quartz + biotite + K-feldspar assemblages (Fig. 3g and h). This type of mineralization is remarkably enriched in Cu and holds ~86% of the total Cu metal reserves, with the Cu grade ranging from 0.97 to 17.03% (commonly 6.19–9.05%) (Kong et al., 2006). The metals of Mo, Au and Ag are also abundant, showing the highest grade up to 0.86%, 13.67 g/t and 84.98 g/t, respectively (Kong et al., 2006). The number 17 orebody is horizontally situated with ~100 m in length, ~90 m in width and < 33 m in thickness (Kong et al., 2006). This orebody transitionally becomes a Mo-rich orebody (named as Mo-I orebody) through an ore-barren quartz-dominated layer (Fig. 2b). The Mo-rich orebody has average Mo and Cu grades of 0.34% and 0.36%, respectively (SXLLAF, 2010). Other orebodies in the form of stockwork-/disseminated mineralization are generally situated below the pegmatitic vein mineralization with steeper dip angles (50–65°) (Fig. 2b). The stockwork-/disseminated-type mineralization occurs as molybdenite and Cu-bearing sulfides disseminated in the altered quartz monzonite (Fig. 3i) or as molybdenite + Cu-bearing sulfides stockworks cutting the altered quartz monzonite. The ore bodies are generally 100–350 m in length, 50–200 m in width and 2–35 m in thickness. They have relatively low Cu and Mo grades, showing Cu grade of 0.51–1.15% and Mo grade of < 0.1% respectively (Kong et al., 2006; SXLLAF, 2010). Apart from the major ore minerals of chalcopyrite, bornite, tennantite, enargite and molybdenite (Fig. 3j–l), other Cu-bearing minerals such as chalcocite, azurite and malachite can be sporadically found. Gangue minerals mainly include K-feldspar, quartz, biotite and sericite. Based on the cross-cutting relationships, two main stages of hydrothermal veins are distinguished, of which the early stage is the ore-forming stage and represented by the Cu- and Mo-bearing pegmatitic veins, whereas the late stage is the post-mineralization stage and represented by the ore-barren quartz veins.

4. Analytical methods

With the aim of detailedly investigating the magmatic-hydrothermal processes of the Wangjiazhuang Cu-Mo deposit, all kinds of high-precise analytical methods were invoked in this study. Zircon U-Pb dating by laser ablation inductively coupled plasma mass spectrometry (LA-ICP-MS) and molybdenite Re-Os isotopic analyses by ICP-MS were used to determine the intrusive age of the ore-forming granitoid and the mineralization age of the deposit, respectively. Trace element analyses of zircon and quartz by LA-ICP-MS were applied to determine the oxidation state and the emplacement temperature and pressure of the host granitoid. Whole-rock major element analyses by X-ray fluorescence spectroscopy (XRF) and trace element analyses by ICP-MS were used to determine the geochemical characteristics of the granitoid and the altered counterparts. Zircon Hf isotopic analyses by laser ablation multi-collector ICP-MS (LA-MC-ICP-MS) and Sr-Nd isotopic analyses by thermal ionization mass spectrometry (TIMS) were used to trace the source materials of the granitoid. Raman spectroscopic and microthermometric analyses coupled with LA-ICP-MS analyses on fluid inclusions were conducted to reveal the characteristics and the evolutional processes of the ore-forming fluids. S and He-Ar isotopic analyses on sulfides by mass spectrometry were also used to trace the sources of the ore-forming metals/fluids.

4.1. U-Pb dating, trace element and Hf isotopic analyses of zircon by LA-(MC)-ICP-MS

In order to identify internal textures and to choose potential target sites for U-Pb dating and Hf isotopic analyses, cathodoluminescence (CL) images of zircons were obtained using a LEO1450VP scanning electron microscope at the Institute of Geology and Geophysics, Chinese Academy of Sciences (IGGCAS), Beijing, China. The working conditions were at 15 kV accelerating voltage and 20 nA beam current.

Zircon grains selected from the fresh quartz monzonite (13ZP01) were used for in-situ U-Pb dating, trace element and Hf isotopic

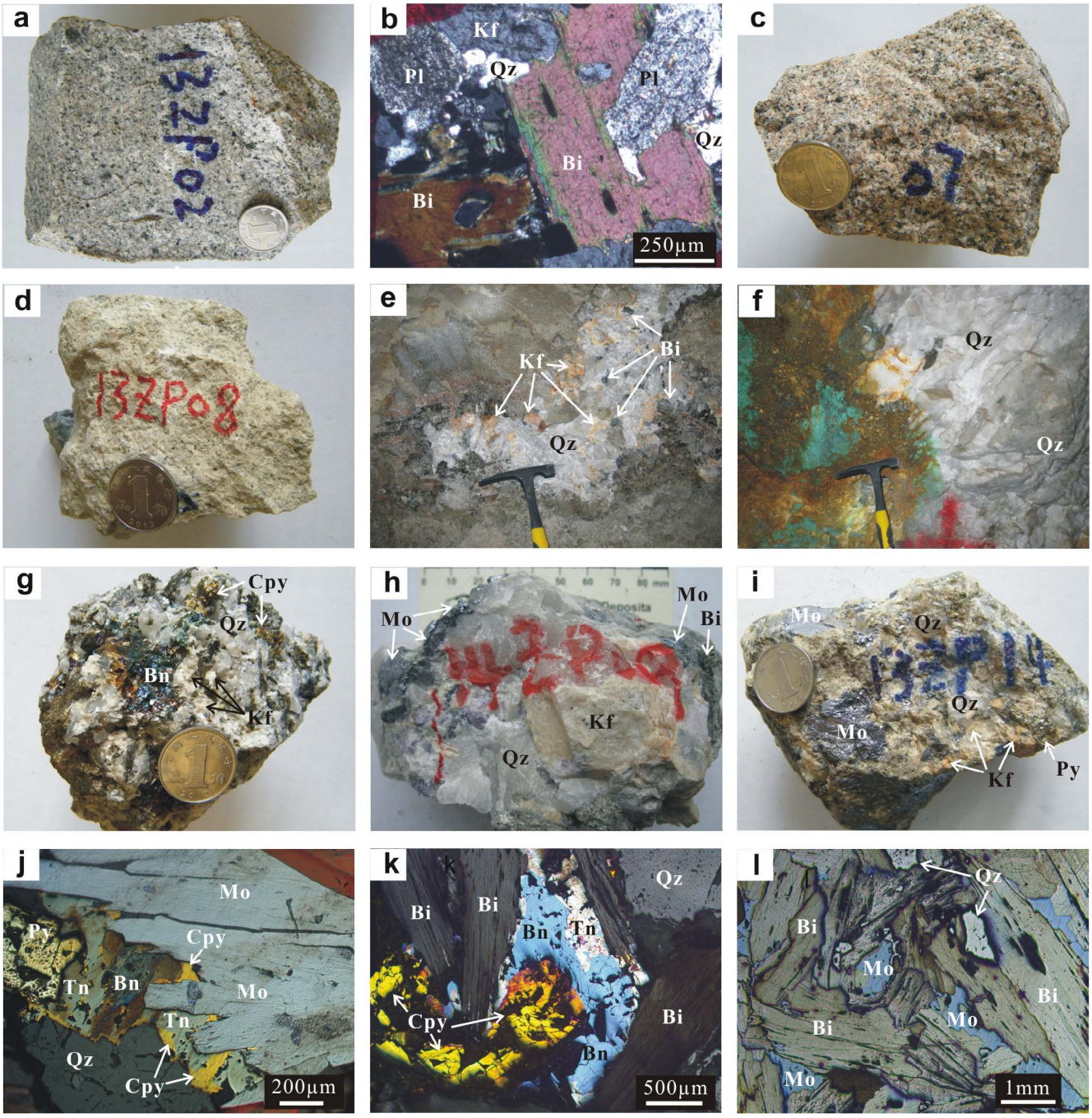

Fig. 3. Photos and microphotographs of representative rock and ore samples from the Wangjiazhuang deposit. (a) Fresh quartz monzonite. (b) Major minerals of the quartz monzonite. (c) and (d) Potassic and sericitic alterations of the quartz monzonite, respectively. (e) Potassic-silicic alteration, expressed as Kf + Qz + Bi vein. (f) Silicic alteration, expressed as Qz vein. (g) Vein-type ores showing coarse and well-crystallized Qz + Kf + Cpy + Bn assemblages. (h) Pegmatitic vein-type ores showing Qz + Kf+ +Bi + Mo assemblages. (i) Coarse Mo and Py disseminated in the altered quartz monzonite. (j) Mineral assemblages of Mo + Cpy + Bn + Tn + Qz; (k) Mineral assemblages of Cpy + Bn + Tn + Bi + Qz. (l) Mineral assemblages of Mo + Bi + Qz. Abbreviations: Pl, plagioclase; Kf, K-feldspar; Bi, biotite; Qz, quartz; Cpy, chalcopyrite; Py, pyrite; Bn, bornite; Tn, tennantite; Mo, molybdenite.

analyses. The U-Pb dating and trace element analyses were conducted synchronously by LA-ICP-MS at the State Key Laboratory of Ore Deposit Geochemistry, Institute of Geochemistry, Chinese Academy of Sciences (IGCAS), Guiyang, China. Laser sampling was performed using a GeoLasPro 193 nm ArF excimer laser. An Agilent 7900 ICP-MS was used to acquire ion-signal intensities. Each analyses incorporated a background acquisition of approximately 20 s (gas blank) followed by 50 s data acquisition from the sample. Helium was used as the carrier gas. Argon was used as the makeup gas and mixed with the carrier gas via a T-connector before entering the ICP. Laser spot size of 32 μm and repetition of 6 Hz were used during the analyses. Zircon 91500 was used as external standard for U-Th-Pb calibrations, and was analyzed twice every 5 analyses. NIST SRM610 was used as external standard for trace element calibrations, and was analyzed twice every 10 analyses. Combined with using Zr as internal standard, this method has the advantage to accurately measure the trace element concentrations in zircon (Liu et al., 2010). Off-line selection and integration of background and analyte signals, time-drift correction, and quantitative calibrations were performed by *ICPMSDataCal* (Liu et al., 2008b). Concordia diagrams and weighted mean calculations were made using *ISOPLOT* software (Ludwig, 2003). The preferred values of element concentrations for the NIST SRM610 are from the GeoReM database

Table 1
Summary of instruments, analytical conditions and reference materials used for the LA-(MC)-ICP-MS measurements.

Analyses item	Zircon Lu-Hf isotopes	Zircon U-Pb dating and elements	Elements in quartz	Fluid inclusion compositions
Laser ablation system				
Instrument	GeoLasPro 193 nm	GeoLasPro 193 nm	GeoLasPro 193 nm	GeoLasPro 193 nm
Energy density (J/cm^2)	8	8	10	10
Spot size (μm)	50	32	44	16–44
Repetition rate (Hz)	6	6	10	10
Cell gas flow (L/min, He)	0.8	0.6	0.6	0.6
ICP-MS				
Instrument	Neptune	Agilent 7900	Agilent 7900	Agilent 7900
RF power (W)	1300	1450	1450	1450
Cooling gas flow (L/min, Ar)	15	15	15	15
Makeup gas flow (L/min, Ar)	1.2	1.0	1.0	1.0
Integration/Dwell time (ms)	131	10–30	10–20	10–20
Monitored isotopes	^{172}Yb, ^{173}Yb, ^{175}Lu, ^{176}Lu, ^{176}Hf, ^{176}Yb, ^{177}Hf, ^{178}Hf, ^{179}Hf, ^{180}Hf, ^{180}W, ^{182}W	^{29}Si, ^{49}Ti, ^{89}Yb, ^{90}Zr, ^{139}La, ^{140}Ce, ^{141}Pr, ^{146}Nd, ^{147}Sm, ^{153}Eu, ^{157}Gd, ^{159}Tb, ^{163}Dy, ^{165}Ho, ^{166}Er, ^{169}Tm, ^{172}Yb, ^{175}Lu, ^{178}Hf, ^{204}Pb, ^{206}Pb, ^{207}Pb, ^{208}Pb, ^{232}Th, ^{235}U, ^{238}U	^{7}Li, ^{9}Be, ^{11}B, ^{23}Na, ^{24}Mg, ^{27}Al, ^{29}Si, ^{31}P, ^{39}K, ^{44}Ca, ^{45}Sc, ^{49}Ti, ^{51}V, ^{52}Cr, ^{55}Mn, ^{57}Fe, ^{59}Co, ^{60}Ni, ^{65}Cu, ^{66}Zn, ^{69}Ga, ^{72}Ge, ^{75}As, ^{77}Se, ^{85}Rb, ^{88}Sr, ^{89}Y, ^{90}Zr, ^{93}Nb, ^{98}Mo, ^{107}Ag, ^{118}Sn, ^{121}Sb, ^{133}Cs, ^{137}Ba, ^{139}La, ^{140}Ce, ^{141}Pr, ^{146}Nd, ^{147}Sm, ^{153}Eu, ^{157}Gd, ^{159}Tb, ^{163}Dy, ^{165}Ho, ^{166}Er, ^{169}Tm, ^{172}Yb, ^{175}Lu, ^{178}Hf, ^{181}Ta, ^{182}W, ^{197}Au, ^{205}Tl, ^{209}Bi, ^{208}Pb, ^{232}Th, ^{238}U	The same as analyzed in quartz
Reference materials	Mud Tank	91500 and NIST SRM610	NIST SRM610	NIST SRM610

(http://georem.mpch-mainz.gwdg.de/). Detailed data calibrations are referred to Liu et al. (2008b, 2010).

In-situ zircon Hf isotopic analyses were determined by a Neptune MC-ICP-MS equipped with a GeoLasPro 193 nm ArF excimer laser at the State Key Laboratory of Lithospheric Evolution, IGGCAS. Laser spot size of 50 μm and repetition of 6 Hz were used during the analyses. The MC-ICP-MS was operated in static mode with the integration for baseline of 30 s. The signal collection model is one block with 200 cycles. Each cycle has 0.131 s integration time and the total time is about 26 s during each analyses. Zircon Mud Tank was measured to monitor the accuracy of the analytical procedures, and was analyzed twice every 5 analyses. Repeated analyses of the Mud Tank yield a mean $^{176}Hf/^{177}Hf$ ratio of 0.282503 ± 32 (2SD), which is well consistent with the recommended values (0.282507 ± 6 by solution method and 0.282504 ± 44 by LA-MC-ICP-MS, Woodhead and Hergt, 2005). Detailed analytical procedures are described in Wu et al. (2006) and Xie et al. (2008).

An overview of the instruments, analytical conditions and reference materials used for the LA-(MC)-ICP-MS measurements is given in Table 1.

4.2. Major and trace element analyses of quartz and fluid inclusion by LA-ICP-MS

Quartz trace element analyses by LA-ICP-MS were conducted on the quartz samples selected from the host granitoid and the hydrothermal veins, whereas the fluid inclusion major and trace element analyses were only conducted on the quartz from the hydrothermal veins. All the quartz samples were prepared as surface-polished sections with thickness of ~300 μm. CL imaging was done to examine growth patterns and to distinguish different growth zones of the crystals. The analyses were also conducted at the State Key Laboratory of Ore Deposit Geochemistry, IGCAS by using the Agilent 7900 ICP-MS equipped with a GeoLasPro 193 nm ArF excimer laser. Laser repetition of 10 Hz and energy density of 10 J/cm^2 were used during the analyses. Laser spot size of 44 μm was used for the quartz trace element analyses, but was adjusted from 16 to 44 μm for the fluid inclusion analyses. For quartz trace element calibrations, external standard of NIST SRM610 was used and analyzed twice every 10 analyses. An internal standard-independent calibration strategy, which is based on the normalization of the sum of all metal oxides to 100 wt%, was applied to the quantitative calibrations by using the *ICPMSDataCal* software (Liu et al., 2008b). This strategy has been proved to work well for anhydrous minerals (Liu et al., 2008b). Standard glasses of NIST SRM612 and GSE-1G were analyzed to monitor the accuracy of the results, which show that the uncertainties of the elements that are probably present in quartz (such as Li, Na, Mg, Al, K, Ca, Sc, Ti, Cr, Ge, Rb and Sr) are less than 6%. For fluid inclusion major and trace element calibrations, the raw LA-ICP-MS data were reduced using the *SILLS* software (Guillong et al., 2008). NIST SRM610 was used as external standard and analyzed twice every 10 analyses. NaCl equivalent wt.% concentrations in the fluid inclusions, which were obtained independently from the microthermometry, were used as the internal standard (Heinrich et al., 2003). The charge-balance method was adopted to correct the modeled amounts of Na (from the NaCl eqv. wt%) for salinity contributions of other chloride salts (Allan et al., 2005). Synthetic fluid inclusions containing five elements of Na, K, Ca, Rb and Cs (standard values are Na = K = Ca = 2.05 wt%, Rb = 300 ppm, Cs = 200 ppm) were also analyzed to monitor the accuracy, which show the total uncertainties of less than 16%.

The instruments, analytical conditions and reference materials used for the above measurements are listed in Table 1.

4.3. Re-Os isotopic analyses

Six molybdenite samples selected from the pegmatitic vein-type and the disseminated-type mineralizations were used for Re-Os isotopic analyses. The analyses were carried out at the Re-Os Laboratory, National Research Center of Geoanalysis, Chinese Academy of Geological Sciences. Well crystallized molybdenite grains were hand-picked under a binocular microscope before being powdered for digestion. A Carius tube digestion method was used. The Re and Os contents and isotopic ratios were determined by TJA X-series ICP-MS. The detailed analytical procedures are described in Du et al. (2004). The Re-Os isochron age was calculated using the *ISOPLOT* software (Ludwig, 2003). The decay constant used in the age calculation is $\lambda^{187}Re = 1.666 \times 10^{-11}$ year^{-1} (Smoliar et al., 1996).

4.4. Whole-rock major and trace element analyses

Five fresh and four altered samples of the host quartz monzonite were selected for major and trace element analyses. The analyses were conducted at the IGGCAS. For major element analyses, 200 mesh whole-rock powders (~0.5 g) admixed with $Li_2B_4O_7$ + $LiBO_2$ (5 g) were fused into glass discs and analyzed by X-ray fluorescence spectroscopy (XRF) with an AXIOS Minerals spectrometer. The analytical uncertainties were within 0.1–1% (RSD). Ferrous iron (Fe^{2+}) was analyzed independently by using dichromate method. For trace element analyses, whole-rock powders (~40 mg) were dissolved in distilled HF + HNO_3 mixture in Teflon screw-cap capsules at 200 °C for 5 days, dried, and then digested with HNO_3 at 150 °C for 1 day. The final step was repeated once. Dissolved samples were diluted to 49 ml with 1% HNO_3 and 1 ml 500 ppb indium was added to the solution as an internal standard. Trace element abundances were determined by ICP-MS using an ELEMENT spectrometer. Accuracy is better than 5% for most of the elements as evaluated from the Chinese granite (GSR1) and basalt (GSR3) standards.

4.5. Whole-rock Sr-Nd isotopic analyses

Four samples of the fresh quartz monzonite were selected for Sr-Nd isotopic analyses. Whole-rock powders (200 mesh) were dissolved in Teflon screw-cap capsules after being spiked with ^{87}Rb, ^{84}Sr, ^{149}Sm and ^{150}Nd tracers prior to HF + HNO_3 + $HClO_4$ dissolution. Rb, Sr, Sm and Nd were separated using conventional ion exchange procedures and measured using a Finnigan MAT262 multi-collector mass spectrometer at the IGGCAS. Procedural blanks are < 100 pg for Sm and Nd and < 300 pg for Rb and Sr. The isotopic ratios were corrected for mass fractionation by normalizing to $^{86}Sr/^{88}Sr = 0.1194$ and $^{146}Nd/^{144}Nd = 0.7219$, respectively. The measured values for the JNdi-1 Nd standard and NBS987 Sr standard were $^{143}Nd/^{144}Nd = 0.512108 \pm 11$ (2SD, n = 5) and $^{87}Sr/^{86}Sr = 0.710256 \pm 11$ (2SD, n = 5), respectively. USGS reference material BCR-2 was measured to monitor the accuracy of the analytical procedures, with the following results: $^{143}Nd/^{144}Nd = 0.512633 \pm 13$ and $^{87}Sr/^{86}Sr = 0.705035 \pm 12$ (2SD, n = 5). The $^{87}Sr/^{86}Sr$ and $^{143}Nd/^{144}Nd$ data of the BCR-2 show good agreement with previously published data by TIMS and MC-ICP-MS techniques (Yang et al., 2010). Detailed analytical procedures are similar to those described in Yang et al. (2010).

4.6. Sulfur isotopic analyses

Two major generations of sulfides were identified in the Wangjiazhuang deposit, of which the first generation represents the potassic alteration and the second generation represents the Cu-Mo mineralization. Four pyrite samples of the first generation and thirteen pyrite, chalcopyrite and molybdenite samples of the second generation were selected for sulfur isotopic analyses. The analyses were conducted at the State Key Laboratory of Ore Deposit Geochemistry, IGCAS. Pure sulfide powders were in-situ sampled using a microdrill sampling system (RELION MSS VI). The powders of sulfides were wrapped in tin capsules and flash-combusted in a single reactor filled with WO_3 and Cu

as reducing agents, liberating SO_2 during interaction with an O_2-enriched He gas. Isotopic measurements were conducted in a continuous-flow isotope ratio mass spectrometer (MAT253). International reference standards of IAEA-S-1, IAEA-S-2 and IAEA-S-3 were used as external standards, with the analytical precision better than ± 0.2‰. The S isotopic composition is expressed against the Canyon Diablo troilite (CDT).

4.7. He-Ar isotopic analyses

Four pyrite and chalcopyrite samples from the Cu-Mo mineralization stage were selected for He-Ar isotopic measurements. The measurements were carried out using a GV 5400 mass spectrometry at the State Key Laboratory of Ore Deposit Geochemistry, IGCAS. The sensitivities of the GV5400 for He and Ar were 3.9725×10^{-4} A/Torr and 1.1018×10^{-3} A/Torr, respectively. Pure and coarse sulfide grains (500–1000 mg with sizes of 0.5–1.5 mm) were hand-picked and cleaned before being loaded on-line into vacuum crusher buckets. The samples were baked at 120–150 °C in the crusher buckets for ca. 24 h to remove adhered atmospheric gases. The gases were released by sequential crushing of the sulfide grains in high-vacuum conditions. He and Ar isotopic compositions and abundances were calibrated against pipettes of 0.1 cm^3 STP air (5.2×10^{-7} cm^3 STP ^{4}He and 9.3×10^{-4} cm^3 STP ^{40}Ar). Procedural blanks were $< 2 \times 10^{-10}$ cm^3 STP ^{4}He and $(2–4) \times 10^{-10}$ cm^3 STP ^{40}Ar. The detailed analytical procedures are described in Hu et al. (2012).

4.8. Raman spectroscopy and microthermometry of fluid inclusion

Representative doubly polished quartz samples selected from the hydrothermal veins, especially from the pegmatitic vein-type mineralization, were used for fluid inclusion Raman microspectroscopic and microthermometric analyses. Due to the lack of quartz with suitable fluid inclusions, no fluid inclusion study was conducted for the stockwork-/disseminated-type mineralization.

All the analyses were carried out after detailed petrographic observations. The Raman spectroscopic analyses were conducted using the LabRam HR800 Raman microspectrometer at the IGGCAS. An argon ion laser with a wavelength of 532 nm and a source power of 44 mW was used in detection.

Microthermometric measurements were carried out using a Linkam THMSG 600 programmable heating-freezing stage equipped with a Leitz microscope at the IGGCAS. The stage was calibrated using synthetic fluid inclusions supplied by FLUID INC. Calibrations against the triple-point of pure CO_2 (−56.6 °C), the freezing point of water (0.0 °C) and the critical point of water (374.1 °C) were done. The heating rate of 0.1–0.2 °C/min was adopted near phase transformation. The precision of measurement was ± 0.2 °C at the freezing temperature and ± 2 °C at the homogenization temperature.

5. Results

5.1. Intrusive age of the host quartz monzonite

Zircon crystals of the host quartz monzonite (sample 13ZP01) mainly range from 50 to 150 μm in size, with length to width ratios of 1:1–2:1. Most of them are subhedral and gray in CL images. The zircons commonly show wide oscillatory zoning in the core and narrow zoning towards the rim (Fig. 4a). Notably, the oscillatory zoning is also accompanied by sector zoning (Fig. 4a), which may reflect unstable crystallization environment resulting in different growth velocities of crystal facies in zircons (Vavra et al., 1996; Wu and Zheng, 2004). Nonetheless, twenty analyses from twenty zircon grains are quite concordant, plotting on the concordia with a weighted mean $^{206}Pb/^{238}U$ age of 128.8 ± 1.3 Ma (2σ) (Fig. 4b and Table 2). This age is therefore interpreted as the intrusive age of the quartz monzonite.

5.2. Timing of the Cu-Mo mineralization

Re-Os chronometer in molybdenite has been proved to be remarkably robust and thus provides one of the most powerful constraints on the mineralization ages of ore deposits (Stein et al., 1997, 2001). The Re-Os analytical results of six molybdenite samples from the Wangjiazhuang Cu-Mo deposit are listed in Table 3. There is no obvious difference in Re-Os contents and model ages between the pegmatitic vein-type and the disseminated-type mineralizations. All the samples have high Re contents of 177–364 ppm and low ^{187}Os contents of 0.24–0.49 ppm. They show model ages ranging from 127.8 to 128.9 Ma with a weighted mean age of 128.3 ± 0.7 Ma (2σ) (Fig. 5a) and construct a well constrained ^{187}Re-^{187}Os isochron age of 128.1 ± 1.9 Ma (2σ) (Fig. 5b). These ages are consistent with each other within errors, implying that the pegmatitic vein-type and the disseminated-type mineralizations occurred almost synchronously. Considering the weighted mean model age is better than the isochron age (Du et al., 2004), the age of 128.3 ± 0.7 Ma is thus interpreted as the mineralization age of the Wangjiazhuang deposit. This age is in accordance with previous studies which were just conducted on the vein-type mineralization (Liu et al., 2013a; Wang et al., 2015).

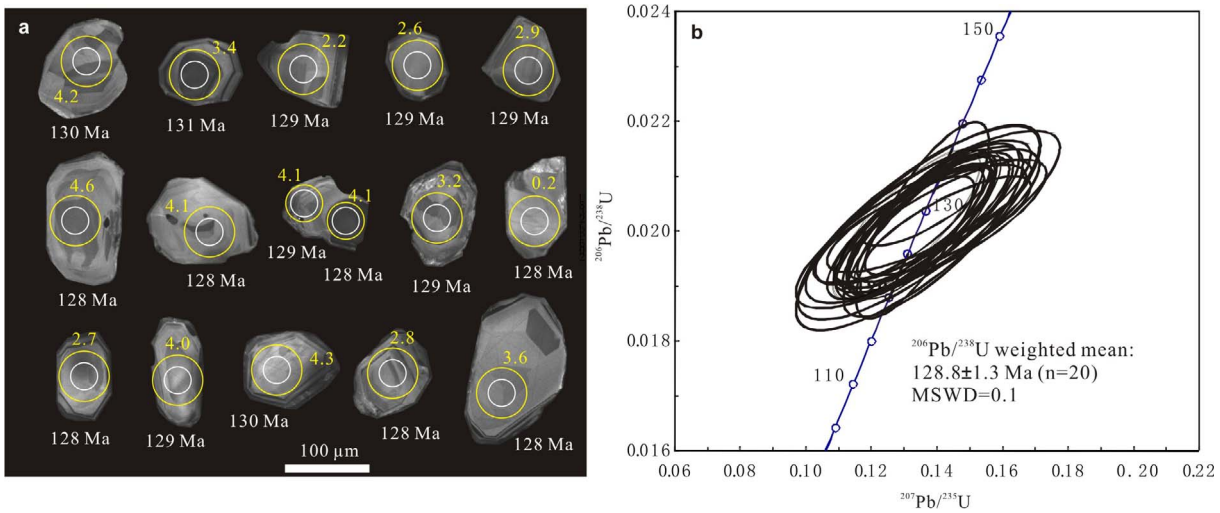

Fig. 4. (a) CL images and (b) concordia plot for U-Pb isotopic data of zircon grains from the quartz monzonite. Small circles in CL images refer to U-Pb dating by LA-ICP-MS, big circles relate to Hf isotopic analyses by LA-MC-ICP-MS.

Table 2
LA-ICP-MS zircon U-Th-Pb data for the quartz monzonite (13ZP01).

Spot	Concentrations (ppm)				Isotopic ratios				Isotopic ages (Ma)			
No.	Pb	Th	U	Th/U	$^{207}Pb/^{235}U$	1σ	$^{206}Pb/^{238}U$	1σ	$^{207}Pb/^{235}U$	1σ	$^{206}Pb/^{238}U$	1σ
1	6.35	218	218	1.00	0.1350	0.0128	0.0201	0.0007	128.6	11.4	128.5	4.4
2	3.50	105	124	0.84	0.1341	0.0245	0.0201	0.0010	127.8	22.0	128.1	6.0
3	3.28	107	115	0.93	0.1356	0.0134	0.0202	0.0012	129.1	12.0	128.9	7.5
4	3.99	95	154	0.62	0.1345	0.0144	0.0202	0.0009	128.2	12.9	128.7	5.5
5	3.84	125	133	0.94	0.1387	0.0256	0.0203	0.0010	131.9	22.8	129.4	6.5
6	4.27	132	155	0.85	0.1372	0.0185	0.0202	0.0009	130.5	16.5	128.9	5.9
7	4.51	135	159	0.85	0.1345	0.0153	0.0201	0.0008	128.1	13.7	128.3	5.4
8	3.72	108	134	0.80	0.1347	0.0215	0.0201	0.0007	128.4	19.2	128.6	4.5
9	8.89	262	317	0.83	0.1355	0.0174	0.0202	0.0008	129.0	15.6	128.8	5.1
10	3.04	96	108	0.89	0.1345	0.0243	0.0202	0.0012	128.2	21.8	128.7	7.4
11	2.92	75	106	0.71	0.1349	0.0189	0.0201	0.0009	128.5	16.9	128.3	5.6
12	2.57	79	96	0.83	0.1356	0.0150	0.0202	0.0008	129.1	13.4	128.7	5.3
13	2.95	81	109	0.75	0.1409	0.0214	0.0201	0.0008	133.9	19.1	128.3	5.1
14	6.05	241	196	1.23	0.1369	0.0150	0.0201	0.0009	130.3	13.4	128.6	5.7
15	3.58	134	124	1.08	0.1357	0.0217	0.0204	0.0009	129.2	19.4	129.9	5.5
16	4.18	117	154	0.76	0.1350	0.0150	0.0201	0.0007	128.6	13.4	128.3	4.7
17	4.21	126	160	0.78	0.1343	0.0247	0.0201	0.0012	127.9	22.1	128.1	7.8
18	4.65	158	172	0.92	0.1377	0.0207	0.0203	0.0007	131.0	18.5	129.5	4.2
19	3.42	94	132	0.72	0.1388	0.0180	0.0200	0.0010	132.0	16.1	127.7	6.5
20	4.15	119	159	0.74	0.1346	0.0146	0.0202	0.0007	128.3	13.0	128.8	4.3

5.3. Major and trace element compositions of the fresh and altered quartz monzonite

Major and trace elements analytical results are presented in Table 4. The fresh quartz monzonite has homogeneous major element contents, showing SiO_2 of 63.7–66.1 wt%, Al_2O_3 of 15.5–16.4 wt%, CaO of 2.37–3.28 wt%, K_2O of 4.09–4.43 wt%, Na_2O of 4.66–5.12 wt%, $Fe_2O_3^T$ of 3.77–4.18 wt%, MgO of 1.32–1.68 wt%, TiO_2 of 0.44–0.68 wt%) and P_2O_5 of 0.18–0.22 wt%, respectively. These features classify the granitoid into quartz monzonite in the R1-R2 discrimination diagram (Fig. 6a), consistent with the petrographic observations. In addition, it is chemically metaluminous according to the alumina saturation index (Fig. 6b). The high K_2O and Na_2O contents also suggest its alkaline affinity in both the SiO_2 vs. A.R. diagram of Wright (1969) (Fig. 6c) and the (Na_2O + K_2O-CaO) vs. SiO_2 diagram of Frost et al. (2001) (Fig. 6d).

The quartz monzonite is enriched in light rare earth elements (LREEs) and depleted in heavy rare earth elements (HREEs), showing strong fractionation between the LREEs and the HREEs ($(La/Yb)_N$ = 21.9–25.8) (Fig. 7a). It also has weak negative Eu anomalies (δEu = 0.81–0.97). On the primitive mantle-normalized spidergram, the quartz monzonite is characterized by significant depletion of high field strength elements (HFSEs, such as Nb, Ta, Zr, P and Ti) and enrichment of large ion lithophile elements (LILEs, such as Sr and Ba) (Fig. 7b).

Compared with the unaltered samples, the potassic alteration shows the obvious decrease of $Fe_2O_3^T$, MgO, CaO, Cr, Ni, Zn, Rb, Sr, Zr, Ba and Ce and the significant increase of K_2O, N_2O and Cu (Fig. 8a and b). In addition, from the potassic alteration to the sericitic alteration, losses of $Fe_2O_3^T$, MgO, CaO, Na_2O, Cr, Cu, Zn, Zr, Sr, Ba, La, Ce, Nd and Pb and gains of K_2O and Rb can be seen (Fig. 8c and d).

5.4. Major and trace element compositions in zircon and quartz

REEs and Ti are the useful elements in zircon, since they can be used to estimate the oxidation state (e.g., Ballard et al., 2002; Trail et al., 2011, 2012) and the crystallization temperature (e.g., Watson et al., 2006; Ferry and Watson, 2007; Watson and Harrison, 2005) of the host magma. For the zircon grains from the quartz monzonite, they are depleted in LREEs and enriched in HREEs with notable positive Ce and negative Eu anomalies (Table 5 and Fig. 9a). Based on the method of Trail et al. (2011, 2012), the intensity of Ce anomaly in zircon can be defined as $(Ce/Ce*)_D = \frac{D^{zrc/melt}_{Ce(total)}}{\sqrt{D^{zrc/melt}_{La} \times D^{zrc/melt}_{Pr}}}$, where $D^{zrc/melt}_{Ce}$ represents the concentrations of Ce in zircon to that of the melt, $D^{zrc/melt}_{La}$ and $D^{zrc/melt}_{Pr}$ are the partition coefficients for La and Pr. As a result, the calculated $(Ce/Ce*)_D$ ratios of the zircons from the quartz monzonite vary from 63 to 291. In addition, as an indicator of oxidation state, the Ce^{4+}/Ce^{3+} ratio in zircon can be calculated from $\frac{Ce_{melt} - \frac{Ce_{zircon}}{D^{zrc/melt}_{Ce^{3+}}}}{\frac{Ce_{zircon}}{D^{zrc/melt}_{Ce^{4+}}} - Ce_{melt}}$ (Ballard et al., 2002), where Ce_{zircon} and Ce_{melt} represent the Ce concentrations in zircon and melt, respectively, and $D^{zrc/melt}_{Ce^{3+}}$ and $D^{zrc/melt}_{Ce^{4+}}$ represent the

Table 3
Re-Os isotopic data of molybdenite for the Cu-Mo mineralization.

Sample	Description	Total Re (ppm)		^{187}Re (ppm)		^{187}Os (ppb)		Common Os (ppb)		Model age (Ma)	
		Value	Uncertainty	Value	Uncertainty	Value	Uncertainty	Value	Uncertainty	Value	Uncertainty
13ZP13	Pegmatitic vein mineralization	280.0	2.0	176.0	1.3	377.1	2.3	0.01	0.14	128.5	1.8
13ZP14	Disseminated mineralization	176.8	1.1	111.1	0.7	238.8	1.5	0.21	0.28	128.9	1.7
13ZP14-1	Disseminated mineralization	223.2	1.6	140.3	1.0	298.9	2.0	0.01	0.40	127.8	1.8
13ZP16	Pegmatitic vein mineralization	194.5	1.2	122.3	0.8	260.8	1.6	0.01	0.47	127.9	1.7
13ZP16-1	Pegmatitic vein mineralization	198.8	1.2	125.0	0.8	268.1	1.7	0.28	0.62	128.6	1.7
13ZP17	Disseminated mineralization	363.6	2.8	228.5	1.7	488.7	3.0	0.01	0.30	128.2	1.8

The uncertainties in Re and Os concentrations include spike calibration uncertainties, weighing errors for spikes and samples, mass measurement and error magnification associated with spiking and spike calibrations. There is also an uncertainty (1.02%) in ^{187}Re decay constant 1.666×10^{-11} $year^{-1}$ for model age calibration (Du et al., 2004). The total uncertainties at the 95% confidence level were calculated using the formula for error propagation before expanding the resulting standard deviation appropriately (Du et al., 2004).

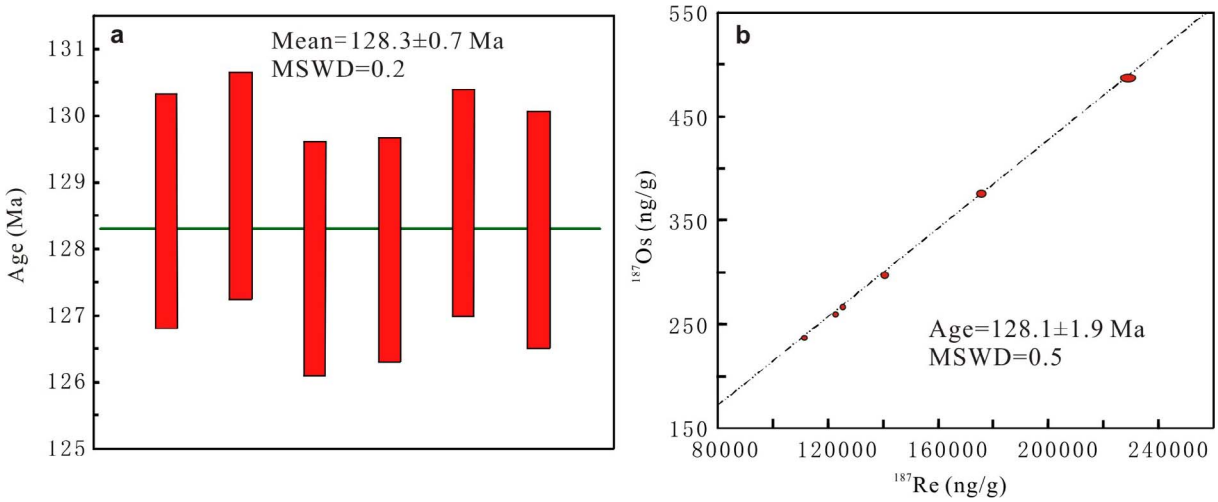

Fig. 5. Re-Os dating of molybdenite for the Wangjiazhuang deposit. (a) Model ages. (b) ^{187}Os vs ^{187}Re plot illustrating the isochron age.

zircon/melt partition coefficients of Ce^{3+} and Ce^{4+}. $D^{zrc/melt}_{Ce^{3+}}$ and $D^{zrc/melt}_{Ce^{4+}}$ are calculated based on the lattice-strain model (Ballard et al., 2002). According to this method, the Ce^{4+}/Ce^{3+} ratios of the zircon grains range from 64 to 359 (Table 5), much higher than those of the contemporaneous lithospheric mantle-derived mafic rocks (Fig. 9b). The Ti contents of the zircon grains change from 11.0 to 18.4 ppm, averaging at 14.0 ppm.

No obvious zoning was detected by CL imaging in both the igneous and hydrothermal quartz, implying the homogeneous compositions in the studied quartz. Trace element compositions show some systematic variations from the igneous quartz to the different stages of the hydrothermal quartz. Li, Na, Mg, Al, K, Ti, Sc, Cr and Ge are present in both the igneous and hydrothermal quartz, of which the Mg, Ti and Sc show the highest contents in the igneous quartz, while the Li, Na, Al and Ge are most abundant in the post-mineralization hydrothermal quartz. The quartz of the ore-forming pegmatitic vein has the lowest Na and the highest K contents (Table 6).

5.5. Sr-Nd-Hf isotopic compositions of the quartz monzonite

The quartz monzonite has high Rb (107–142 ppm) and Sr (867–1219 ppm) contents and shows low $^{87}Rb/^{86}Sr$ (0.2550–0.4728) and $^{87}Sr/^{86}Sr$ (0.706032–0.706203) ratios (Table 7 and Fig. 10a). When calculated back to the intrusive age of 128.8 Ma, the initial $^{87}Sr/^{86}Sr$ ratios range from 0.705309 to 0.705704. Low Sm (4.80–4.91 ppm) and relatively high Nd (26.6–28.5 ppm) contents are featured in the quartz monzonite. The $^{147}Sm/^{144}Nd$ ratios vary from 0.1038 to 0.1096 while the $^{143}Nd/^{144}Nd$ ratios change from 0.512544 to 0.512569, which result in the $\varepsilon_{Nd}(t)$ values varying from −0.3 to 0.1 (Table 7).

The Hf isotopic compositions of zircons are listed in Table 8 and shown in Fig. 10b. Twenty analyses (sample 13ZP01) yield $^{176}Hf/^{177}Hf$ ratios varying from 0.282699 to 0.282826 and $\varepsilon_{Hf}(t)$ values of 0.2–4.6.

5.6. Sulfur isotopic compositions of sulfides

Sulfur isotopic compositions of sulfides are listed in Table 9. The $\delta^{34}S_{CDT}$ values of four pyrite samples selected from the early potassic alteration stage are significantly negative, ranging from −7.07‰ to −5.05‰ (average at −5.83‰). By contrast, the sulfides from the Cu-Mo mineralization stage have higher $\delta^{34}S_{CDT}$ values, of which five chalcopyrite samples show the values of −3.78‰ to −3.29‰ (average at −3.58‰), three pyrite samples have the values ranging from −2.78‰ to −2.55‰ (average at −2.69‰) and five molybdenite samples are characterized by −1.54‰ to −1.02‰ (average at −1.28‰). The $\delta^{34}S_{CDT}$ values in the Cu-Mo mineralization stage increase from the chalcopyrite to the pyrite and then to the molybdenite, which are consistent with isotope equilibrium fractionation among the sulfides (Ohmoto and Rye, 1979).

5.7. He-Ar isotopic compositions of sulfides

He and Ar isotopic compositions of sulfides are listed in Table 10 and shown in Fig. 11. The samples have ^{3}He and ^{4}He concentrations of (3.93–14.3) × 10^{-14} cm^3 STP/g and (1.41–9.65) × 10^{-8} cm^3 STP/g, respectively, resulting in the $^3He/^4He$ ratios of 0.8–2.9 Ra (Ra represents the $^3He/^4He$ ratio of air, 1.39 × 10^{-6}). The concentrations of ^{36}Ar and ^{40}Ar have larger variations, showing (8.87–116) × 10^{-11} cm^3 STP/g and (4.08–132) × 10^{-8} cm^3 STP/g, respectively. The $^{40}Ar/^{36}Ar$ ratios of the samples change from 353 to 1131, which are higher than that of the air (295.5).

5.8. Petrographic and Laser Raman spectroscopic results of fluid inclusions

Combined with petrographic observations under microscope and Laser Raman spectroscopic results at room temperature, four types of primary fluid inclusions were identified in the ore-forming pegmatitic veins, but only one type was identified in the post-mineralization quartz veins. They are described as follows:

(1) L-type: Liquid-rich fluid inclusions consisting of a dominant liquid H_2O phase and a small H_2O bubble (< 40% in volume) (Fig. 12a). This type of fluid inclusion is abundant in both the pegmatitic veins and the quartz veins. The fluid inclusions vary from 5 to 35 μm in size, with the common size of 10–20 μm. Most of them show negative crystal shapes, although round, polygonal and irregular shapes are also present. They occur isolated or distribute in groups in the pegmatitic veins, but are commonly grouped in clusters in the quartz veins.

(2) V-type: Vapor-rich fluid inclusions composed by a large H_2O bubble (> 70% in volume) and a small liquid H_2O phase (Fig. 12b). This type of fluid inclusion is only present in the pegmatitic veins. The fluid inclusions commonly occur isolated and show negative crystal shapes, with the sizes ranging from 9 to 20 μm. Notably, weak CO_2 signals were detected in some fluid inclusions of this type using Laser Raman spectroscopy, but could not be observed under microscope or using microthermometry. This phenomenon is likely due to the low contents of CO_2 in the fluid inclusions and the low detection limit of the Laser Raman spectroscopy. Experiments have shown that the detection limit of CO_2 for a fluid inclusion by laser Raman spectroscopy is about 1 bar at ambient temperature, but

Table 4
Major oxides (wt.%) and trace elements (ppm) data for the quartz monzonite and the altered counterparts.

Sample	13ZP01	02	03	04	05	06	07	08	09	Gain and loss of element		GSR1	GSR1	GSR3	GSR3
Rock type	Fresh quartz monzonite					Potassic alteration		Sericitic alteration		Potassic Alteration[b]	Sericitic alteration[c]	Avg.[d]	Rem.[e]	Avg.	Rem.
SiO_2	64.2	66.1	64.1	63.7	65.8	64.8	64.7	65.8	66.5	−0.45	−0.97	73.4	72.8	44.0	44.6
TiO_2	0.46	0.45	0.48	0.47	0.44	0.36	0.44	0.35	0.34	−0.06	−0.07	0.29	0.28	2.36	2.36
Al_2O_3[a]	16.4	15.6	16.4	16.4	15.5	16.2	16.2	16.8	16.8	0.00	0.00	13.4	13.4	13.5	13.8
$Fe_2O_3^T$	3.95	3.77	4.09	4.18	3.85	2.89	3.63	2.14	2.33	−0.73	−1.10	2.15	2.14	13.3	13.4
FeO	0.32	0.32	0.27	1.84	1.74	0.78	1.53	0.96	0.85	0.25	−0.28				
MnO	0.04	0.07	0.08	0.09	0.07	0.04	0.04	0.01	0.01	−0.03	−0.03	0.06	0.06	0.17	0.17
MgO	1.68	1.32	1.52	1.43	1.38	0.44	1.43	0.29	0.45	−0.54	−0.58	0.43	0.42	7.64	7.77
CaO	2.37	2.65	3.20	3.28	2.73	1.98	1.30	1.01	0.75	−1.22	−0.79	1.57	1.55	8.79	8.81
Na_2O	4.90	4.66	5.12	5.05	4.59	5.63	5.00	3.59	4.11	0.41	−1.60	3.15	3.13	3.32	3.38
K_2O	4.41	4.34	4.09	4.16	4.43	4.56	5.1	7.72	5.82	0.51	1.70	5.06	5.01	2.33	2.32
P_2O_5	0.21	0.18	0.22	0.21	0.18	0.15	0.19	0.13	0.13	−0.03	−0.04	0.10	0.09	0.96	0.95
LOI	1.00	0.46	0.26	0.32	0.48	2.58	1.4	1.98	2.16	1.47	0.01				
Sum	99.9	99.8	99.9	99.6	99.7	99.9	99.7	100.0	99.6	−0.70	−3.51				
Li	15.7	9.69	13.0	7.36	9.97	10.1	16.5	12.6	12.6	2.06	−1.16	126	131	9.31	9.50
Sc	6.05	5.87	5.40	6.37	5.21	3.07	4.24	2.67	3.01	−2.15	−0.92	6.04	6.10	15.3	15.2
V	76.2	70.7	76.3	81.0	69.1	71.1	68.9	72.2	64.4	−5.15	−4.10	23.8	24.0	162	167
Cr	117	231	137	120	123	133	125	90.5	55.2	−17.3	−58.9	6.21	5.00	134	134
Co	9.36	8.44	8.65	8.77	7.62	4.62	8.36	1.70	3.75	−2.12	−3.86	2.84	3.40	47.4	46.5
Ni	28.2	16.3	25.5	15.7	15.1	10.8	13.7	16.3	11.8	−7.98	1.27	5.03	2.30	146	140
Cu	101	86.1	80.1	137	44.2	1018	1193	810	947	1008	−258	1.99	3.20	51.4	48.6
Zn	27.5	55.9	63.3	70.4	44.7	27.2	30.7	6.1	29.7	−23.6	−11.7	22.7	28.0	153	150
Ga	25.0	23.7	25.5	26.1	23.9	24.1	24.3	23.1	24.8	−0.79	−1.14	18.7	19.0	24.6	24.8
Rb	146	143	94	110	119	120	114	204	53.0	−6.44	7.04	442	466	38.2	37.0
Sr	936	829	1049	1185	729	458	674	449	162	−383	−272	101	106	1113	1100
Y	11.1	11.8	11.9	11.2	11.6	9.66	11.3	5.67	9.50	−1.09	−3.18	59.6	62.0	21.6	22.0
Zr	138	164	128	131	158	129	126	136	59.6	−11.0	−33.6	161	167	279	277
Nb	8.77	10.7	9.84	9.26	12.1	9.09	10.2	8.15	9.61	−0.55	−1.09	38.1	40.0	68.3	68.0
Cs	9.11	11.9	6.33	6.31	8.57	3.75	7.12	3.71	4.18	−3.04	−1.63	36.3	38.4	0.50	0.49
Ba	1588	1266	1557	1607	1345	1367	1578	1958	486	−10.6	−293	348	343	526	526
La	32.6	39.9	32.4	34.2	39.0	29.9	35.1	26.6	26.2	−3.38	−7.05	52.2	54.0	57.4	56.0
Ce	68.1	77.0	65.2	67.1	75.0	56.3	66.2	38.8	18.8	−9.70	−33.5	103	108	108	105
Pr	7.67	8.23	7.13	7.66	7.38	7.01	8.12	4.17	6.62	−0.10	−2.36	12.9	12.7	13.4	13.2
Nd	28.5	29.8	24.9	28.5	25.8	25.1	29.7	14.0	25.1	−0.27	−8.54	47.0	47.0	55.3	54.0
Sm	4.98	4.90	5.11	5.04	4.63	4.01	5.40	2.45	4.35	−0.26	−1.42	9.65	9.70	10.6	10.2
Eu	1.38	1.19	1.33	1.47	1.08	0.95	1.29	0.57	1.32	−0.17	−0.21	0.80	0.85	3.28	3.20
Gd	3.84	3.83	3.77	3.91	3.38	2.94	3.77	1.67	3.08	−0.41	−1.07	8.86	9.30	9.10	8.50
Tb	0.49	0.49	0.49	0.50	0.44	0.38	0.49	0.22	0.38	−0.05	−0.14	1.62	1.65	1.21	1.20
Dy	2.22	2.25	2.32	2.26	2.10	1.73	2.25	0.98	1.68	−0.26	−0.71	10.2	10.2	5.68	5.60
Ho	0.40	0.42	0.42	0.41	0.40	0.33	0.41	0.18	0.31	−0.04	−0.13	2.10	2.05	0.94	0.88
Er	1.01	1.10	1.07	1.01	1.14	0.88	1.04	0.52	0.84	−0.11	−0.30	6.53	6.50	2.01	2.00
Tm	0.15	0.16	0.16	0.14	0.16	0.14	0.15	0.09	0.13	−0.01	−0.04	1.07	1.06	0.24	0.28
Yb	0.95	1.07	1.00	0.90	1.07	0.90	0.98	0.61	0.88	−0.06	−0.23	7.54	7.40	1.32	1.50
Lu	0.15	0.16	0.15	0.13	0.17	0.14	0.15	0.10	0.14	−0.01	−0.03	1.19	1.15	0.18	0.19
Hf	4.38	5.17	4.20	3.35	5.14	4.13	4.19	4.09	4.06	−0.32	−0.23	6.24	6.30	6.76	6.50
Ta	0.54	0.69	0.62	0.53	0.89	0.60	0.64	0.58	0.66	−0.04	−0.02	7.09	7.20	4.49	4.30
Tl	0.99	0.73	0.47	0.54	0.72	1.01	1.08	1.45	1.07	0.35	0.17	1.92	1.93	0.05	0.12
Pb	18.1	31.4	26.3	27.7	28.5	31.0	18.0	9.06	15.0	−2.10	−12.9	30.9	31.0	3.67	4.70
Bi	0.03	0.17	0.31	0.20	0.04	0.93	1.61	0.22	0.69	1.11	−0.83	0.48	0.53	0.00	0.05
Th	15.3	19.8	13.8	13.5	21.8	15.2	15.0	11.9	18.3	−1.86	−0.54	56.7	54.0	6.51	6.00
U	6.01	3.70	3.45	3.02	6.11	3.45	4.30	3.03	8.67	−0.61	1.77	18.7	18.8	1.48	1.40
T_{Zr}(°C)[f]	749	761	732	733	755										

[a] The element was assumed to be immobile and its ratio between the fresh and altered rock was used to calculate the gain and loss (Grant, 1986). The approach is: $\Delta C = (C^F_{immobile}/C^A_{immobile})\cdot C^A - C^F$, where C^F and C^A are the concentrations in the fresh (F) and altered (A) samples, respectively, and ΔC denotes the gain or loss in grams per 100 g for major elements and per million for trace elements.

[b] Gains and losses of elements of potassic alteration are compared to the average value of the fresh quartz monzonite.

[c] Gains and losses of elements of sericitic alteration are compared to the average value of the potassic alteration.

[d] Average value actually measured for reference standard.

[e] Recommended value for reference standard.

[f] Calculated from zircon saturation thermometry, $\ln D_{Zr}^{zircon/melt} = 12{,}900/T_{Zr}(K) - 0.85(M-1) - 3.8$, M = (Na + K + 2Ca)/(Al × Si) cation ratio (Watson and Harrison, 1983).

should be up to 10.4 bars (based on clathrate dissociation) or 45 bars (based on solid CO_2 melting) by microthermometry (Rosso and Bodnar, 1995). This indicates that the CO_2 pressures in the V-type fluid inclusions are lower than 10.4 bars and thus the CO_2 can be ignored.

(3) D-type: Daughter mineral-bearing fluid inclusions composed by liquid H_2O, vapor H_2O and daughter mineral (Fig. 12c and d). This type of fluid inclusion is only present in the pegmatitic veins. They commonly show irregular shapes with sizes between 6 and 32 μm. They are isolated or grouped in clusters. The vapor phase occupies < 30 vol% of the inclusions, whereas the solid phase occupies 5–50 vol%. Three kinds of daughter minerals have been identified, of which halite and sylvite are dominant and hematite is rare. The crystals of halite are cubic and colorless with sizes ranging from 2 to 10 μm (Fig. 12c). The sylvite crystals are rounded with the largest size less than 5 μm. Hematite shows red color (Fig. 12d) and can be easily identified by the Raman spectrum. Besides the common occurrence of one daughter mineral in an inclusion, coexistence of two to three daughter minerals

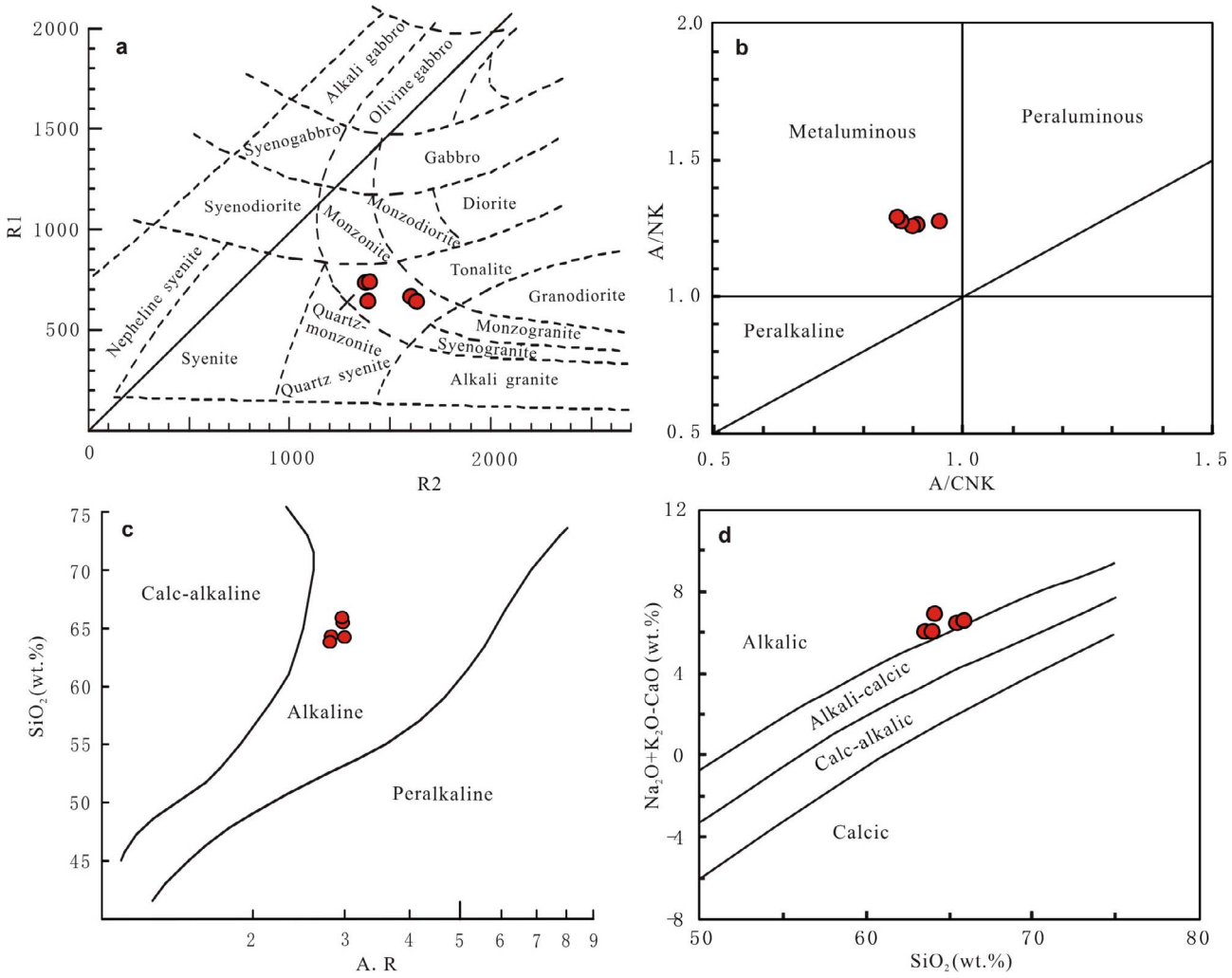

Fig. 6. Plots of (a) R1 vs. R2 [R1 = 4Si-11(Na + K)-2(Fe + Ti), R2 = 6Ca + 2 Mg + Al], (b) A/NK vs. A/CNK [A/NK = molar ratio $Al_2O_3/(Na_2O + K_2O)$, A/CNK = molar ratio $Al_2O_3/(CaO + Na_2O + K_2O)$], (c) SiO_2 vs. A.R [A.R. = $(Al_2O_3 + CaO + Na_2O + K_2O)/(Al_2O_3 + CaO\text{-}Na_2O\text{-}K_2O)$] and (d) ($Na_2O + K_2O$-CaO) vs. SiO_2 for the quartz monzonite. (a), (b) and (c) are from De la Roche et al. (1980), Wright (1969) and Frost et al. (2001), respectively.

was also observed (Fig. 12c and d). Coexistence of D-type, L-type and V-type fluid inclusions is common (Fig. 12e).

(4) C-type: Carbon dioxide-bearing fluid inclusions showing three phases of liquid H_2O, liquid CO_2 and vapor CO_2 (Fig. 12f). This type of fluid inclusion is only present in the pegmatitic veins and rarely observed in the studied samples. One such inclusion was clearly observed, which shows triangle shape with the long diameter of 20 μm. It occurs as an isolated inclusion. The liquid and vapor CO_2 phases occupies about 40 vol% of the inclusion, of which the vapor CO_2 is dominant.

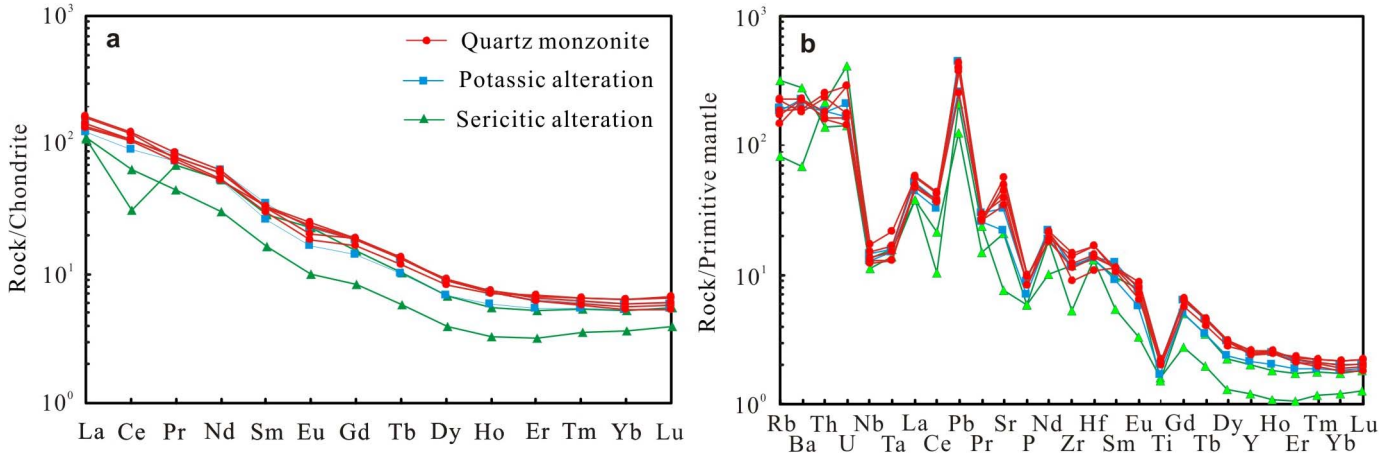

Fig. 7. (a) Chondrite-normalized REE pattern and (b) Primitive Mantle (PM) normalized spider diagram for the fresh and altered quartz monzonite samples. Chondrite and PM values are from Sun and McDonough (1989).

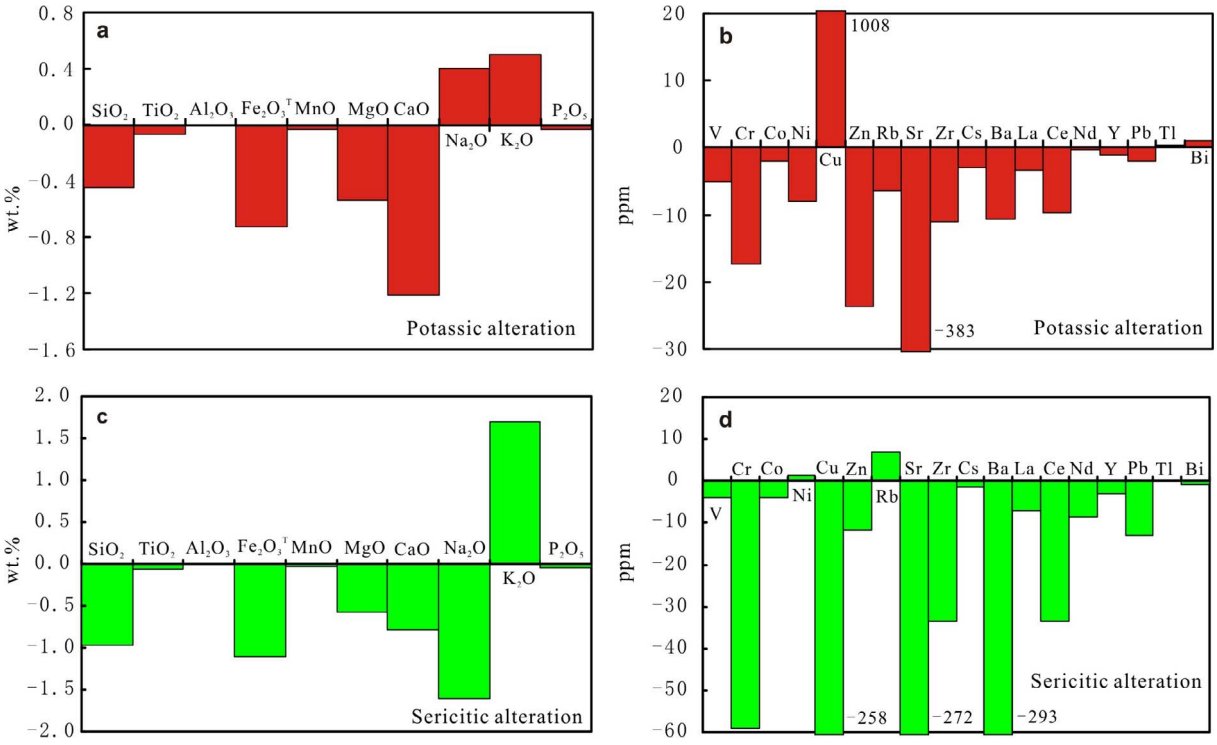

Fig. 8. Gains and losses of major and trace elements of the quartz monzonite during potassic (a and b) and sericitic (c and d) alterations. Gains and losses of elements of potassic alteration are compared to the average value of the fresh quartz monzonite, whereas those of the sericitic alteration are compared to the average value of the potassic alteration. The detailed calculations are described in Table 4.

5.9. Microthermometric results of fluid inclusions

Microthermometric results are shown in Fig. 13 and described below.

(1) L-type fluid inclusions: During cooling, most of the L-type fluid inclusions were frozen at the temperatures between −30 °C and −40 °C. Heating was started after the inclusions were totally frozen below −60°C. In the ore-forming pegmatitic veins, the L-type fluid inclusions have the final ice melting temperatures (Tm_{ice}) varying from −10.3 °C to −5.0 °C, which correspond to the salinities of 7.9–14.2 wt% NaCl equivalent (average at 9.8 wt% NaCl eqv.) when using the equation from Bodnar (1993) to calculate the salinity (Fig. 13a). The fluid inclusions homogenized to liquid phase,

Table 5
LA-ICP-MS zircon trace element concentrations (ppm) for the quartz monzonite (13ZP01).

Spot	Ti	La	Ce	Pr	Nd	Sm	Eu	Gd	Tb	Dy	Ho	Er	Tm	Yb	Lu	Hf	$(Ce/Ce^*)_D$	Ce^{4+}/Ce^{3+}	T_{Ti}(°C)[a]	T_{Ti}(°C)[b]
1	11.5	0.006	10.0	0.08	1.25	2.37	0.51	11.8	3.55	40.1	13.1	62.2	13.0	136	25.4	9723	84	103	760	715
2	12.0	0.024	19.0	0.05	1.97	2.82	0.59	12.0	3.23	36.4	12.2	59.0	11.9	127	23.8	10,159	66	127	763	719
3	18.4	0.008	18.2	0.09	1.55	2.62	0.63	11.6	3.38	36.8	12.6	64.2	12.7	134	24.3	9530	132	165	807	762
4	15.7	0.016	19.4	0.15	1.74	2.20	0.51	11.2	3.11	35.3	12.4	61.8	12.5	132	25.6	11,100	80	92	790	746
5	16.4	0.021	12.1	0.07	1.43	2.88	0.59	13.4	4.02	43.0	14.4	70.9	13.8	146	26.4	9362	103	75	794	750
6	14.0	0.010	26.3	0.08	1.07	2.51	0.55	11.6	3.54	35.9	12.7	57.6	12.4	126	23.1	10,404	232	213	779	734
7	11.4	0.012	11.7	0.09	0.96	2.07	0.45	11.5	3.45	41.4	14.5	71.2	14.6	158	30.7	10,314	120	83	758	714
8	14.6	0.014	19.8	0.10	1.77	3.02	0.61	13.2	3.97	40.5	13.9	67.2	13.8	149	28.6	9947	121	120	783	738
9	14.3	0.027	19.4	0.06	1.14	2.38	0.47	10.2	2.98	33.4	11.4	56.5	11.7	123	23.2	10,267	200	111	780	736
10	11.0	0.009	8.60	0.02	0.61	1.42	0.26	5.84	2.04	24.6	8.90	45.2	9.41	101	19.3	10,604	245	145	755	710
11	14.1	0.008	22.1	0.13	1.62	3.25	0.84	14.6	4.07	46.3	15.2	71.9	14.6	150	28.6	11,135	122	157	779	735
12	12.3	0.006	15.3	0.09	0.87	2.28	0.46	11.3	3.39	37.4	12.6	61.6	12.9	137	26.1	9949	145	145	766	722
13	13.0	0.006	19.8	0.14	2.63	4.55	0.85	17.5	4.67	48.9	16.0	74.2	15.1	156	28.2	10,782	72	152	771	726
14	12.2	0.040	24.4	0.20	3.24	5.59	1.34	22.6	6.26	71.7	24.9	121	24.5	260	48.8	9778	77	63	765	720
15	18.3	0.006	13.0	0.14	1.88	4.54	0.75	19.6	5.42	61.7	20.8	98.2	19.6	203	38.0	10,332	64	101	806	761
16	14.4	0.004	13.2	0.10	1.53	3.10	0.59	13.4	3.81	46.5	15.8	76.7	15.4	162	31.0	10,263	92	148	781	737
17	15.3	0.091	12.6	0.05	0.83	2.09	0.39	10.4	3.16	35.1	12.0	58.0	11.8	124	23.5	11,180	218	190	787	743
18	12.1	0.011	13.0	0.08	1.23	3.03	0.56	13.6	3.80	43.9	15.1	71.6	14.3	149	28.9	9903	109	103	764	720
19	17.9	0.014	19.2	0.04	0.90	2.05	0.44	9.73	2.74	32.5	10.8	52.2	10.8	112	21.6	10,492	271	179	803	759
20	11.8	0.002	13.5	0.05	1.32	2.50	0.56	12.5	3.82	41.6	14.4	67.5	14.0	142	26.9	10,002	143	291	762	717
Mean	14.0	0.017	16.7	0.09	1.48	2.86	0.60	12.9	3.72	41.6	14.2	68.4	13.9	146	27.6	10,261	135	133	778	733

[a] Calculated from Ti-in-zircon thermometer (Ferry and Watson, 2007). The thermometer is given as $\log Ti_{zircon}(ppm)) = 5.711–4800/T_{Ti}(K) - \log\alpha_{SiO_2} + \log\alpha_{TiO_2}$, in which the activities of TiO_2 (α_{TiO_2}) and SiO_2 (α_{SiO_2}) must be defined. The quartz monzonite contains quartz grains, thus the α_{SiO_2} is set to 1 ($\log\alpha_{SiO_2} = 0$). The estimation of α_{TiO_2} is based on the method of Hayden and Watson (2007), which is on the assumption that the solubility of TiO_2 in siliceous melt can be calculated from $\log Ti_{melt}(ppm) = 7.95–5305/T(K) + 0.124FM$ (FM = 1/Si × (Na + K + 2(Ca + Mg + Fe))/Al, cation fractions). According to this method, only 1253–1310 ppm Ti could lead to the rutile saturation in the quartz monzonite. The quartz monzonite contains 2638–2878 ppm Ti, suggesting the saturation of TiO_2 in the melt. Thus the α_{TiO_2} is also set to 1 ($\log\alpha_{TiO_2} = 0$).

[b] Pressure-corrected temperature.

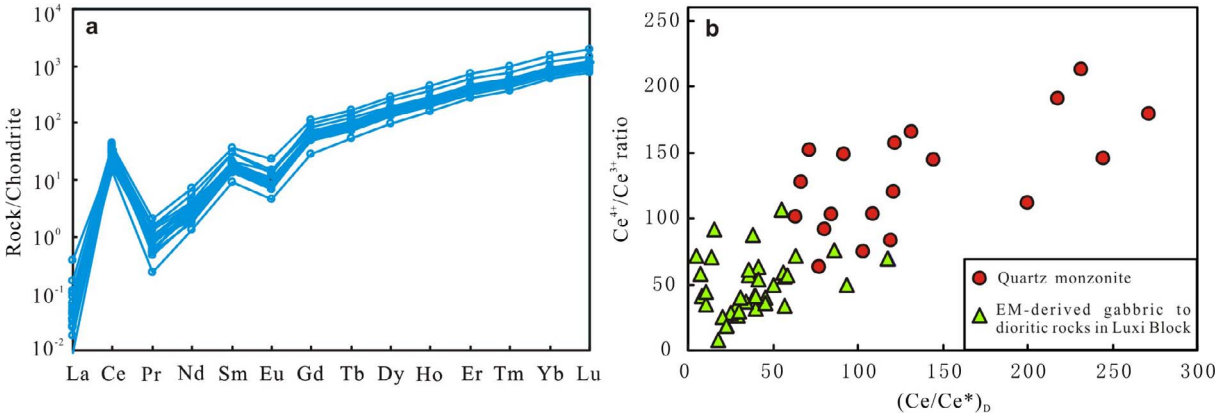

Fig. 9. (a) Chondrite-normalized REE pattern and (b) Ce^{4+}/Ce^{3+} ratio vs. $(Ce/Ce^*)_D$ plot for the zircon grains from the quartz monzonite.

with the homogenization temperatures of 280–417 °C (average at 349 °C) (Fig. 13b). For the fluid inclusions from the post-mineralization quartz veins, they have the Tm_{ice} varying from −5.3 °C to −4.4 °C (average at −4.8 °C), which correspond to the salinities of 7.0–8.3 wt% NaCl eqv. (average at 7.6 wt% NaCl eqv.). They also homogenized to the liquid phase, with the homogenization

Table 6
Major and trace element concentrations (ppm) in representative igneous and hydrothermal quartz from the Wangjiazhuang deposit.

Spot		Li	Na	Mg	Al	K	Sc	Ti	Cr	Ge	Rb	Sr	P_{Ti} (kbar)
13ZP01-01	Quartz monzonite	20.4	15.5	18.8	173	17.7	0.91	159	2.34	0.98	0.26	0.42	1.26
13ZP01-02		14.2	14.0	8.35	178	15.8	1.08	175	3.88	1.10	0.19	0.33	1.05
13ZP01-03		11.5	11.5	11.0	144	9.54	1.18	178	3.54	1.46	0.41	0.77	1.02
13ZP01-04		18.0	9.83	11.0	163	11.2	1.14	173	3.26	0.99	0.25	0.88	1.08
13ZP01-05		21.3	13.0	19.5	188	8.16	1.23	191	3.09	0.90	0.13	0.76	0.89
13ZP01-06		23.0	12.6	12.1	159	15.6	0.93	199	3.94	0.77	0.19	0.30	0.82
13ZP01-07		21.0	11.1	16.9	149	8.51	1.38	171	1.04	0.41	0.12	0.46	1.10
13ZP01-08		17.3	9.92	14.5	171	15.5	0.95	160	1.80	0.76	0.23	1.11	1.24
13ZP01-09		21.2	8.48	10.9	170	13.3	1.08	146	1.96	1.29	0.12	1.01	1.46
13ZP01-10		14.9	11.0	21.8	196	8.98	1.02	173	2.39	1.29	0.64	0.94	1.08
13ZP01-11		15.9	9.74	13.0	135	8.55	0.94	198	2.40	0.88	0.11	1.00	0.83
13ZP01-12		17.0	14.4	20.2	152	6.44	0.75	177	2.72	1.00	0.09	0.90	1.04
13ZP01-13		22.5	20.7	8.16	165	7.39	1.14	198	2.71	1.28	0.15	0.47	0.83
13ZP01-14		18.3	13.1	16.3	151	6.58	0.96	174	1.86	0.77	0.11	0.72	1.06
13ZP01-15		17.6	16.8	18.7	175	13.6	0.64	171	2.54	0.81	0.18	1.15	1.10
13ZP01-16		10.8	19.7	18.7	156	11.2	1.32	141	1.48	1.48	0.40	0.58	1.54
13ZP01-17		15.7	14.0	17.1	143	12.0	1.04	163	1.48	1.29	0.11	0.97	1.20
	Average	17.7	13.3	15.1	163	11.2	1.0	181	2.50	1.03	0.22	0.75	1.10
13ZP15-01	Ore-forming pegmatitic vein	14.7	5.92	6.71	216	24.2	0.67	24.8	2.25	1.20	0.19	–	
13ZP15-02		15.2	3.09	5.75	199	19.4	0.73	21.7	1.29	1.24	0.18	–	
13ZP15-03		14.8	4.09	5.32	175	11.6	0.71	21.3	1.10	1.25	0.15	–	
13ZP15-04		11.9	6.16	6.28	179	7.00	0.69	22.5	1.85	1.27	0.18	–	
13ZP15-05		12.3	6.18	7.20	220	24.1	0.67	21.8	2.16	1.33	0.20	–	
13ZP15-06		12.9	4.77	7.58	204	15.8	0.70	22.1	1.98	1.08	0.16	–	
13ZP15-07		13.3	1.31	11.2	170	14.7	0.68	21.5	3.18	1.35	0.08	–	
13ZP15-08		12.8	5.31	10.4	176	9.05	0.75	22.0	2.05	1.08	0.10	–	
13ZP15-09		11.4	5.57	12.7	208	19.3	0.64	26.3	2.17	1.46	0.17	–	
13ZP15-10		10.7	4.43	12.7	210	27.2	0.53	26.6	1.16	1.27	0.27	–	
13ZP15-11		10.7	1.16	12.4	199	16.0	0.61	26.2	1.60	1.14	0.11	–	
13ZP15-12		12.9	2.27	11.4	220	25.5	0.58	27.5	1.53	0.93	0.26	–	
	Average	12.8	4.19	9.13	198	17.8	0.66	23.7	1.86	1.22	0.17		
13ZP29-01	Post-ore-forming quartz vein	388	21.3	5.21	2221	6.73	0.68	9.18	1.61	3.85	–	–	
13ZP29-02		383	28.8	7.20	2215	6.98	0.67	6.70	2.05	3.27	–	–	
13ZP29-03		374	23.5	8.51	2164	5.67	0.67	8.27	2.23	2.73	–	–	
13ZP29-04		403	24.3	7.47	2272	4.09	0.78	10.0	2.26	3.74	–	–	
13ZP29-05		420	31.7	9.21	2521	5.39	0.66	9.49	2.49	4.03	–	–	
13ZP29-06		450	35.3	7.78	2609	4.41	0.68	6.49	2.38	3.51	–	–	
13ZP29-07		410	27.6	7.02	2424	4.73	0.64	9.60	1.85	3.66	–	–	
13ZP29-08		414	27.7	7.33	2384	5.37	0.60	10.2	2.06	3.89	–	–	
13ZP29-09		397	23.9	8.54	2366	3.32	0.75	10.8	2.15	2.88	–	–	
13ZP29-10		403	32.6	8.22	2334	6.87	0.66	3.28	3.94	5.53	–	–	
13ZP29-11		387	20.8	10.4	2161	2.97	0.56	4.59	3.90	4.89	–	–	
13ZP29-12		368	18.0	7.27	2073	3.70	0.94	7.56	1.32	4.27	–	–	
13ZP29-13		381	15.4	7.94	2078	2.93	0.89	7.44	1.01	4.44	–	–	
	Average	398	25.5	7.85	2294	4.86	0.70	7.97	2.25	3.90			

"-" indicates the concentration below detection limit. The pressure (P_{Ti}) is calculated from the titanium-in-quartz thermobarometer of Huang and Audétat(2012). The thermobarometer is written as $\log Ti(ppm) = -0.27943 \times 10^4/T(K) - 660.53 \times P^{0.35}/T + 5.6459$, in which the T is represented by the average T_{Zr} (746 °C) in this study.

Table 7
Sr-Nd isotopic compositions of the quartz monzonite.

Sample	Rb (ppm)	Sr (ppm)	$^{87}Rb/^{86}Sr$	$^{87}Sr/^{86}Sr$	± 2σ	I_{sr}[a]	Sm (ppm)	Nd (ppm)	$^{147}Sm/^{144}Nd$	$^{143}Nd/^{144}Nd$	± 2σ	$\varepsilon_{Nd}(t)$[b]	$\int_{Sm/Nd}$
13ZP02	142	867	0.4728	0.706175	0.000012	0.705309	4.89	28.5	0.1038	0.512544	0.000010	−0.3	−0.473
13ZP03	111	1182	0.2723	0.706203	0.000012	0.705704	4.91	27.1	0.1096	0.512569	0.000012	0.1	−0.443
13ZP04	107	1219	0.2550	0.706032	0.000011	0.705565	4.80	26.6	0.1094	0.512548	0.000012	−0.3	−0.444
13ZP05	138	942	0.4227	0.706126	0.000011	0.705352	4.84	27.6	0.1063	0.512547	0.000009	−0.3	−0.460

[a] Chondrite Uniform Reservoir (CHUR) values ($^{87}Rb/^{86}Sr$ = 0.0847, $^{87}Sr/^{86}Sr$ = 0.7045, $^{147}Sm/^{144}Nd$ = 0.1967, $^{143}Nd/^{144}Nd$ = 0.512638) are used for the calculation. $\lambda_{Rb} = 1.42 \times 10^{-11}$ year^{-1}, $\lambda_{Sm} = 6.54 \times 10^{-12}$ year^{-1} (Lugmair and Harti, 1978).
[b] Chondrite Uniform Reservoir (CHUR) values ($^{87}Rb/^{86}Sr$ = 0.0847, $^{87}Sr/^{86}Sr$ = 0.7045, $^{147}Sm/^{144}Nd$ = 0.1967, $^{143}Nd/^{144}Nd$ = 0.512638) are used for the calculation. $\lambda_{Rb} = 1.42 \times 10^{-11}$ year^{-1}, $\lambda_{Sm} = 6.54 \times 10^{-12}$ year^{-1} (Lugmair and Harti, 1978).

temperatures ranging from 246 °C to 292 °C (average at 266 °C).

(2) V-type fluid inclusions: Because of the large vapor percentages, it was difficult to observe the ice melting temperature. Nonetheless, the obtained results show that the fluid inclusions have the Tm_{ice} ranging from −4.9 °C to −1.1 °C (average at −3.1 °C). These temperatures correspond to the salinities of 1.9–7.7 wt% NaCl eqv. (average at 5.0 wt% NaCl eqv.). They commonly homogenized to vapor phase and show the homogenization temperatures of 306–415 °C (average at 358 °C). Critical homogenization was also observed in several fluid inclusions, showing the narrow homogenization temperatures of 384–388 °C. It is noteworthy that, although the V-type fluid inclusions have much larger vapor percentages than those of the L-type, the main homogenization temperatures of them are similar (Fig. 13b).

(3) D-type fluid inclusions: Liquid-vapor homogenization commonly occurred prior to the dissolution of the daughter minerals, showing that vapor bubbles disappeared firstly at the temperatures of 177–404 °C and subsequently daughter minerals of halite and/or sylvite dissolved at 287–466 °C (average at 362 °C). In a few cases, the daughter minerals dissolved before or simultaneous to the disappearance of the vapor bubbles, having the dissolution temperatures of daughter minerals at 198–324 °C and the disappearance temperatures of vapor bubbles at 289–352 °C. Hematite was not dissolved at temperatures even up to 550 °C. For calculating the salinities of this type of fluid inclusions, it is necessary to interpret why the daughter minerals (halite and/or sylvite) dissolved at temperatures greater than the liquid-vapor homogenization. Three models have been proposed for this phenomenon (Lecumberri-Sanchez et al., 2015, and references therein): (A) a high-salinity, single-phase liquid trapped at high pressures such that halite nucleates before vapor during cooling; (B) postentrapment modification such as loss of H_2O from the inclusions; (C) fluid inclusions heterogeneously entrapping solid halite together with fluid under halite-saturated conditions. Lecumberri-Sanchez et al. (2015) concluded that in most magmatic-hydrothermal systems the third model is ubiquitous and can be distinguished by no evidence of fluid inclusion migration and highly variable halite dissolution temperatures (e.g., ± 100 °C). Based on the above criteria, the D-type fluid inclusions in this study are well consistent with the third model and thus the salinities can be calculated using the method of Lecumberri-Sanchez et al. (2012), which is specially designed for such fluid inclusions. Therefore, using the HokieFlincs_H_2O-NaCl programs (Steele-MacInnis et al., 2012), the salinities of the D-type fluid inclusions vary between 33.8 and 52.6 wt% NaCl equivalent (average at 43 wt% NaCl eqv.) (Fig. 13a). Based on the disappearance temperatures of the daughter minerals (halite and/or sylvite) or the vapor bubbles, the final homogenization temperatures vary from 287 °C to 466 °C (average at 356 °C), well overlapping with those of the L- and V-type fluid inclusions (Fig. 13b).

(4) C-type fluid inclusions: Although rarely seen, the C-type fluid inclusions are significant for estimating the CO_2 contents as well as the P and T conditions of the ore-forming fluid. One of the C-type inclusions shows the melting temperature of solid CO_2 at −56.6 °C, consistent with that of the pure CO_2 (Angus et al., 1976). In addition, the CO_2 clathrate dissolved at 8.6 °C, corresponding to the salinity of 2.77 wt% NaCl eqv. (Collins, 1979). Partial

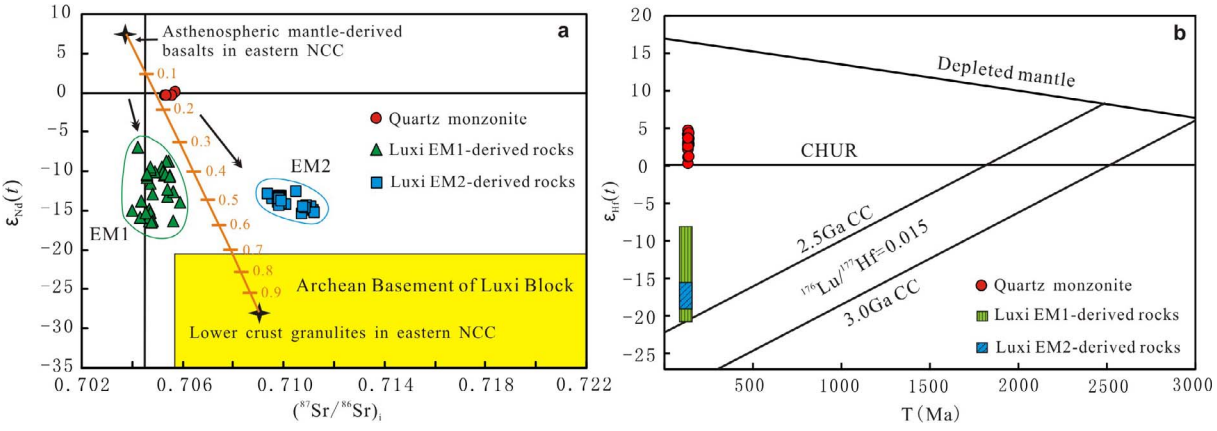

Fig. 10. (a) Plot of initial $^{87}Sr/^{86}Sr$ vs. $\varepsilon_{Nd}(t)$ and (b) diagram of Hf isotopic evolution in zircons from the quartz monzonite. The early Cretaceous EM1-derived rocks are represented by the Jinan and Zouping basalts/gabbros in the northern Luxi Block, the Sr-Nd isotopic data of which are from Guo et al. (2003), Yang et al. (2012) and Yang et al. (2012a), and the Hf isotopic data are from Yang et al. (2012a). The EM2-deirved rocks are represented by the Yinan, Fangcheng and Feixian basalts/gabbros in southeastern Luxi Block, the Sr-Nd isotopic data of which are from Zhang et al. (2002), Xu et al. (2004) and Yang et al. (2012), and the Hf isotopic data are from Yang et al. (2012b). The Sr-Nd isotopic compositions of the asthenospheric mantle beneath eastern NCC are represented by the average values of the late Cretaceous asthenosphere-derived basalts in eastern Shandong Province (Yan et al., 2005), while the lower crust is represented by the lower crust intermediate granulites in Hannuoba area in eastern NCC (Liu et al., 2004). The field of Archean basement rocks of Luxi Block is shown for comparison, and the Sr-Nd isotopic data of which are from Jahn et al. (1988). In (a), the mixing modeling parameters are Sr = 730 ppm, $^{87}Sr/^{86}Sr$ = 0.70373, Nd = 33.9 ppm, ε_{Nd} = 7.3 for the asthenospheric mantle and Sr = 1122 ppm, $^{87}Sr/^{86}Sr$ = 0.70897, Nd = 49.5 ppm, ε_{Nd} = −28.1 for the lower crust. In (b), the depleted mantle evolution is calculated by using $\varepsilon_{Hf}(t)$ = 16.9 at t = 0 Ma and $\varepsilon_{Hf}(t)$ = 6.4 at t = 3.0 Ga, the applied parameters are as in Table 8. The corresponding lines of crustal extraction are calculated by using the $^{176}Lu/^{177}Hf$ ratio of 0.015 for the average continental crust (Griffin et al., 2002). Abbreviations: CHUR, chondritic uniform reservoir; CC, continental crust.

Table 8
LA-MC-ICP-MS zircon Hf isotopic data for the quartz monzonite (13ZP01).

Spot No.	Age (Ma)	$^{176}Yb/^{177}Hf$	$^{176}Lu/^{177}Hf$	$^{176}Hf/^{177}Hf$	2σ	$(^{176}Hf/^{177}Hf)_i$	$\varepsilon_{Hf}(0)$	$\varepsilon_{Hf}(t)$[a]	T_{DM1} (Ma)	T_{DM2} (Ma)	$f_{Lu/Hf}$
01	128	0.0218	0.0008	0.282776	0.000018	0.282774	0.2	2.9	671	1000	−0.98
02	128	0.0232	0.0009	0.282812	0.000031	0.282810	1.4	4.2	621	919	−0.97
03	129	0.0113	0.0004	0.282792	0.000019	0.282791	0.7	3.5	642	963	−0.99
04	131	0.0390	0.0014	0.282791	0.000021	0.282788	0.7	3.4	660	969	−0.96
05	129	0.0109	0.0004	0.282755	0.000019	0.282754	−0.6	2.2	694	1047	−0.99
06	129	0.0120	0.0004	0.282768	0.000020	0.282767	−0.2	2.6	677	1018	−0.99
07	129	0.0101	0.0004	0.282775	0.000021	0.282774	0.1	2.9	666	1002	−0.99
08	128	0.0243	0.0008	0.282826	0.000020	0.282824	1.9	4.6	602	889	−0.97
09	128	0.0120	0.0004	0.282809	0.000018	0.282808	1.3	4.1	619	924	−0.99
10	129	0.0114	0.0004	0.282750	0.000021	0.282749	−0.8	2.0	701	1057	−0.99
11	129	0.0146	0.0005	0.282809	0.000019	0.282807	1.3	4.1	622	926	−0.98
12	128	0.0353	0.0012	0.282812	0.000041	0.282809	1.4	4.1	629	923	−0.96
13	129	0.0144	0.0005	0.282783	0.000023	0.282781	0.4	3.2	658	985	−0.98
14	128	0.0101	0.0004	0.282699	0.000019	0.282698	−2.6	0.2	772	1174	−0.99
15	129	0.0105	0.0004	0.282722	0.000021	0.282721	−1.8	1.0	740	1121	−0.99
16	128	0.0123	0.0005	0.282770	0.000021	0.282769	−0.1	2.7	674	1013	−0.99
17	129	0.0185	0.0006	0.282806	0.000022	0.282804	1.2	4.0	627	933	−0.98
18	130	0.0108	0.0004	0.282813	0.000021	0.282812	1.5	4.3	613	914	−0.99
19	128	0.0155	0.0006	0.282774	0.000021	0.282773	0.1	2.8	671	1005	−0.98
20	128	0.0116	0.0004	0.282794	0.000021	0.282793	0.8	3.5	640	959	−0.99

[a] The following parameters are applied to the calculations: $(^{176}Lu/^{177}Hf)_{CHUR} = 0.0332$, $(^{176}Hf/^{177}Hf)_{CHUR,0} = 0.282772$, $(^{176}Lu/^{177}Hf)_{DM} = 0.0384$, $(^{176}Hf/^{177}Hf)_{DM,0} = 0.28325$ (Blichert-Toft and Albaréde, 1997; Griffin et al., 2000), ^{176}Lu decay constant $\lambda = 1.867 \times 10^{-11}\ a^{-1}$ (Söderlund et al., 2004).

homogenization of the liquid and vapor CO_2 phases to a vapor phase occurred at 19.0 °C, giving a CO_2 density of 0.186 g/cm^3 and vapor pressure of 56 bars (Brown and Lamb, 1989). The final homogenization to a vapor phase was completed at 384 °C. This temperature is almost the same as the critical homogenization temperatures of the V-type fluid inclusions (384–388 °C).

5.10. Major and trace element compositions of fluid inclusions

Different types of fluid inclusions from different stages of hydrothermal veins show some regular variations in compositions (Table 11). In the ore-forming pegmatitic veins, the D-type fluid inclusions contain the most abundant and diverse elements such as Na, K, Mn, Fe, Cu, Zn, Rb, Sr, Mo, Cs, Ba, W, Tl and Pb. For the L-type fluid inclusions, they commonly contain Na, K, Mn, Cu, Zn, Rb, Sr, Cs, Ba and Pb, but show much lower contents than those of the D-type fluid inclusions. Fe, Mo, W and Tl rarely occur in the L-type fluid inclusions. The V-type fluid inclusions contain the lowest Na, K, Mn, Fe, Zn, Rb, Sr and Pb contents and occasionally contain Mo. However, the Cu contents in the V-type fluid inclusions are significantly high, much higher than those of the L-type fluid inclusions or even higher than some of the D-type fluid inclusions. For the L-type fluid inclusions in the post-mineralization quartz veins, Na and K are the dominant elements. Minor Rb, Sr, Cs and W sporadically occur. While the element contents show wide variations, the element ratios are more constant and reliable. In the pegmatitic veins, the K/Na ratios in the D-type fluid inclusions (0.22–0.64, average at 0.38) decrease to the L-type fluid inclusions (0.09–0.49, average at 0.27), but increase to the V-type fluid inclusions (0.16–0.90, average at 0.46) (Fig. 14a). In addition, the D-type fluid inclusions have the highest Mn/Na, Fe/Na and Pb/Na ratios (Table 11). It is notable that the Cu/Na ratios are the highest in the V-type fluid inclusions (0.11–1.12, average at 0.45), but successively decrease to the L-type (0.0–0.66, average at 0.12) and then to the D-type (0.0–0.10, average at 0.05) fluid inclusions (Fig. 14b). The L-type fluid inclusions from the post-mineralization quartz veins show similar K/Na ratios (0.12–0.36, average at 0.21) to those of the pegmatitic veins (Table 11).

Table 9
Sulfur isotopic compositions of sulfides from the Wangjiazhuang deposit.

Sample	Mineral	Description	Hydrothermal stage	$\delta^{34}S_{CDT}$ (‰)	Avg. $\delta^{34}S_{CDT}$ (‰)
13ZP10	Py	Relicts of Kf + Py in Bi + Cpy + Mo + Qz vein	Potassic alteration	−7.07	−5.83
13ZP14	Py	Py disseminated in potassic alteration	Potassic alteration	−5.25	
13ZP17	Py	Py disseminated in potassic alteration	Potassic alteration	−5.05	
13ZP20	Py	Relicts of Py in Cpy + Tn + Qz assemblages	Potassic alteration	−5.94	
13ZP11	Cpy	Well-crystallized Cpy + Bn + Tn + Qz + Bi + Kf vein	Mineralization	−3.61	−3.58
13ZP15	Cpy	Well-crystallized Cpy + Bn + Tn + Mo + Qz + Bi + Kf vein	Mineralization	−3.29	
13ZP22	Cpy	Well-crystallized Cpy + Tn + Mo + Bi + Qz + Kf vein	Mineralization	−3.74	
13ZP24	Cpy	Well-crystallized Cpy + Qz + Kf vein	Mineralization	−3.49	
13ZP31	Cpy	Well-crystallized Cpy + Bi + Qz + Kf vein	Mineralization	−3.78	
13ZP32	Py	Coarse Py + Tn + Qz vein	Mineralization	−2.78	−2.69
14ZP01	Py	Well-crystallized Qz + Py vein	Mineralization	−2.74	
14ZP06	Py	Well-crystallized Qz + Py vein	Mineralization	−2.55	
13ZP10	Mo	Bi + Cpy + Mo + Qz vein	Mineralization	−1.31	−1.28
13ZP14	Mo	Mo + Cpy + Tn metasomatizing potassic alteration	Mineralization	−1.40	
13ZP22	Mo	Well-crystallized Cpy + Tn + Mo + Bi + Qz + Kf vein	Mineralization	−1.02	
13ZP23	Mo	Well-crystallized Mo + Qz + Kf vein	Mineralization	−1.54	
14ZP09	Mo	Well-crystallized Mo + Qz + Bi + Kf vein	Mineralization	−1.16	

Abbreviations: Kf, K-feldspar; Bi, biotite; Qz, quartz; Cpy, chalcopyrite; Py, pyrite; Bn, bornite; Tn, tennantite; Mo, molybdenite; Avg, average.

Table 10
He-Ar isotopic compositions of sulfides from the Wangjiazhuang deposit.

Sample	Mineral	Hydrothermal stage	$^{3}He(10^{-13}$ cm^{4} STP/g)	$^{4}He(10^{-8}$ cm^{3} STP/g)	R/Ra[a]	$^{40}Ar(10^{-8}$ cm^{3} STP/g)	$^{36}Ar(10^{-9}$ cm^{3} STP/g)	$^{40}Ar/^{36}Ar$	$^{40}Ar^{*}/^{4}He$[b]
13ZP11	Chalcopyrite	Mineralization	0.62	2.71	1.64 ± 0.05	6.86	0.09	773 ± 56	1.56
13ZP14	Chalcopyrite	Mineralization	1.07	9.65	0.80 ± 0.02	132	1.17	1131 ± 40	10.1
13ZP19	Pyrite	Mineralization	1.43	3.51	2.94 ± 0.13	10.5	0.15	719 ± 78	1.75
13ZP26	Pyrite	Mineralization	0.39	1.41	2.01 ± 0.07	4.08	0.12	353 ± 15	0.47

[a] Ra represents the $^{3}He/^{4}He$ ratio of air, 1.39×10^{-6}.
[b] $^{40}Ar^{*} = (^{40}Ar/^{36}Ar - 295.5) \times {}^{36}Ar$, and 295.5 is the $^{40}Ar/^{36}Ar$ ratio of air (Stuart et al., 1995).

6. Discussion

6.1. Genesis of the host granitoid

The host quartz monzonite is characterized by high Sr (729–1185 ppm) and low Y (11.1–11.9 ppm) and Yb (0.90–1.07 ppm) concentrations as well as high Sr/Y (63–106) and La/Yb (33–38) ratios. Coupled with the high SiO_2 (> 63 wt%) and Al_2O_3 (> 15 wt%) and low MgO contents (< 2 wt%), the quartz monzonite shows similar geochemical characteristics to adakites as defined by Defant and Drummond (1990). The adakitic affinity is also evidenced by the popular discrimination diagrams for adakites (Castillo, 2012), in which all the samples of the quartz monzonite clearly fall into the adakite field (Fig. 15). Since adakitic features can be produced by either partial melting of the subducted oceanic slab (e.g., Defant and Drummond, 1990), or partial melting of the mantle wedge modified by the slab melts (e.g., Martin et al., 2005), or melting of the thickened or delaminated lower crust (e.g., Wang et al., 2006, 2007), or even the magma mixing between the melts derived from the asthenosphere and the lower crust (e.g., Richards and Kerrich, 2007), the generation of the quartz monzonite might be produced through one of the above scenarios. Melting of subducting oceanic slab can only occur in situations where the slab is subducted at abnormally high temperatures, such as the subduction of young oceanic crust (≤25 Myr old), the shallow or stalled subduction, the slab detachment following arc collision, highly oblique subduction, ridge subduction, or in slab windows where hot asthenosphere is in direct contact with the plate edge (Defant and Kepezhinskas, 2001; Richards and Kerrich, 2007 and references therein). These scenarios, however, were likely not present in the eastern NCC during the early Cretaceous. The collisional events at the northern and southern margins of the NCC were completed before the middle Triassic (Meng and Zhang, 2000; Xiao et al., 2003; Windley et al., 2010), which do not support partial melting of young and hot oceanic slabs during the emplacement of the quartz monzonite. Although the eastern China was affected by the subduction of the Paleo-Pacific plate at least since the Jurassic (Maruyama et al., 1997; Zhou and Li, 2000; Li and Li, 2007; Sun et al., 2007), the steep subduction angle inferred from the high-resolution geophysical imaging (Fukao et al., 1992; Huang and Zhao, 2006; Ichiki et al., 2006; Xu et al., 2011; Zhao et al., 2017) and the far distance to the subduction zone (> 1000 km, Maruyama et al., 1997; Li and Li, 2007) preclude the shallow melting of the subducting oceanic slab to generate adakites in the study area. Actually, melts of the subducting Paleo-Pacific slab might have not affected the compositions of the mantle beneath the eastern NCC during the early Cretaceous (> 110Ma), because recycled oceanic slab materials were just detected in the mantle enclaves/magmas younger than ~100 Ma (Zhu et al., 2012a; Xu, 2014). The lithospheric mantle-derived mafic rocks show remarkably low $\varepsilon_{Nd}(t)$ and $\varepsilon_{Hf}(t)$ values (most of them are lower than −10, Fig. 10), characterizing the early Cretaceous lithospheric mantle beneath the eastern NCC to be a significantly enriched one (EM1 to EM2, Fig. 10a). Such low $\varepsilon_{Nd}(t)$ and $\varepsilon_{Hf}(t)$ values can only be explained by ancient continental crust involvement in the mantle region either through lower crust delamination (Xu et al., 2008, 2013) or through continental crust subduction (Zhang et al., 2002; Xu et al., 2004; Yang et al., 2012a, 2012b). In addition, even if partial melting of the subducting oceanic slab occurred, it is highly suspected that such slab-derived melt can still survive after passing through the thick mantle wedge (> 400 km, Huang and Zhao, 2006; Xu et al., 2011; Zhao et al., 2017). Therefore, partial melting of the oceanic slab was unlikely responsible for the origin of the quartz monzonite. The Nd-Hf isotopic compositions of the quartz monzonite are distinct from those of the local lower crust and the enriched subcontinental lithospheric mantle (Fig. 10), also precluding the lower crust as well as the lithospheric mantle as its source, or as its sole source.

It is noted that the Sr-Nd isotopic compositions of the quartz monzonite plot closely to the field of the asthenospheric mantle and show a trend to the EM2 or to the lower crust field on the $\varepsilon_{Nd}(t)$ vs. $(^{87}Sr/^{86}Sr)_i$ diagram (Fig. 10a), implying that the quartz monzonite likely

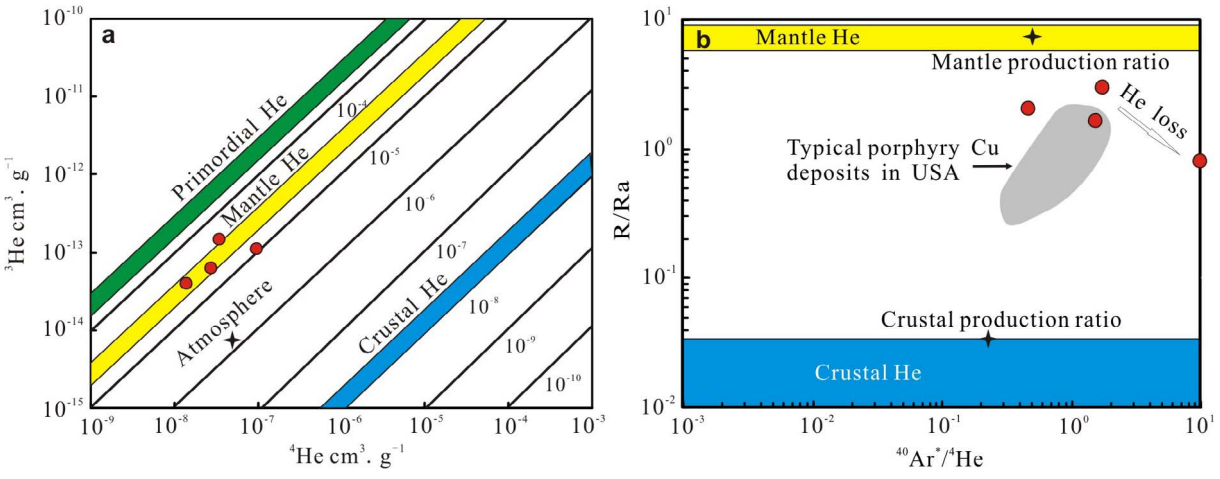

Fig. 11. Plots of (a) ^{3}He vs. ^{4}He and (b) R/Ra vs. $^{40}Ar^{*}/^{4}He$ for the sulfides selected from the Cu-Mo mineralization stage. (a) is after Mamyrin and Tolstikhin (1984). (b) is modified from Stuart et al. (1995). $^{40}Ar^{*}/^{4}He = (^{40}Ar/^{36}Ar\text{-}296) \times {}^{36}Ar/^{4}He$. The field of five typical porphyry Cu deposits in USA (Kendrick et al., 2001) is shown for comparison.

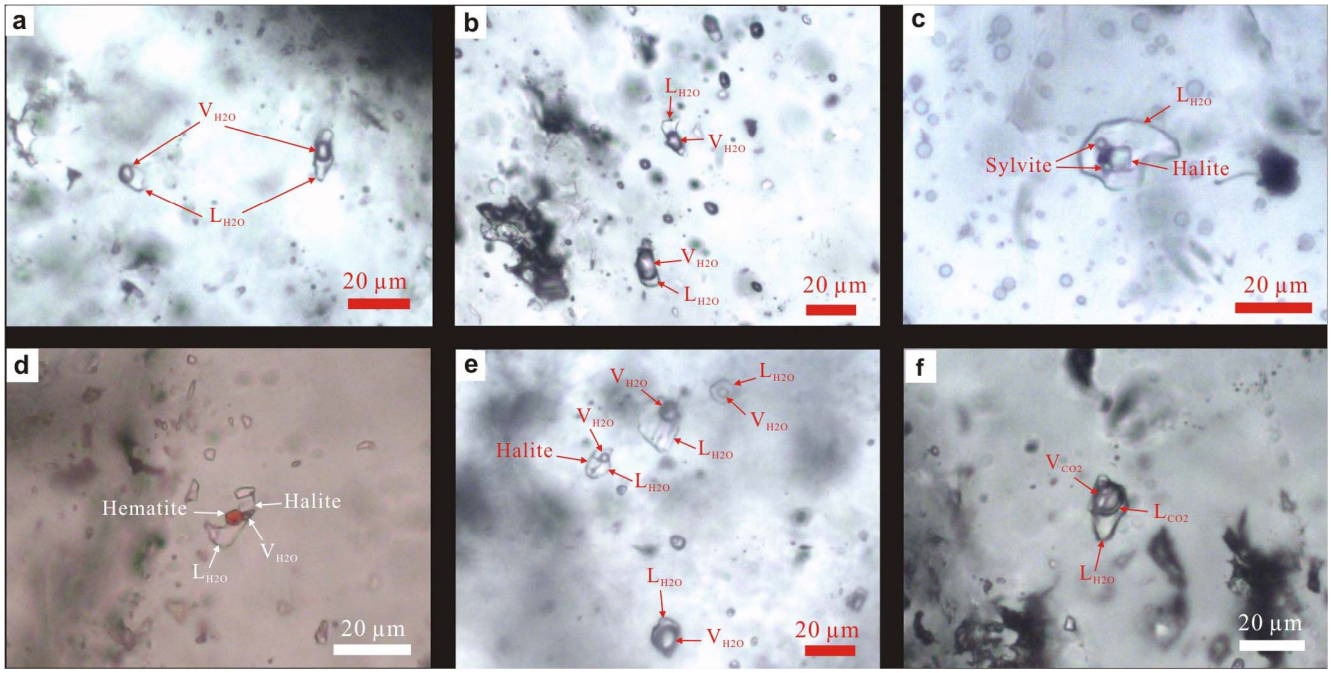

Fig. 12. Microphotographs of different types of fluid inclusions from the hydrothermal veins. (a) shows the L-type fluid inclusions in pegmatitic vein. (b) shows the V-type fluid inclusion. (c) shows the multiple daughter minerals (sylvite + halite) in a D-type fluid inclusion. (d) illustrates hematite + halite daughter minerals in a D-type fluid inclusion. (e) indicates the coexistence of D-type, L-type and V-type fluid inclusions. (f) shows a typical C-type fluid inclusion. Abbreviations: V, vapor; L, liquid.

originated from the deep asthenospheric mantle with some involvement of the EM2 or the lower crustal materials. The lithospheric mantle beneath the Zouping area was EM1 rather than EM2 during the early Cretaceous (Guo et al., 2001, 2003; Yang et al., 2012; Yang et al., 2012a, 2012b), directly precluding the participation of the EM2. The high-SiO_2 features of the quartz monzonite (SiO_2 > 63 wt%) also favor the involvement of felsic continental crust materials. Therefore, asthenospheric mantle-derived melt mixing with some crust-derived materials was likely responsible for the generation of the quartz monzonite. This way to generate adakitic rocks has been proved to be feasible, as suggested by Richards and Kerrich (2007) who considered that normal asthenosphere-derived tholeiitic to calc-alkaline magmas, interacting with crustal melts derived from amphibolites and undergoing fractional crystallization of amphibole and/or garnet, will tend to produce adakitic geochemical features. It was suggested that fractionation of 47 percent of amphibole from an andesite, or only 11 percent from a more felsic melt, can yield the adakitic features of Sr/Y > 40 and La/Yb > 20 (Richards and Kerrich, 2007). To testify this model, crustal involvement and significant fractional crystallization of amphibole and/or garnet must be assessed. Based on a mixing modeling using Sr-Nd isotopes (Langmuir et al., 1978), ~15–20% lower crust components would be required to participate in the quartz monzonite (Fig. 10a). The amounts are consistent with other studies showing that tens of percent of lower crustal components (~20%) were assimilated by asthenosphere-derived basaltic magmas to generate adakite-like rocks (Richards and Kerrich, 2007). The neglectable variations of $(^{87}Sr/^{86}Sr)_i$ and $\varepsilon_{Nd}(t)$ values, which change little with increasing SiO_2 and decreasing MgO (Fig. 16a and b), confirm that crustal involvement mainly occurred in the magma chamber through magma mixing rather than through assimilation during magma ascent. Considering the markedly high Sr/Y (63–106) and La/Yb (33–38) ratios of the quartz monzonite, the magma mixing probably occurred at the base of the lower crust, where garnet would be retained or fractionated from the magma to generate the adakitic features (Richards and Kerrich, 2007). In addition, significant fractionation of amphibole is indeed supported by some geochemical evidence: (1) The MgO and $Fe_2O_3{}^T$ contents decrease with increasing SiO_2 (Fig. 16c and d), suggesting the fractionation of ferromagnesian silicate minerals such as amphibole; (2) Most importantly,

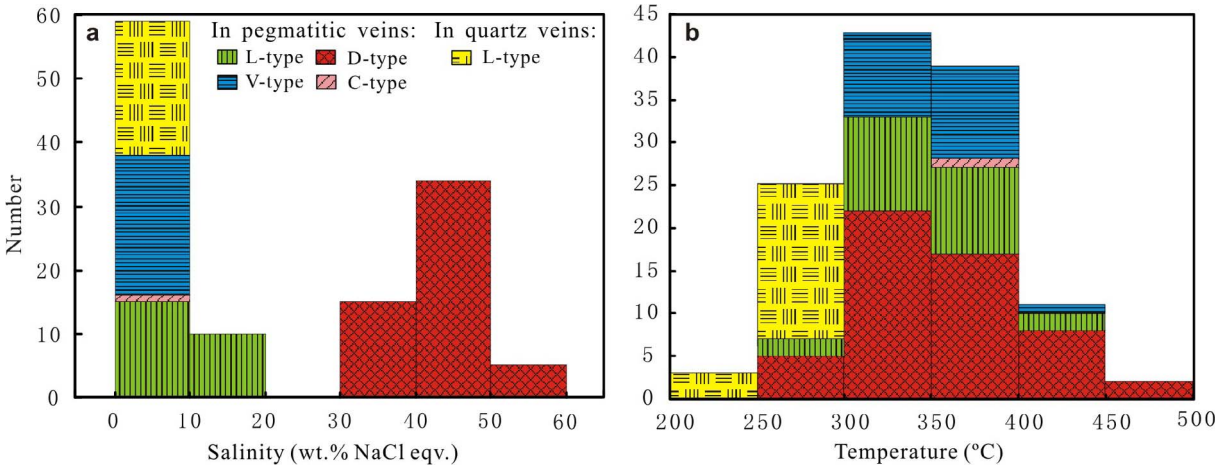

Fig. 13. Histograms showing (a) salinities and (b) homogenization temperatures of different types of fluid inclusions.

Table 11
Major and trace element concentrations (ppm) of fluid inclusions from hydrothermal veins.

	Spot	^{23}Na	^{39}K	^{55}Mn	^{57}Fe	^{65}Cu	^{66}Zn	^{85}Rb	^{88}Sr	^{98}Mo	^{133}Cs	^{137}Ba	^{182}W	^{205}Tl	^{208}Pb	K/Na	Mn/Na	Fe/Na	Cu/Na	Zn/Na	Pb/Na
Fluid inclusions in ore-forming pegmatitic veins																					
D-type	13ZP11-01	83,485	24,575	9618	40,547	5998	2165	391	331	97.9	135	520	110	–	1999	0.29	0.12	0.49	0.07	0.03	0.024
	13ZP11-02	74,640	23,874	10,615	43,561	5364	3668	332	322	365	81.0	510	107	–	1919	0.32	0.14	0.58	0.07	0.05	0.026
	13ZP11-03	65,189	23,681	12,342	26,839	686	2868	327	350	200	117	367	–	–	1604	0.36	0.19	0.41	0.01	0.04	0.025
	13ZP11-04	90,839	30,435	16,834	38,506	3287	3800	337	326	153	199	407	62.2	11.0	1817	0.34	0.19	0.42	0.04	0.04	0.020
	13ZP11-05	60,440	22,780	9790	33,538	2700	2326	258	641	225	81.8	431	80.2	31.8	1586	0.38	0.16	0.55	0.04	0.04	0.026
	13ZP11-06	94,740	23,005	17,024	39,303	4445	2747	295	433	101.4	113	432	14.8	–	1839	0.24	0.18	0.41	0.05	0.03	0.019
	13ZP11-07	93,178	34,164	16,410	38,733	4572	3474	391	322	115	165	480	9.1	–	2089	0.37	0.18	0.42	0.05	0.04	0.022
	13ZP11-08	77,187	28,321	10,794	53,735	5188	2449	281	297	320	106	581	124	–	1495	0.37	0.14	0.70	0.07	0.03	0.019
	13ZP15-01	89,793	33,587	10,899	47,659	9010	2761	321	331	432	130	555	131	13.1	2122	0.37	0.12	0.53	0.10	0.03	0.024
	13ZP15-02	104,002	23,203	8254	38,295	4794	2058	213	233	200	89.8	382	16.6	16.4	1865	0.22	0.08	0.37	0.05	0.02	0.018
	13ZP15-03	91,363	41,863	12,537	51,651	7275	3472	472	275	332	155	608	87.8	21.6	2228	0.46	0.14	0.57	0.08	0.04	0.024
	13ZP15-04	95,430	43,423	13,522	44,798	2066	3659	394	356	92.2	235	731	41.5	–	2847	0.46	0.14	0.47	0.02	0.04	0.030
	13ZP15-05	81,895	38,119	13,514	50,533	8059	3061	384	358	102.7	149	591	103.1	11.4	2556	0.47	0.17	0.62	0.10	0.04	0.031
	13ZP15-06	96,564	31,765	11,092	43,889	4581	2572	309	211	277	96.3	337	38.2	15.3	1989	0.33	0.11	0.45	0.05	0.03	0.021
	13ZP15-07	95,779	39,079	9382	26,276	8835	1334	262	97.9	347	128	–	–	–	2171	0.41	0.10	0.27	0.09	0.01	0.023
	13ZP15-08	97,535	33,829	11,431	43,157	5207	2659	347	184	243	100.1	522	87.1	8.87	1903	0.35	0.12	0.44	0.05	0.03	0.020
	13ZP15-09	102,844	32,792	10,312	41,395	8045	2194	266	237	303	62.7	218	118	9.46	1841	0.32	0.10	0.40	0.08	0.02	0.018
	13ZP15-10	97,461	22,004	9416	35,188	1485	1880	227	271	77.6	116	444	33.7	–	1741	0.23	0.10	0.36	0.02	0.02	0.018
	13ZP15-11	81,476	52,166	13,595	42,902	3173	3566	441	194	241	110	479	86.8	14.6	2463	0.64	0.17	0.53	0.04	0.04	0.030
	13ZP15-12	91,102	43,247	19,117	38,999	1977	6132	508	433	146	614	1128	83.1	15.2	3315	0.47	0.21	0.43	0.02	0.07	0.036
	13ZP15-13	95,681	33,711	9041	45,486	5923	2199	262	151	314	79.2	303	141	16.2	2101	0.35	0.09	0.48	0.06	0.02	0.022
	13ZP15-14	59,358	19,284	5013	20,070	4566	1410	206	23	173	52.5	–	50.4	–	1149	0.32	0.08	0.34	0.08	0.02	0.019
	13ZP15-15	100,277	30,399	10,881	38,251	4983	2351	283	122	276	118	147	68.0	–	2400	0.30	0.11	0.38	0.05	0.02	0.024
	13ZP15-16	69,193	23,005	6737	26,343	3761	1989	251	95	214	79.4	143	85.2	–	1259	0.33	0.10	0.38	0.05	0.03	0.018
	13ZP15-17	90,210	33,948	11,983	45,980	6122	5012	410	119	188	134	210	93.8	–	2148	0.38	0.13	0.51	0.07	0.06	0.024
	13ZP15-18	85,594	30,327	14,955	51,620	1317	1026	343	433	210	43.7	80.0	53.6	–	172	0.35	0.17	0.60	0.02	0.01	0.002
	13ZP15-19	81,995	38,629	17,726	58,909	5416	3259	415	327	186	136	605	81.3	15.6	2109	0.47	0.22	0.72	0.07	0.04	0.026
	13ZP15-20	86,650	43,443	13,265	41,858	4968	4118	426	279	216	286	676	103.0	13.0	2304	0.50	0.15	0.48	0.06	0.05	0.027
	13ZP15-21	102,837	24,706	8619	46,726	7432	2324	228	132	351	85.4	176	130	–	1670	0.24	0.08	0.45	0.07	0.02	0.016
	13ZP21-01	86,000	31,914	7775	33,105	5085	1925	279	154	200	250	219	26.9	–	1275	0.37	0.09	0.38	0.06	0.02	0.015
	13ZP21-02	109,175	42,224	3146	34,660	10,432	1513	378	120	856	53.2	26.1	35.3	9.71	1470	0.39	0.03	0.32	0.10	0.01	0.013
	13ZP21-03	104,294	40,400	7713	29,844	1834	2670	348	190	165	293	230	–	15.3	1751	0.39	0.07	0.29	0.02	0.03	0.017
	13ZP21-04	105,416	42,632	4253	42,115	7903	2235	372	277	494	97.4	199	30.5	16.6	2038	0.40	0.04	0.40	0.07	0.02	0.019
	13ZP21-05	103,782	49,581	3385	38,759	8947	2480	317	106.0	687	80.6	59.9	21.3	13.9	1673	0.48	0.03	0.37	0.09	0.02	0.016
	13ZP21-06	111,030	38,618	9450	33,420	825	2517	305	308	62.1	381	531	79.0	17.0	1503	0.35	0.09	0.30	0.01	0.02	0.014
	13ZP21-07	95,012	46,112	4396	30,093	8905	2573	495	140	658	92.1	42.6	27.1	7.91	1776	0.49	0.05	0.32	0.09	0.03	0.019
	13ZP21-08	99,531	51,280	10,369	19,311	2158	3189	580	773	135	377	1547	–	13.1	1400	0.52	0.10	0.19	0.02	0.03	0.014
	13ZP21-09	90,877	53,483	8860	44,309	5658	2542	391	164	476	204	203	35.3	–	1763	0.59	0.10	0.49	0.06	0.03	0.019
	13ZP21-10	79,944	37,500	8181	54,239	6009	2208	346	78.2	609	86.3	86.5	71.8	8.34	935	0.47	0.10	0.68	0.08	0.03	0.012
	13ZP21-11	109,014	37,778	7914	20,042	1289	2748	444	260	45	336	88.8	11.82	–	1457	0.35	0.07	0.18	0.01	0.03	0.013
	13ZP21-12	123,425	30,865	5963	26,901	3363	2352	242	163	136	101.8	123.4	44.0	–	2618	0.25	0.05	0.22	0.03	0.02	0.021
	13ZP21-13	106,023	39,397	8379	38,130	6432	2460	343	226	149	125.2	243	71.5	13.7	2002	0.37	0.08	0.36	0.06	0.02	0.019
	13ZP21-14	88,707	39,210	8134	29,237	2427	2602	359	456	133	257	353	35.8	11.8	1598	0.44	0.09	0.33	0.03	0.03	0.018
	13ZP21-15	97,401	42,652	3410	31,002	7737	2782	364	98.4	744	75.7	85.6	24.5	42.3	1391	0.44	0.04	0.32	0.08	0.03	0.014
	13ZP21-16	103,543	35,005	6206	31,489	4408	2619	376	165	295	238	95.1	51.6	–	1352	0.34	0.06	0.30	0.04	0.03	0.013
Avg.		92,220	35,156	10,050	38,476	4992	2710	345	257	274	157	377	66.0	15.3	1838	0.38	0.11	0.43	0.05	0.03	0.020
L-type	13ZP11-09	18,837	3996	–	–	306	–	–	13.2	–	–	–	–	–	65.5	0.21	–	–	0.02	–	0.003
	13ZP11-10	18,163	6689	726	–	295	1009	–	17.2	–	–	–	–	–	135	0.37	0.04	–	0.02	0.06	0.007
	13ZP11-11	14,530	3590	509	–	130	–	52.9	21.7	–	–	50.8	–	–	301	0.25	0.04	–	0.01	–	0.021
	13ZP11-12	13,338	2131	–	–	9	33	4.42	18.2	–	–	9.6	–	–	1.57	0.16	–	–	0.00	0.00	0.000
	13ZP11-13	23,881	2590	–	–	270	–	–	–	–	–	–	–	–	92	0.11	–	–	0.01	–	0.004
	13ZP11-14	22,790	4192	–	–	87	–	–	75.7	–	37.4	–	–	–	25.4	0.18	–	–	0.00	–	0.001

(continued on next page)

Table 11 *(continued)*

	Spot	^{23}Na	^{39}K	^{55}Mn	^{57}Fe	^{65}Cu	^{66}Zn	^{85}Rb	^{88}Sr	^{98}Mo	^{133}Cs	^{137}Ba	^{182}W	^{205}Tl	^{208}Pb	K/Na	Mn/Na	Fe/Na	Cu/Na	Zn/Na	Pb/Na
	13ZP11-15	20,199	4112	1248	–	–	191	42.0	140	–	18.1	153	–	–	309	0.20	0.06	–	–	0.01	0.015
	13ZP11-16	16,443	5444	650	–	350	313	62.8	29.1	–	20.4	–	–	–	264	0.33	0.04	–	0.02	0.02	0.016
	13ZP11-17	15,490	1397	–	–	72	–	–	128	–	17.6	22.3	–	–	–	0.09	–	–	0.00	–	–
	13ZP11-18	13,421	1208	–	–	–	–	–	14.1	–	–	–	–	–	–	0.09	–	–	–	–	–
	13ZP15-22	18,840	8474	–	–	7542	–	–	30.5	–	–	–	–	–	–	0.45	–	–	0.40	–	–
	13ZP15-23	14,067	4581	–	–	–	–	–	139	–	58.6	199	–	–	–	0.33	–	–	–	–	–
	13ZP15-24	11,253	5351	–	–	794	–	118	29.6	–	–	–	–	–	15.1	0.48	–	–	0.07	–	0.001
	13ZP15-25	9291	2123	–	–	6110	–	–	–	–	–	–	–	–	25.9	0.23	–	–	0.66	–	0.003
	13ZP15-26	18,224	4565	1258	6445	7059	277	63.0	105	–	41.7	91	–	–	205	0.25	0.07	0.35	0.39	0.02	0.011
	13ZP15-27	17,129	5430	–	–	–	–	187	197	–	131	166	–	–	–	0.32	–	–	–	–	–
	13ZP15-28	27,874	6394	–	–	6500	–	–	–	–	–	139	–	–	35.4	0.23	–	–	0.23	–	0.001
	13ZP21-17	14,090	5047	–	–	849	–	28.9	–	–	–	–	–	–	71	0.36	–	–	0.06	–	0.005
	13ZP21-18	12,019	2802	893	–	1028	330	36.2	39.9	35.0	–	27.1	–	–	285	0.23	0.07	–	0.09	0.03	0.024
	13ZP21-19	21,600	10479	1867	5838	1301	610	88	32.4	74.2	27.9	48.8	15.8	–	372	0.49	0.09	0.27	0.06	0.03	0.017
	13ZP21-20	25,362	8558	1307	7161	1318	598	98	39.7	66.9	60.8	–	–	–	410	0.34	0.05	0.28	0.05	0.02	0.016
	13ZP21-21	19,320	5094	–	–	417	362	43.6	3.08	9.3	27.2	–	–	–	286	0.26	–	–	0.02	0.02	0.015
Avg.		17553	4738	1057	6481	2389	414	68.7	59.7	46.3	44.1	91			170	0.27	0.06	0.30	0.12	0.02	0.010
V-type	13ZP11-19	7112	1114	–	–	2949	–	–	6.90	–	–	–	–	–	–	0.16	–	–	0.41	–	–
	13ZP11-20	12,936	3373	430	4941	3376	442	31.9	40.4	–	–	–	–	–	36.9	0.26	0.03	0.38	0.26	0.03	0.003
	13ZP15-29	4162	1646	177	–	3560	–	–	–	–	–	–	–	–	30.9	0.40	0.04	–	0.86	–	0.007
	13ZP15-30	9308	4603	593	3555	1155	190	37.0	23.3	–	–	–	–	–	124	0.49	0.06	0.38	0.12	0.02	0.013
	13ZP15-31	11,200	2938	–	–	10859	–	–	–	–	–	–	–	–	50.3	0.26	–	–	0.97	–	0.004
	13ZP15-32	6530	5864	–	–	4906	–	33.8	36.9	–	16.89	–	–	–	–	0.90	–	–	0.75	–	–
	13ZP15-33	4264	828	–	–	3326	–	–	3.69	–	–	–	–	–	18.6	0.19	–	–	0.78	–	0.004
	13ZP15-34	3376	1523	–	–	2421	–	–	–	–	–	–	–	–	5.83	0.45	–	–	0.72	–	0.002
	13ZP21-22	10,463	4553	653	3940	1622	151	29.6	3.26	32.0	15.2	–	–	–	92.4	0.44	0.06	0.38	0.16	0.01	0.009
	13ZP21-23	5354	2385	465	–	789	347	–	–	–	13.3	–	10.50	–	86.4	0.45	0.09	–	0.15	0.06	0.016
	13ZP21-24	5342	2102	–	–	613	–	–	–	–	–	–	–	–	31.0	0.39	–	–	0.11	–	0.006
	13ZP21-25	7797	6165	428	4025	943	395	48.6	16.7	53.2	11.1	9.04	2.49	–	149	0.79	0.05	0.52	0.12	0.05	0.019
	13ZP21-26	6069	4742	–	–	6791	374	–	–	–	–	–	–	–	98.3	0.78	–	–	1.12	0.06	0.016
	13ZP21-27	6225	2922	249	1675	1211	121	23.0	5.15	41.8	5.69	–	–	–	87.9	0.47	0.04	0.27	0.19	0.02	0.014
	13ZP21-28	11,662	4010	562	3215	3386	283	39.7	–	81.7	15.7	–	15.98	–	180	0.34	0.05	0.28	0.29	0.02	0.015
	13ZP21-29	9660	2512	–	–	1047	283	24.6	–	27.1	–	–	–	–	50.1	0.26	–	–	0.11	0.03	0.005
Avg.		7591	3205	444	3559	3060	287	33.5	17.04	47.2	12.97				74.4	0.44	0.05	0.37	0.45	0.04	0.010
Fluid inclusions in post-mineralization quartz veins																					
L-type	13ZP29-01	21,850	3701	–	–	–	–	17.0	–	–	–	–	–	–	–	0.17	–	–	–	–	–
	13ZP29-02	24,225	8653	–	–	–	–	10.7	0.84	–	3.43	–	1.40	–	–	0.36	–	–	–	–	–
	13ZP29-03	17,054	2603	–	–	–	–	13.5	–	–	–	–	–	–	–	0.15	–	–	–	–	–
	13ZP29-04	21,469	5626	–	–	–	–	17.8	3.16	–	–	–	5.27	–	–	0.26	–	–	–	–	–
	13ZP29-05	19,123	3876	–	–	–	–	–	–	–	–	–	–	–	–	0.20	–	–	–	–	–
	13ZP29-06	15,563	1797	–	–	–	–	–	–	–	–	–	–	–	–	0.12	–	–	–	–	–
	13ZP29-07	23,804	5185	–	–	–	–	–	–	–	–	–	–	–	–	0.22	–	–	–	–	–
	13ZP29-08	21,240	3377	–	–	–	–	–	2.09	–	–	–	4.09	–	–	0.16	–	–	–	–	–
	13ZP29-09	16,734	2857	–	–	–	–	–	–	–	7.38	–	4.71	–	–	0.17	–	–	–	–	–
	13ZP29-10	24,525	4118	–	–	–	–	–	5.92	–	–	–	–	–	–	0.17	–	–	–	–	–
	13ZP29-11	25,766	6347	–	–	–	–	–	–	–	–	–	3.45	–	–	0.25	–	–	–	–	–
	13ZP29-12	15,719	4772	–	–	–	–	20.1	–	–	–	14.4	–	–	–	0.30	–	–	–	–	–
	Average	20,589	4409					15.8	3.00		5.41		3.78			0.21					

"–" indicates the concentration below the detection limit.

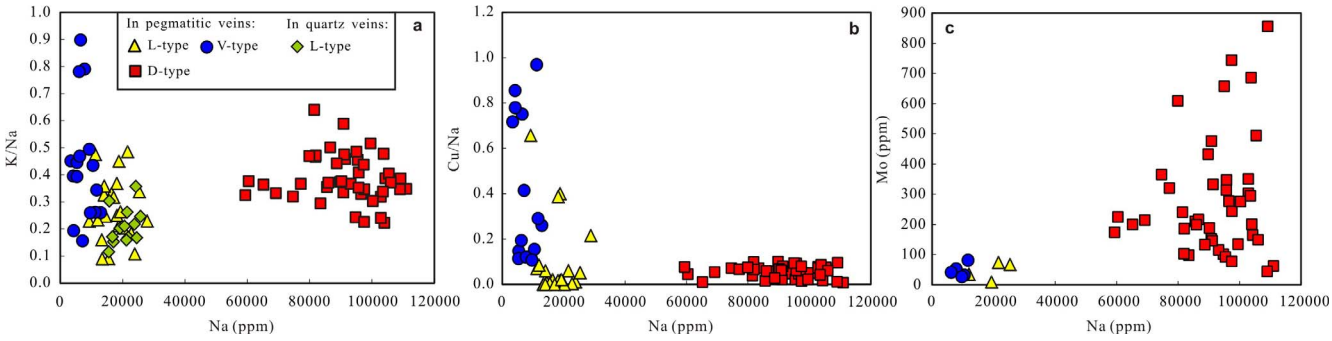

Fig. 14. Plots of (a) K/Na vs. Na, (b) Cu/Na vs. Na and (c) Mo vs. Na for the fluid inclusions from the Wangjiazhuang deposit.

the obvious decrease of Nb/Ta ratios and the increase of Zr/Sm ratios with increasing SiO_2 (Fig. 16e and f), which are mainly controlled by low-Mg amphibole due to the preferential retention of Nb and Sm in such amphibole (Foley et al., 2002; Condie, 2005), clearly indicate the fractional crystallization of low-Mg amphibole. Therefore, magma mixing between the asthenospheric mantle- and lower crust-derived melts at the base of the lower crust, coupled with significant fractionation of amphibole, is considered as the most applicable way for the generation of the adakitic quartz monzonite in this study.

Zircon saturation thermometry (T_{Zr}) provides a simple and robust means of estimating magma temperatures from bulk-rock compositions (Watson and Harrison, 1983; Miller et al., 2003). It has been well applied in a wide range of intermediate to felsic melts (e.g., Watson and Harrison, 1983; Hanchar and Watson, 2003; Miller et al., 2003). Based on this thermometry, the calculated T_{Zr} for the quartz monzonite varies from 732 °C to 761 °C (average at 746 ± 12 °C, 1SD, n = 5) (Table 4). If the T_{Zr} is valid, then the crystallization pressure of the quartz monzonite can be determined by the titanium-in-quartz thermobarometer (P_{Ti}) of Huang and Audétat (2012). As a result, the calculated P_{Ti} changes from 0.82 to 1.54 kbar (average at 1.1 ± 0.2 kbar, 1SD, n = 17) (Table 6). On the assumption that the average density of the crust is approximately 2800 kg/m^3 (Rudnick and Fountain, 1995), the pressures correspond to the depths of 3.0–5.6 km (average at 4.0 ± 0.7 km, 1SD, n = 17). The above P-T results can be examined by other thermobarometers. Ti-in-zircon thermometer (T_{Ti}) is another useful thermometer which has been widely applied to igneous and metamorphic rocks in recent years (e.g., Watson et al., 2006; Baldwin et al., 2007; Ferry and Watson, 2007; Fu et al., 2008; Hiess et al., 2008). By using the revised Ti-in-zircon thermometer (Ferry and Watson, 2007), the calculated crystallization temperatures of the zircon grains (T_{Ti}) from the quartz monzonite vary from 755 °C to 807 °C (average at 778 °C) (Table 5). In this thermometer, the pressure dependence is approximately 50 °C/GPa (Ferry and Watson, 2007), and thus the pressure effect should be corrected (Fu et al., 2008). If we use 1.1 kbar (the average P_{Ti}) to correct the temperature, the final crystallization temperatures of the zircon grains are 710–762 °C (average at 733 ± 16 °C, 1SD, n = 20) (Table 5). The average T_{Ti} is well consistent with the T_{Zr} within errors, implying that the calculated P-T conditions for the quartz monzonite are reliable. The crystallization temperature (746 ± 12 °C) of the quartz monzonite is similar to many other ore-forming porphyries (e.g., Cao et al., 2014; Xu et al., 2014; Tapster et al., 2016), but the emplacement depth (4.0 ± 0.7 km) is a little bit deeper than most ore-forming rocks of porphyry copper deposits (range from ~1 to 6 km and average at 1.9 km, Kesler and Wilkinson, 2008). The relatively deeper emplacement depth thus can explain the non- porphyritic texture of the quartz monzonite.

6.2. Origin of the ore-forming materials

The Wangjiazhuang Cu-Mo deposit (128.3 Ma) is exclusively hosted in the quartz monzonite (Fig. 2a), and basically coincides with the emplacement of the host rock (128.8 Ma). The close spatial and temporal relationships imply their genetic association. In addition, the quartz monzonite has the highest Cu (77–840 ppm) and Mo (1.3–11.9 ppm) concentrations among the rocks surrounding the deposit (Li and Yuan, 1991; Kong et al., 2006), becoming the most favorable source rock of the ore-forming metals. Microthermometric results show that the ore-forming fluids are featured by high temperature (up to 466 °C) and high salinity (up to 50% wt.% NaCl equivalent). Such high-temperature fluid with high salinity is commonly indicative of magmatic differentiation origin (Roedder, 1992). Therefore, the ore-forming fluids of the Wangjiazhuang deposit were most likely derived from the

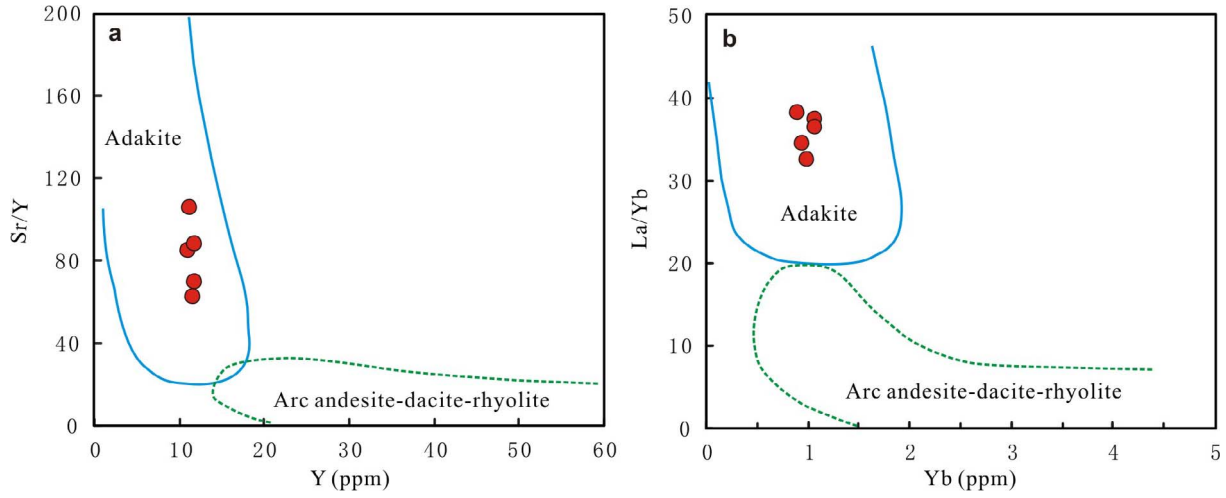

Fig. 15. Plots of (a) Sr/Y vs. Y and (b) La/Yb vs. Yb for the quartz monzonite (modified after Castillo, 2012).

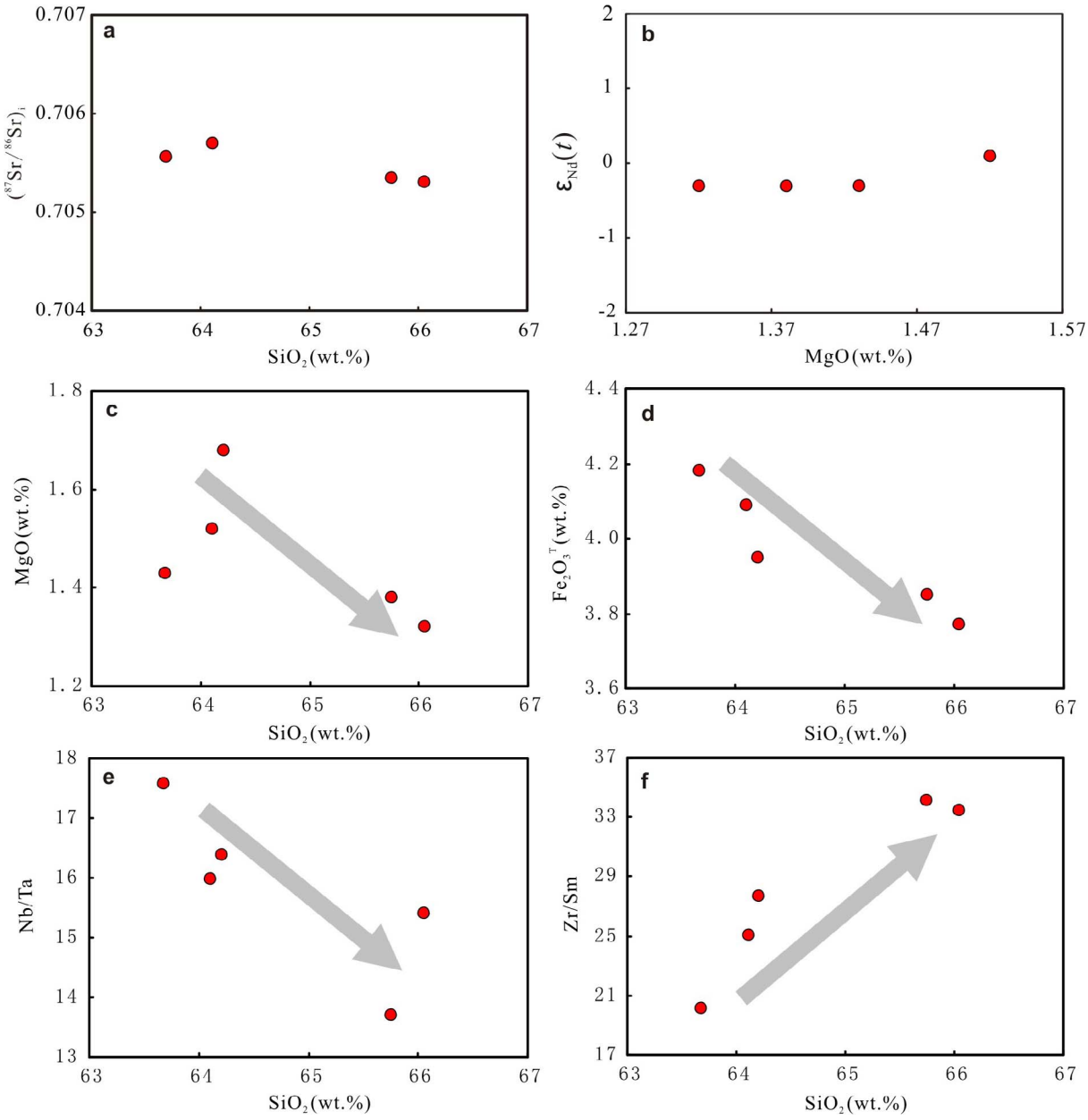

Fig. 16. Plots of (a) $(^{87}Sr/^{86}Sr)_i$ vs. SiO_2, (b) $\varepsilon_{Nd}(t)$ vs. MgO, (c) MgO vs. SiO_2, (d) $Fe_2O_3^T$ vs. SiO_2, (e) Nb/Ta vs. SiO_2 and (f) Zr/Sm vs. SiO_2, illustrating neglectable crustal contamination and significant fractional crystallization of amphibole during magma ascent.

magmatic differentiation of the quartz monzonite.

The lithologies of the early Cretaceous igneous rocks in the study area vary widely from gabbros/basalts to granites/rhyolites, but why only the quartz monzonite produced Cu-Mo deposit is puzzled. It is noted that most of the igneous rocks in the study region were derived from the enriched lithospheric mantle (Zhang et al., 2002; Xu et al., 2004; Lan et al., 2011b; Yang et al., 2012; Yang et al., 2012a, 2012b), whereas the quartz monzonite has peculiar derivation from the deeper asthenospheric mantle. This implies that the asthenospheric mantle likely provided the initial ore-forming metals. Although the Cu content of the local asthenospheric mantle has not been reported, it can be roughly inferred from the asthenosphere-derived MORBs, which have Cu contents up to ~70 ppm (Hofmann, 1988; Kelemen et al., 2007). Primitive andesites derived from asthenospheric mantle wedge were estimated to contain Cu contents as high as 145 ppm (Gill, 1981; Richards, 2011a). These Cu contents are much higher than those of the local lower to upper crusts (27–45 ppm, Gao et al., 1998) and the enriched lithospheric mantle-derived gabbros (28–71 ppm, Gao and Chen, 2013). Therefore, the high Cu background in the asthenosphere indicates that it is a favorable source of Cu.

The sources of Mo are more diverse. In general, both the crust (Farmer and DePaolo, 1984; Stein et al., 1997; Klemm et al., 2008) and the mantle (Westra and Keith, 1981; Audétat, 2010; Pettke et al., 2010) have been considered to be the potential sources of Mo. Many studies showed that Re content in molybdenite is an effective indicator to distinguish the mantle or crustal origin of Mo. For example, Mao et al. (1999) reported the phenomenon that Re contents in molybdenites decrease from mantle to I-type and then to S-type granite-related deposits. Stein et al. (2001) proposed that molybdenites associated with mantle underplating or metasomatism, or melting of mafic and ultramafic rocks have significantly higher Re contents than those genetically related to crustal rocks or organic-poor sedimentary sequences. The remarkably high Re contents in the molybdenites (177–364 ppm) of the Wangjiazhuang deposit indicate that the Mo was likely originally derived from the mantle. This origin is in accordance with host quartz monzonite. In addition, the mantle origin of the Mo is corroborated by

the low Re contents (< 10 ppm) in the molybdenites from the Jurassic crust-derived skarn- and porphyry-type Mo deposits in the neighboring Jiaobei Terrane (Ding et al., 2012).

He-Ar isotopes have been proved to be one of the most effective tracers to identify mantle components in hydrothermal fluids (e.g., Stuart et al., 1995; Hu et al., 2012; Xie et al., 2016). For example, it shows that the mantle products have $^{3}He/^{4}He$ ratios of 6–9 Ra, whereas those of the crustal products are 0.01–0.05 Ra (Allégre et al., 1986/1987; Stuart et al., 1995). The large difference of isotopic compositions between the mantle and crustal reservoirs thus allows the noble gases to provide a unique insight into processes where mantle volatiles have been involved (Stuart et al., 1995). The sulfides of the Wangjiazhuang deposit show ^{3}He and ^{4}He contents similar to those of the mantle reservoir (Fig. 11a), and have R/Ra and $^{40}Ar*/^{4}He$ ratios close to the mantle products (Fig. 11b), strongly suggesting the mantle origin of the ore-forming materials, although minor crustal components were probably also involved in. Therefore, based on the above results, both the Cu and Mo metals of the Wangjiazhuang deposit were originally derived from the asthenospheric mantle. This conclusion can well explain the rarity of Cu-Mo deposits in the study area (at the inner domain of the eastern NCC) during the early Cretaceous. It is likely due to the scarce development of the deeper asthenospheric mantle-derived rocks during that time.

6.3. Enrichment and transportation of the ore-forming metals from the magma to the hydrothermal fluids

The Wangjiazhuang Cu-Mo deposit has two types of mineralization, one is the pegmatitic vein-type and the other is the stockwork-/disseminated-type. Because the host granitoid is not a porphyry and the pegmatitic vein-type rather than the stockwork-/disseminated-type mineralization holds the majorities of the metal reserves, the deposit cannot be considered as a porphyry deposit. Nonetheless, it indeed shares many characteristics with porphyry deposits: (1) showing similar alteration types, such as potassic, potassic-silicic, sericitic, chloritic and kaolinitic alterations (Fig. 2); (2) having high-temperature (up to 466 °C), high-salinity (up to 50% wt.% NaCl eqv.) and highly oxidized (hematite occurs in fluid inclusions) ore-forming fluids; (3) also having the stockwork-/disseminated-type mineralization featured in porphyry deposits; (4) being regionally associated with volcanics which are common in porphyry systems (Sillitoe, 2010). Therefore, the magmatic-hydrothermal processes of the Wangjiazhuang deposit can be generally analogous to those of the porphyry deposits.

High water contents (Richards, 2011a, 2011b), high oxidation state (Mungall, 2002) and sulfide saturation (Wilkinson, 2013) of the magma have been considered to be the crucial factors controlling the generation of a porphyry deposit. Amphibole and biotite are indicators of high water contents in magmas (Ridolfi et al., 2010; Richards, 2011b; Richards et al., 2012), of which the biotite is abundant in the quartz monzonite (Fig. 3a and b), suggesting the water contents in the magma of the quartz monzonite were probably ≥ 4 wt% (Richards, 2011b; Richards et al., 2012). Such high water contents could facilitate the intense alteration during the magmatic-hydrothermal processes and promote the transportation of ore-forming metals from the magma into the hydrothermal fluids. The processes are evidenced by the widespread alterations in the Wangjiazhuang deposit. During potassic alteration, the obvious losses of $Fe_2O_3^T$, MgO, CaO, Cr, Ni, Rb, Sr and Ba (Fig. 8a and b), combined with petrographic observations, indicate the significant breakdown of biotite and plagioclase in the quartz monzonite. Most importantly, the evident gains of K_2O, N_2O and Cu imply that the transportation of Cu from the magma into the hydrothermal fluids was promoted by the alkali fluids (enriched in K and Na). Such alkali fluids could also have important effect for Mo extracting from the magma, as supported by experiments showing that alkali chloride-rich magmatic-hydrothermal fluids are extremely efficient in extracting Mo from silicate liquids (Webster, 1997). Subsequent sericitic alteration overprinting on the potassic alteration resulted in the losses of $Fe_2O_3^T$, MgO, CaO, Na_2O, Cr, Cu, Zn, Zr, Sr, Ba, La, Ce, Nd and Pb and the gains of K_2O and Rb (Fig. 8c and d), indicating the continuous breakdown of the mafic minerals and the decomposition of some accessory minerals (such as zircon and sphene) as well as the transformation of feldspar into sericite. Notably, the Cu contents show significant decrease from the potassic alteration to the sericitic alteration (Fig. 8d), which likely suggest the Cu precipitation prior to the sericitic alteration. The coexistence of quartz + biotite + K-feldspar + Cu-bearing sulfides (Fig. 3g–k) confirms the Cu precipitation simultaneous to the potassic-silicic alteration. Copper mineralization closely associated with potassic alteration has been observed in numerous porphyry deposits worldwide (e.g., Ulrich and Heinrich, 2001; Einaudi et al., 2003; Sillitoe, 2010; Sun et al., 2013). Such an association can be explained by the phase equilibria for the system K_2O-Al_2O_3-SiO_2-H_2O-KCl-HCl, which show that in high KCl/HCl conditions (e.g., the occurrence of K-feldspar and/or biotite), the potassic alteration would dominate at the temperature as low as ~450 °C (Seedorff et al., 2005), close to the dramatic decrease of Cu solubility (as chloride species) in the fluids (~400° to 300 °C interval, Hezarkhani et al., 1999; Redmond et al., 2004; Landtwing et al., 2005; Klemm et al., 2007; Richards, 2011a). In addition, potassic alteration can strongly change the pH conditions of the magmatic-hydrothermal systems, initiating the precipitation of sulfide minerals (Richards, 2011a; Sun et al., 2013).

The quartz monzonite shows mafic mineral assemblages of biotite (with high Mg/Fe ratio > 2) + magnetite + sphene, which are similar to those of the oxidized granitoids (Wones, 1981; Takagi and Tsukimura, 1997). In addition, it has much higher zircon Ce^{4+}/Ce^{3+} and whole-rock Fe_2O_3/FeO ratios than those of the contemporaneous enriched lithospheric mantle-derived rocks (Figs. 9b and 17), strongly suggesting its oxidized characteristics. Based on the $\log(Fe_2O_3/FeO)$ value (Blevin, 2004), the f_{O2} (oxygen fugacity) of the quartz monzonite is far above the fayalite-magnetite-quartz oxygen buffer (FMQ) (Fig. 17). Since sulfur speciation in silicate melts will change from sulfide to sulfate in the f_{O2} range of FMQ < f_{O2} < FMQ + 2 (Carroll and Rutherford, 1988; Jugo, 2009; Jugo et al., 2010; Yang, 2012), sulfur speciation in the quartz monzonite magma was likely dominated by sulfate. This could be favorable for the Cu enrichment in the magma. Experiments have showed that sulfate in the oxidized melts can enhance the S solubility and prevent Cu deposition by suppressing Cu-bearing sulfides crystallization in the magma (Jugo et al., 2010; Lee et al., 2012; Chiaradia, 2014). In addition, Mo solubility in the magma can also benefit from the high oxygen fugacity. In the oxidized silicate

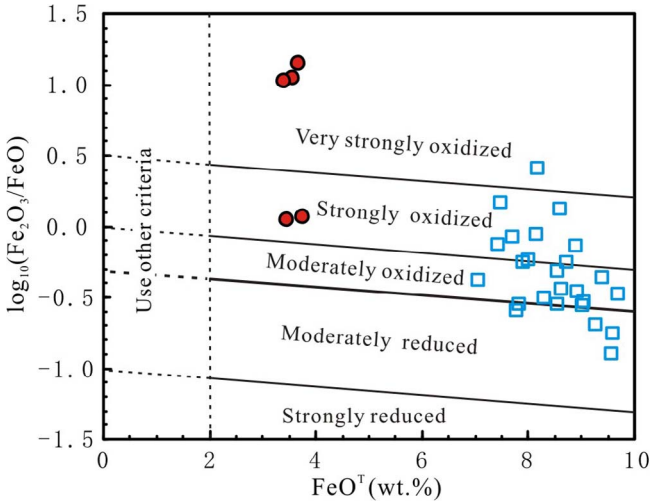

Fig. 17. Redox classification scheme for igneous rocks (modified after Blevin, 2004). The early Cretaceous enriched lithospheric mantle-derived mafic rocks are shown for comparison (data from Guo et al., 2001, 2003). The boundary between the moderately reduced and moderately oxidized fields approximates the FMQ buffer curve (Blevin, 2004).

melt, Mo^{6+} will be the dominant species of Mo, the solubility of which is higher than that of the relatively reduced Mo^{4+} (Holzheid et al., 1994; Farges et al., 2006; Sun et al., 2014). The high oxygen fugacity of the quartz monzonite also agrees well with the observations in numerous porphyry Cu (Au, Mo) deposits worldwide, which found that porphyry deposits are typically related to the magmas with high oxygen fugacity (Ballard et al., 2002; Seedorff et al., 2005; Sillitoe, 2010), probably more than two orders of magnitude higher than the fayalite-magnetite-quartz oxygen buffer (ΔFMQ + 2) (Mungall, 2002; Yang, 2012; Sun et al., 2013). Such high oxygen fugacity could be inherited by the fluids exsolved from the magma, and eventually affect the depositional ways of the ore-forming metals (Sun et al., 2013).

An oxidized hydrous magma is favored for the preliminary enrichment of the ore-forming metals, but how the metals are transported from the magma into the hydrothermal fluids and finally precipitated is also a vital problem. Fluids exsolved from the hydrous magma can occur either as a single phase of intermediate salinity fluid or as two immiscible phases including a dense, hypersaline liquid and a low-salinity vapor if the fluid has intersected its solvus (Roedder, 1992; Shinohara, 1994; Einaudi et al., 2003; Redmond et al., 2004; Sillitoe, 2010; Williams-Jones and Heinrich, 2005). In the Wangjiazhuang deposit, the coexistent vapor-rich, liquid-rich and daughter mineral-rich (mainly chlorides) fluid inclusions (Fig. 12e) with similar variations of temperatures (Fig. 13b) suggest that differentiation of the magmatic-hydrothermal fluid into a low-density vapor phase and a hypersaline liquid phase likely occurred (such as boiling, Roedder, 1992). However, it should be noted that the homogenization temperatures of these fluid inclusions mainly vary in the range of 300–400 °C (Fig. 13b), which are much lower than those of the fluids directly exsolved from the silicate melts (commonly > 500 °C, Roedder, 1992). This implies that the observed fluids could not be the direct results of magmatic exsolution and a high-temperature precursor should have operated. Such a precursor was probably a supercritical fluid with moderate salinity, as inferred from the P-T-X_{NaCl} phase diagram of H_2O-NaCl system (Williams-Jones and Heinrich, 2005; Driesner and Heinrich, 2007; Richards, 2011a). Supercritical fluid is highly mobile and has much greater potential as an efficient transporting medium for ore components (Richards, 2011a and references therein). No matter what the precursor was, the differentiation of the fluid into different phases likely contributed to the separation of Cu and Mo in the Wangjiazhuang deposit. It was observed that the Cu-rich ore bodies (represented by the number 17 orebody) are horizontally situated at shallower level while the Mo-rich ore bodies (represented by Mo-I orebody) are located at deeper depth (Fig. 2b). Because the two types of ore bodies show transitional variation (Fig. 2b) and both of them have the coexistent Cu- and Mo-bearing sulfides assemblages (e.g., chalcopyrite + bornite + molybdenite, Fig. 3j), combined with the highly concentrated mineralization ages of all types of ores (Table 3), the separation of Cu and Mo could not be attributed to the different pulses of precipitation. Alternatively, it was probably due to the different mobilities between the Cu and Mo carried by different mediums. Numerous studies have showed that Cu is mainly complexed with chlorine in the aqueous fluid exsolved from the magma above critical P-T conditions (Candela and Holland, 1984; Keppler and Wyllie, 1991; Shinohara, 1994; Webster, 1997; Berry et al., 2009), whereas below the critical P-T conditions Cu is highly partitioned into the vapor phase by complexing with $H_2S \pm SO_2$ (mainly presented as Cu(I)-S complexes, such as $Cu(HS)_2^-$ and $Cu(HS)(H_2S)$, Heinrich et al., 1999; Williams-Jones and Heinrich, 2005; Pokrovski et al., 2008; Etschmann et al., 2010; Seo et al., 2012; Sillitoe, 2010). For Mo, it is considered that Mo is mainly complexed as molybdate species (such as H_2MoO_4 and Na_2MoO_4) as well as hydroxide, oxy-chloride and oxo-chloride complexes (such as $MoO_2(OH)_2$, $MoO(OH)Cl_2$, MoO_2Cl_2) in the fluids (Candela and Holland, 1984; Cao, 1989; Keppler and Wyllie, 1991; Ulrich and Mavrogenes, 2008). The above considerations are confirmed by the LA-ICP-MS results of fluid inclusions. In the Wangjiazhuang deposit, the V-type fluid inclusions have the highest Cu/Na ratios while the D-type fluid inclusions contain the highest Mo concentrations (Fig. 14b and c), implying that the Cu and Mo were separated by vapor-rich and high-salinity liquid-rich mediums, respectively. It is deduced that the vapor-carried Cu was more mobile and thus rose to the shallower level, whereas the liquid-carried Mo was less mobile and precipitated in the deeper depth. In addition, because the Wangjiazhuang deposit is located at a volcanic caldera, the extensional faults induced by the volcanic structures could facilitate the vapor-carried Cu to precipitate in pegmatitic veins at shallow crustal level, contrasting with the stockwork-/disseminated-type mineralization in the deep.

6.4. Depositional processes of the ore-forming metals

In the Wangjiazhuang Cu-Mo deposit, it is noted that hematite crystals occur in the fluid inclusions (Fig. 12d) and some magnetite grains were observed in the ores, whereas no or little sulfates were found in the fluid inclusions as well as in the ores. In addition, the sulfur isotopic compositions ($\delta^{34}S_{CDT}$) increase from the early potassic alteration stage (−7.07‰ to −5.05‰) to the Cu-Mo mineralization stage (−3.78‰ to −1.02‰). These results suggest that the oxidation and sulfidation states had changed during the magmatic-hydrothermal processes, and the depositional processes of the ore-forming metals can be estimated from these specific phenomenons.

The deposition of hematite and magnetite requires a strong oxidizer to oxidize Fe from Fe^{2+} to Fe^{3+}. In an oxidized system, SO_2 is the dominant sulfur species in the high-temperature (> 400 °C) magmatic volatile phases (Gerlach, 1993; Rye, 1993; Oppenheimer et al., 2011; Richards, 2014), which would progressively disproportionate to H_2S and H_2SO_4 as the system cools below ~400 °C (Rye et al., 1992; Einaudi et al., 2003; Richards, 2011a, 2014):

$$4SO_2 + 4H_2O = H_2S + 3H_2SO_4 \quad (1)$$

The resultant aqueous sulfate is an effective oxidizer, and therefore the hematite or magnetite in the Wangjiazhuang deposit can be generated through ferrous iron reacting with the aqueous sulfate (Haynes et al., 1994; Reed and Palandri, 2006; Wilson et al., 2007):

$$8Fe^{2+} + 8H_2O + SO_4^{2-} = 4Fe_2O_3 + 14H^+ + H_2S \quad (2)$$

The reduction and consumption of the aqueous sulfate thus could be responsible for the lack of sulfates in the deposit. In the Reaction (1), abundant H_2S can be produced, which would promote the previously chlorine-carried Cu (Candela and Holland, 1984; Keppler and Wyllie, 1991; Shinohara, 1994; Webster, 1997; Berry et al., 2009) to be partitioned into the vapor phase by complexing with H_2S as Cu-S complexes (Heinrich et al., 1999; Williams-Jones and Heinrich, 2005; Pokrovski et al., 2008; Etschmann et al., 2010; Sillitoe, 2010; Seo et al., 2012). Accompanying this process, phase separation of the fluid occurred, as indicated by the coexistence of different types of fluid inclusions with similar temperatures (300–400 °C, Figs. 12e and 16b), generating the Cu-S enriched vapor-like fluid (represented by the Cu-rich V-type fluid inclusions). When such vapor-like fluid ascended, it cooled down and changed in acidity in contact with feldspatic wallrocks (Pokrovski et al., 2008), leading to the precipitation of ore minerals such as chalcopyrite ($CuFeS_2$) and bornite (Cu_5FeS_4) during rock-water interaction. The reactions probably proceeded in the following ways (Einaudi et al., 2003; Seo et al., 2012):

$$2Cu(HS)_2^- + 2Fe^{2+}_{(rock)} = 2CuFeS_2 + 2H^+ + H_2 \quad (3)$$

$$2Cu(HS)(H_2S) + 2Fe^{2+}_{(rock)} = 2CuFeS_2 + 4H^+ + H_2 \quad (4)$$

$$5CuFeS_2 + 2H_2O = Cu_5FeS_4 + 4FeS_2 + 2H_2 \quad (5)$$

It is noteworthy that, because the solubilities of Cu-Fe-S minerals are not significantly affected by temperature and pressure, but are strongly controlled by pH (Reed and Palandri, 2006), the mineral assemblages of

chalcopyrite + bornite + pyrite in the Wangjiazhuang deposit (Fig. 3j and k) likely indicate a pH value of ~3.5 (Reed and Palandri, 2006). The low pH value during metal precipitation is also confirmed by the Al variations in quartz. In the Wangjiazhuang deposit, the Al contents increase slightly from the quartz monzonite (135–196 ppm) to the ore-forming pegmatitic vein (170–220 ppm), but dramatically to the post-mineralization quartz vein (2073–2609 ppm) (Fig. 18). Rusk et al. (2008) suggested that Al concentrations in hydrothermal quartz are dependent on pH, and showed that the pH value decreasing from 3.5 to 1.5 could lead to the Al contents in hydrothermal quartz increasing six orders of magnitude within the temperature interval of 200–500 °C. This indicates that in the Wangjiazhuang deposit the pH value decreased drastically during/after the precipitation of the ore-forming metals. Combined with the Ti concentrations in quartz, which are commonly the function of temperature (Wark and Watson, 2006; Thomas et al., 2010; Huang and Audétat, 2012), the cooperative changes of the Ti and Al concentrations in quartz suggest the acidization of the fluids as the temperature decreased (Fig. 18).

For the Mo, the latest experimental studies suggested that hydrated trioxide species of Mo ($MoO_3(H_2O)_y$, mainly $MoO_3(H_2O)_8$) are dominant in H-O-Cl-S-bearing high-temperature (300 °C and 500 °C) vapor and low- to intermediate-density fluids (Hurtig and Williams-Jones, 2014). If this observation is true, the precipitation of Mo in the Wangjiazhuang deposit can proceed as (Hurtig and Williams-Jones, 2014):

$$2MoO_3(H_2O)_8 + 4H_2\ S = 2MoS_2 + 20H_2\ O + O_2 \quad (6)$$

During this process, the precipitation of molybdenite is mainly controlled by cooling and depressurizing, and can be enhanced by interaction with wallrocks (Hurtig and Williams-Jones, 2014).

The above reactions can well explain the negative $\delta^{34}S_{sulfide}$ values of the deposit and the increasing trend from the early to the late hydrothermal stages. In a porphyry deposit, anomalously low $\delta^{34}S_{sulfide}$ values can either be resulted from magmatic-hydrothermal processes, or from incorporation of an external, isotopically light, sulfur source such as biogenic sulfide (Ohmoto and Rye, 1979; Wilson et al., 2007). The Wangjiazhuang deposit is hosted in the quartz monzonite and broadly surrounded by volcanics, which was difficult to obtain external isotopically light sulfur derived from biogenic or sedimentary sources during its emplacement. It is therefore considered that the sulfur is primarily of magmatic derivation. During magmatic-hydrothermal processes, the changes in temperature, f_{O2} and pH of the fluid can lead to the fractionation of $\delta^{34}S$ values between the sulfides and the sulfates (Ohmoto, 1972). Typically, ^{34}S is preferentially fractionated into the oxidized sulfur species in the coexistent sulfides and sulfates and the sulfur isotopic equilibrium between them can be completed in minutes at high temperatures (~400°C, Ohmoto and Lasaga, 1982), leading to the isotopic fractionation towards lower $\delta^{34}S$ values in sulfides during cooling (Rye, 1993; Wilson et al., 2007). For instance, under high-temperature and highly oxidized conditions (e.g., T = 400 °C, H_2S/SO_4 = 0.2), the $\delta^{34}S_{sulfide}$ value in equilibrium with sulfate can be as low as −11‰, whereas under reduced conditions (e.g., H_2S/SO_4 = 5) it will shift to −1‰ (Rye, 1993). Therefore, for the Wangjiazhuang deposit, when the SO_2 disproportionated into the H_2S and H_2SO_4 in the oxidized magmatic-hydrothermal fluids at about 400 °C (Reaction (1)), the resultant H_2S would be depleted in ^{34}S and could generate significantly negative $\delta^{34}S$ values in the sulfides, as shown by the low $\delta^{34}S$ values of the pyrites in the early potassic stage (−7.02‰ to −5.05‰, Table 9). The subsequent reduction of the aqueous sulfate by reacting with the ferrous iron would produce more and more H_2S (Reaction (2)), which increased the H_2S/SO_4 ratio and thus lowered the oxygen fugacity of the hydrothermal fluid, elevating the $\delta^{34}S$ value of the H_2S. The consequent generation of sulfides by complexing with such H_2S would yield higher $\delta^{34}S$ values, resulting in the relatively high $\delta^{34}S$ values in the sulfides (Reactions (3)-(6)) of the Cu-Mo mineralization stage (−3.78‰ to −1.02‰). In conclusion, the low $\delta^{34}S_{sulfide}$ values and the increasing trend from the early to the late hydrothermal stages of the Wangjiazhuang deposit are interpreted to be the results of sulfides deposition from oxidized magmatic-hydrothermal fluids which were continuously reduced and acidized as the temperature decreased.

6.5. Implications for Cu-Mo mineralization within an intracontinental setting

It has long been recognized that the development of the Mesozoic metallogeny in the NCC was associated with the lithospheric thinning or the craton destruction (Yang et al., 2003; Mao et al., 2011, 2014; Li et al., 2012; Li and Santosh, 2014). However, the links between them remain poorly understood, particularly the mechanisms within the interior of the craton (Li and Santosh, 2014). Considering the uniqueness of these deposits, some researchers classified them into new types of deposits, such as “decratonic gold deposit” for the gold deposits (Zhu et al., 2015) and “Made in China” for the porphyry and porphyry-skarn deposits (Pirajno and Zhou, 2015). The Wangjiazhuang deposit is located at the inner domain of the eastern NCC and shows many similarities to the porphyry deposits, and therefore provides a key to understand the relationships between the porphyry or porphyry-like Cu-Mo mineralizations and the lithospheric thinning/craton destruction.

Porphyry Cu-Mo deposits are preferentially associated with highly oxidized magmas with abundant water and sulfur contents (Sillitoe, 2010). In arc settings, such magma can be produced due to the subduction of the oceanic slab which effectively transports water, sulfur and oxidative seafloor materials into the mantle source (Mungall, 2002; Richards, 2011a; Wilkinson, 2013). The ore-forming magma of the Wangjiazhuang Cu-Mo deposit was neither related to the enriched lithospheric mantle metasomatized by previous subduction-collision events, nor directly associated with the melting of a subducting oceanic slab. Actually, it was coeval with the development of A-type granites, alkaline rocks, bimodal volcanics, mafic dike swarms, carbonatite dikes, metamorphic core complexes and sedimentary basins, being associated with an intracontinental extensional environment (Ren et al., 2002; Wu et al., 2005; Windley et al., 2010; Pirajno and Zhou, 2015). Therefore, how the necessary conditions (e.g., high oxidation state, high water and sulfur contents in the magma) required for the generation of the porphyry or porphyry-like Cu-Mo deposits were achieved in this unique tectonic setting need to be evaluated. It is noted that, although the westward subduction of the Paleo-Pacific oceanic slab did not provide any melt for the ore-forming magma of this deposit, it indeed created some favorable conditions, at least in aspect of water supply. Studies on water contents in primitive basalts showed that the subcontinental lithospheric mantle beneath the eastern NCC contained

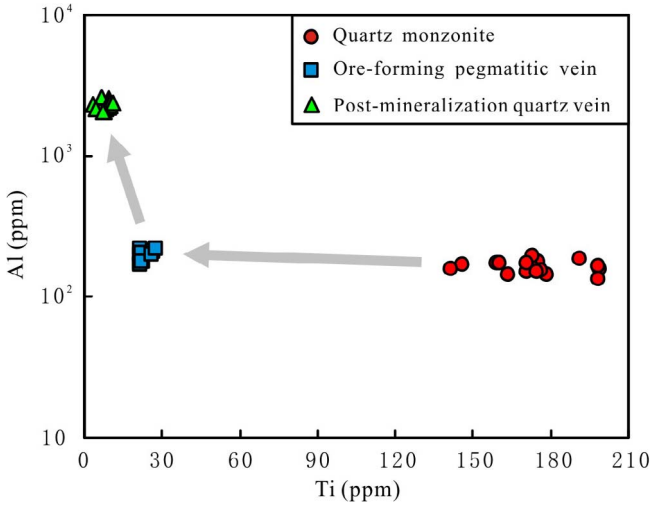

Fig. 18. Plot of Al vs. Ti concentrations in quartz.

more than 1000 ppm H_2O (by weight) during the early Cretaceous (~120 Ma) (Xia et al., 2013), which are much higher than those of the Cenozoic lithospheric mantle in the same region (< 300 ppm, Xia et al., 2010), the mid-ocean ridge basalts (50–200 ppm) and the ancient Kaapvaal cratonic mantle in South Africa (~120 ppm) (Xia et al., 2013 and references therein). Windley et al. (2010) evaluated the effects of the westward subduction of the Paleo-Pacific oceanic plate on transferring water into the deep mantle and concluded that the mantle transition zone (410–660 km depth) under the eastern NCC should be highly enriched in water due to the stagnant slab releasing water into the overlying mantle. Based on compiling and examining petrochemical characteristics of drilled basalts, Komiya and Maruyama (2007) also concluded that the western Pacific region is the place where abundant water contents have been transported into the mantle during the last 150 Ma. Experiments and simulations have proved that considerable amounts of water can be transported by the old, cold oceanic lithosphere into the mantle transition zone (Komabayashi et al., 2004; Maruyama and Okamoto, 2007). Most importantly, high-resolution geophysical imaging provides the direct evidence that such an oceanic stagnant slab occurred beneath the eastern China in the transition zone (Fukao et al., 1992; Ichiki et al., 2006; Xu et al., 2011; Zhao et al., 2017). Due to the remarkable effect on inducing asthenospheric upwelling and melting, the elevated water contents in the mantle have been typically invoked to explain the lithospheric thinning of the eastern NCC (Windley et al., 2010; Xu et al., 2011; Xia et al., 2013). In addition, the high water contents derived from the stagnant slab probably elevated the oxidation state of the asthenosphere. Frost and McCammon (2008) suggested that the release of H_2O can lead to mantle oxidation at deep regions (> 5 GPa) where CH_4 and H_2 are in equilibrium with the mantle f_{O2}. Numerous studies conducted on the subduction on oxygen fugacity have confirmed that hydrous slab-derived components can strongly oxidize the asthenospheric mantle (Wood et al., 1990; Kelley and Cottrell, 2009; Rowe et al., 2009). Crustal involvement probably can also contribute to the high oxidation state of the magma. However, the lower crustal melt involved in the ore-forming magma in this study could not be the case, because the ancient continental lower crust has significantly low oxygen fugacities (commonly between iron-wüstite and magnetite-wüstite buffers, Frost and Shive, 1986; Haggerty and Toft, 1985). Therefore, the above results suggest that the asthenosphere beneath the eastern NCC was likely hydrated and oxidized by the water released from the stagnant Paleo-Pacific slab in the transition zone, which subsequently became the favorable source for the generation of porphyry or porphyry-like deposits. The high sulfur contents required for the generation of the deposits do not seem to be a problem if the mantle source is hydrous and highly oxidized, because sulfur is not only abundant in the asthenosphere (Moore and Fabbi, 1971), but also highly fractionated into the melt under oxidized conditions (Jugo, 2009). Richards (2011b) considered that the high magmatic water content is the key factor of magmatic-hydrothermal ore-forming systems, whereas the high oxidation state and sulfur content are only secondary to the requirement for sufficient water. Based on the above discussion, it is concluded that upwelling and partial melting of the asthenosphere which had been oxidized and hydrated by sufficient water are crucial for the generation of the porphyry or porphyry-like Cu-Mo deposits within the intracontinental setting during lithospheric thinning (Fig. 19). It is necessary to note that, besides the chemical modification on the asthenosphere, the unique geodynamics could also play an important role. During the early Cretaceous, the eastern China suffered a subduction with drifting direction by the Paleo-Pacific plate (Maruyama et al., 1997; Sun et al., 2007). The sudden change in subduction direction led to the remarkable extension of the lithosphere (Maruyama et al., 1997; Sun et al., 2007), especially the extension of the deep Tan-Lu fault in the study region (Zhang et al., 2003). The extension promoted the upwelling and partial melting of the asthenosphere (Wu et al., 2005), facilitating the emplacement of asthenospheric mantle-derived magmas. This geodynamic regime is thus different from those in magmatic arcs or collisional orogens.

7. Conclusions

The Wangjiazhuang Cu-Mo deposit occurred during lithospheric thinning/craton destruction within an intracontinental setting. It shows similarities to porphyry deposits in aspects of alteration types, ore-forming fluids and physico-chemical conditions, but is distinguished from typical porphyry deposits by the host rock, the mineralization style and the tectonic setting. Systematic studies on geochronology, geochemistry, fluid inclusions, stable and radioactive isotopes of the ore bodies as well as the host granitoid allow us to investigate the specific ore-forming processes and to reveal the essential factors controlling the formation of this unusual Cu-Mo deposit:

1. The Cu-Mo mineralization occurred at ca. 128.3 ± 0.7 Ma, nearly coincident with the emplacement of the host quartz monzonite (128.8 ± 1.0 Ma, 2σ).
2. The quartz monzonite shows adakitic and alkaline characteristics with high water and metal (Cu and Mo) contents and high oxidation state, giving rise to the oxidized ore-forming fluids during magma differentiation.
3. Hydrothermal alterations such as potassic, potassic-silicic, silicic and sericitic alterations were developed in the deposit, of which the potassic-silicic alteration is basically associated with the ore-forming fluids.
4. The precipitation of the ore-forming metals mainly occurred at the temperatures of 300–400 °C, and was initiated by the f_{O2} and pH change during cooling and water-rock interaction. Different mobilities between the vapor-carried Cu and the liquid-carried Mo contributed to the separation of the Cu-rich and Mo-rich orebodies at shallow crustal depth.
5. Both Cu and Mo were originally sourced from the asthenospheric mantle, consistent with the origin of the host granitoid which was mainly derived from asthenospheric mantle mixed by ~15–20% lower crust melts.
6. The asthenospheric mantle beneath the eastern NCC was oxidized

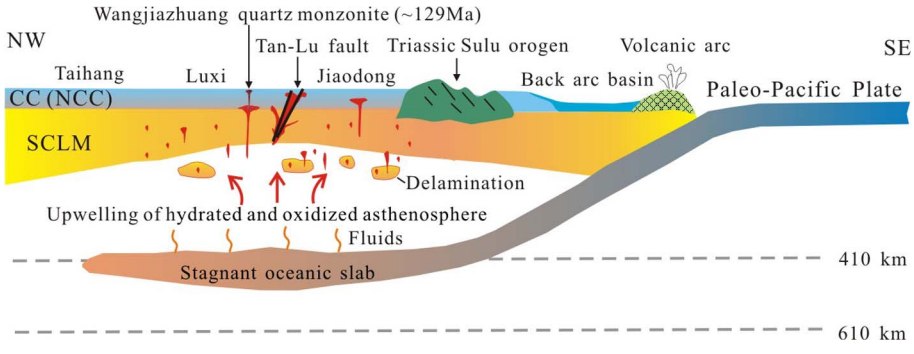

Fig. 19. Geodynamic model for the generation of the Wangjiazhuang deposit and the host granitoid (consulted from Pirajno and Zhou, 2015). Abbreviations: CC, continental crust; SCLM, subcontinental lithospheric mantle; NCC, North China Craton.

and hydrated by the water released from the stagnant Paleo-Pacific slab in the transitional zone (410–660 km) during the early Cretaceous. Such modification not only contributed to the remarkable thinning of the lithosphere beneath the eastern NCC, but also facilitated the asthenospheric mantle to become the favorable source for the generation of Cu-Mo deposits.

Acknowledgements

We are grateful to Chao-Feng Li for help during Sr-Nd isotopes analyses, to Zhi-hui Dai and Yue-Heng Yang for help during zircon U-Pb and Hf analyses, to Guo-Hao Jiang for help during He-Ar isotopes analyses, to Jin Gu for help during sulfur isotopic analyses, and to He Li and Wen-Jun Li for help during whole-rock major and trace elements analyses. Li Zhou is thanked for synthesizing fluid inclusion standards. Thomas Ulrich, Nuo Li and the anonymous reviewers are thanked for providing constructive comments on the earlier version of the paper. Kun Shen and Lei Shu from Shandong Geological Sciences Institute are also thanked for help during field investigations. This study is financially supported by the Ministry of Science and Technology of People's Republic of China (2016YFC0600105), the Natural Science Foundation of China (41472079) and the Youth Innovation Promotion Association, Chinese Academy of Sciences (Granted No. 2014358).

References

Allan, M.M., Yardley, B.W.D., Forbes, L.J., Shmulovich, K.I., Banks, D.A., Shepherd, T.J., 2005. Validation of LA-ICP-MS fluid inclusion analysis with synthetic fluid inclusions. Am. Miner. 90, 1767–1775.

Allégre, C.J., Staudacher, T., Sarda, P., 1986. Rare gas systemataics: formation of the atmosphere, evolution and structure of the earth's mantle. Earth Planet. Sci. Lett. 81, 127–150.

Angus, S., Armstrong, B., de Reuck, K.M., 1976. International Thermodynamic Tables of the Fluid State. Carbon Dioxide. Pergamon Press, New York, pp. 1–385.

Audétat, A., 2010. Source and evolution of molybdenum in the porphyry Mo(-Nb) deposit at Cave Peak, Texas. J. Petrol. 51, 1739–1760.

Baldwin, J.A., Brown, M., Schmitz, M.D., 2007. First application of titanium-in-zircon thermometry to ultrahigh-temperature metamorphism. Geology 35, 295–298.

Ballard, J.R., Palin, J.M., Campbell, I.H., 2002. Relative oxidation states of magmas inferred from Ce(IV)/Ce(III) in zircon: application to porphyry copper deposits of northern Chile. Contrib. Miner. Petrol. 144, 347–364.

Berry, A.J., Harris, A.C., Kamenetsky, V.S., Newville, M., Sutton, S.R., 2009. The speciation of copper in natural fluid inclusions at temperatures up to 700 °C. Chem. Geol. 259, 2–7.

Berzina, A.P., Berzina, A.N., Gimon, V.O., 2011. The Sora porphyry Cu-Mo deposit (Kuznetsk Alatau): magmatism and effect of mantle plume on the development of ore-magmatic system. Russ. Geol. Geophys. 52, 1553–1562.

Blevin, P.L., 2004. Redox and compositional parameters for interpreting the granitoid metallogeny of Eastern Australia: implications for gold-rich ore systems. Resource Geol. 54, 241–252.

Blichert-Toft, J., Albaréde, F., 1997. The Lu-Hf isotope geochemistry of chondrites and the evolution of the mantle-crust system. Earth Planet. Sci. Lett. 148, 243–258.

Bodnar, R.J., 1993. Revised equation and table for determining the freezing point depression of H_2O-NaCl solutions. Geochim. Cosmochim. Acta 57, 683–684.

Brown, P.E., Lamb, W.M., 1989. P-V-T properties of fluids in the system $H_2O \pm CO_2 \pm$ NaCl: new graphical presentations and implications for fluid inclusion studies. Geochim. Cosmochim. Acta 53, 1209–1221.

Candela, P.A., Holland, H.D., 1984. The partitioning of copper and molybdenum between silicate melts and aqueous fluids. Geochim. Cosmochim. Acta 48, 373–380.

Cao, X., 1989. Solubility of molybdenite and the transport of molybdenum in hydrothermal solutions (PhD thesis). Iowa State University, Iowa, pp. 1–103.

Cao, M., Qin, K., Li, G., Jin, L., Evans, N.J., Yang, X., 2014. Baogutu: an example of reduced porphyry Cu deposit in western Junggar. Ore Geol. Rev. 56, 159–180.

Carroll, M.R., Rutherford, M.J., 1988. Sulfur speciation in hydrous experimental glasses of varying oxidation state: results from measured wavelength shifts of sulfur X-rays. Am. Miner. 73, 845–849.

Castillo, P.R., 2012. Adakite petrogenesis. Lithos 134-135, 304–316.

Chen, B., Jahn, B.M., Suzuki, K., 2013. Petrological and Nd-Sr-Os isotopic constraints on the origin of high-Mg adakitic rocks from the North China Craton: tectonic implications. Geology 41, 91–94.

Chen, L., Tao, W., Zhao, L., Zhen, T.Y., 2008. Distinct lateral variation of lithospheric thickness in the Northeastern North China Craton. Earth Planet. Sci. Lett. 267, 56–68.

Chen, L., Zheng, T., Xu, W., 2006. A thinned lithospheric image of the Tanlu Fault Zone, eastern China: constructed from wave equation based receiver function migration. J. Geophys. Res. 111, B09312.

Chen, Y.J., Zhang, C., Wang, P., Pirajno, F., Li, N., 2017. The Mo deposits of Northeast China: a powerful indicator of tectonic settings and associated evolutionary trends. Ore Geol. Rev. 81, 602–640.

Chiaradia, M., 2014. Copper enrichment in arc magmas controlled by overriding plate thickness. Nat. Geosci. 7, 43–46.

Collins, P.L.F., 1979. Gas hydrates in CO_2-bearing fluid inclusions and the use of freezing data for estimation of salinity. Econ. Geol. 74, 1435–1444.

Condie, K.C., 2005. TTGs and adakites: are they both slab melts? Lithos 80, 33–44.

Cooke, D.R., Hollings, P., Walshe, J.L., 2005. Giant porphyry deposits: characteristics, distribution, and tectonic controls. Econ. Geol. 100, 801–818.

De la Roche, H., Leterrier, J., Granclaude, P., Marchal, M., 1980. A classification of volcanic and plutonic rocks using R1-R2 diagram and major-element analyses-its relationships with current nomenclature. Chem. Geol. 29, 183–210.

Defant, M.J., Drummond, M.S., 1990. Derivation of some modern arc magmas by melting of young subducted lithosphere. Nature 347, 662–665.

Defant, M.J., Kepezhinskas, P., 2001. Evidence suggests slab melting in arc magmas. EOS Trans. Am. Geophys. Union 82, 62–70.

Ding, Z.J., Sun, F.Y., Liu, J.H., Liu, D.H., Li, B.L., Zhang, P.J., Qian, Y., Li, J., 2012. Re-Os dating of molybdenites from the Xingjiashan molybdenum-tungsten deposit in Jiaodong Peninsula, China and its geological significance. Acta Petrologica Sinica 28, 2721–2732 (in Chinese with English abstract).

Dong, G., Santosh, M., Li, S., Shen, J., Mo, X., Scott, S., Qu, K., Wang, X., 2013. Mesozoic magmatism and metallogenesis associated with the destruction of the North China Craton: evidence from U-Pb geochronology and stable isotope geochemistry of the Mujicun porphyry Cu-Mo deposit. Ore Geol. Rev. 53, 434–445.

Driesner, T., Heinrich, C.A., 2007. The system H_0O-NaCl Part I: correlation formulae for phase relations in temperature-pressure-composition space from 0 to 1000 °C, 0 to 5000 bar, and 0 to 1 XNaCl. Geochim. Cosmochim. Acta 71, 4880–4901.

Du, A., Wu, S., Sun, D., Wang, S., Qu, W., Markey, R., Stain, H., Morgan, J., Malinovskiy, D., 2004. Preparation and certification of Re-Os dating reference materials: molybdenites HLP and JDC. Geostand. Geoanal. Res. 28, 41–52.

Einaudi, M.T., Hedenquist, J.W., Inan, E.E., 2003. Sulfidation state of fluids in active and extinct hydrothermal systems: transitions from porphyry to epithermal environments. Soc. Econ. Geologists Special Publ. 10, 285–313.

Etschmann, B.E., Liu, W., Testemale, D., Müller, H., Rae, N.A., Proux, O., Hazemann, J.L., Brugger, J., 2010. An in situ XAS study of copper (I) transport as hydrosulfide complexes in hydrothermal solutions (25–592 °C, 180–600 bar): speciation and solubility in vapor and liquid phases. Geochim. Cosmochim. Acta 74, 4723–4739.

Fan, W.M., Zhang, H.F., Baker, J., Jarvis, K.E., Mason, P.R.D., Menzies, M.A., 2000. On and off the North China Craton: where is the Archaean keel? J. Petrol. 41, 933–950.

Farges, F., Siewert, R., Brown, J.R., et al., 2006. Structural environments around molybdenum in silicate glasses and melts. I. Influence of composition and oxygen fugacity on the local structure of molybdenum. Can. Mineral. 44, 731–753.

Farmer, G.L., DePaolo, D.J., 1984. Origin of Mesozoic and Tertiary granite in the western United States and implications for pre-Mesozoic crustal structure 2. Nd and Sr isotopic studies of unmineralized and Cu- and Mo-mineralized granite in the Precambrian craton. J. Geophys. Res. 89, 10141–10160.

Ferry, J.M., Watson, E.B., 2007. New thermodynamic models and revised calibrations for the Ti-in-zircon and Zr-in-rutile thermometers. Contrib. Miner. Petrol. 154, 429–437.

Foley, S., Tiepolo, M., Vannucci, R., 2002. Growth of early continental crust controlled by melting of amphibolite in subduction zones. Nature 417, 837–840.

Frost, B.R., Barnes, C.G., Collins, W.J., Arculus, R.J., Ellis, D.J., Frost, C.D., 2001. A geochemical classification for granitic rocks. J. Petrol. 42, 2033–2048.

Frost, B.R., Shive, P.N., 1986. Magnetic mineralogy of the lower continental crust. J. Geophys. Res. 91, 6513–6521.

Frost, D.J., McCammon, A., 2008. The redox state of earth's mantle. Annu. Rev. Earth Planet. Sci. 36, 389–420.

Fu, B., Page, F.Z., Cavosie, A.J., Clechenko, C.C., Fournelle, J., Kita, N.T., Lackey, J.S., Wilde, S.A., Valley, J.W., 2008. Ti-in-zircon thermometry: applications and limitations. Contrib. Miner. Petrol. 156, 197–215.

Fukao, Y., Obayashi, M., Inoue, H., Nenbai, M., 1992. Subducting slabs stagnant in the mantle transition zone. J. Geophys. Res. 97, 4809–4822.

Gao, L., Chen, B., 2013. Study on petrology, geochemistry and Os-Nd-Sr isotopes of Jinan gabbro in Luxi Block. J. Earth Sci. Environ. 35, 19–31 (in Chinese with English abstract).

Gao, S., Luo, T.C., Zhang, B.R., Zhang, H.F., Han, Y.W., Zhao, Z.D., Hu, Y.K., 1998. Chemical composition of the continental crust as revealed by studies in East China. Geochim. Cosmochim. Acta 62, 1959–1975.

Gao, S., Zhang, J.F., Xu, W.L., Liu, Y.S., 2009. Delamination and destruction of the North China Craton. Chin. Sci. Bull. 54, 3367–3378.

Gao, Y.F., Santosh, M., Wei, R.H., Ma, G.X., Chen, Z.K., Wu, J.L., 2013. Origin of high Sr/Y magmas from the northern Taihang Mountains: implications for Mesozoic porphyry copper mineralization in the North China Craton. J. Asian Earth Sci. 78, 143–159.

Gerlach, T.E., 1993. Oxygen buffering of Kilauea volcanic gases and the oxygen fugacity of Kilauea basalt. Geochim. Cosmochim. Acta 57, 795–814.

Gill, J.B., 1981. Orogenic Andesites and Plate Tectonics. Springer-Verlag, Berlin Heidelberg, New York, pp. 1–390.

Grant, J.A., 1986. The isocon diagram-a simple solution to Gresens' equation for metasomatic alteration. Econ. Geol. 81, 1976–1982.

Griffin, W.L., Pearson, N.J., Belousova, E., Jackson, S.E., Achterbergh, E.V., O'Reilly, S.Y., Shee, S.R., 2000. The Hf isotope composition of cratonic mantle: LAM-MC-ICPMS analysis of zircon megacrysts in kimberlites. Geochim. Cosmochim. Acta 64, 133–147.

Griffin, W.L., Wang, X., Jackson, S.E., Pearson, N.J., O'Reilly, S.Y., Xu, X.S., Zhou, X.M., 2002. Zircon chemistry and magma mixing, SE China: in-situ analysis of Hf isotopes, Tonglu and Pingtan igneous complexes. Lithos 61, 237–269.

Griffin, W.L., Zhang, A.D., O'Reilly, S.Y., Ryan, C.G., 1998. Phanerozoic evolution of the lithosphere beneath the Sino-Korean Craton. Am. Geophys. Union-Geodyn. Series 27, 107–126.

Guillong, M., Meier, D.L., Allan, M.M., Heinrich, C.A., Yardley, B.W.D., 2008. SILLS: A MATLAB-based program for the reduction of laser ablation ICP-MS data of homogeneous materials and inclusions. In: Sylvester, P. (Ed.), Laser Ablation ICP-MS in the Earth Sciences: Current Practices and Outstanding Issues. Mineralogical Association of Canada Short Course Series 40, 328–333.

Guo, F., Fan, W., Wang, Y., Lin, G., 2003. Geochemistry of late Mesozoic mafic magmatism in west Shandong Province, eastern China: characterizing the lost lithospheric mantle beneath the North China Block. Geochem. J. 37, 63–77.

Guo, F., Fan, W.M., Wang, Y.J., Lin, G., 2001. Late Mesozoic mafic intrusive complexes in North China Block: constraints on the nature of subcontinental lithospheric mantle. Phys. Chem. Earth (Part A: Solid Earth and Geodesy) 26, 759–771.

Haggerty, S.E., Toft, P.B., 1985. Native iron in the continental lower crust: petrological and geophysical implications. Science 229, 647–649.

Hanchar, J.M., Watson, E.B., 2003. Zircon saturation thermometry. Rev. Mineral. Geochem. 53, 89–112.

Hayden, L.A., Watson, E.B., 2007. Rutile saturation in hydrous siliceous melts and its bearing on Ti-thermometry of quartz and zircon. Earth Planet. Sci. Lett. 258, 561–568.

Haynes, D.W., Cross, K.C., Bills, R.T., Reed, M.H., 1994. Olympic Dam ore genesis: a fluid mixing model. Econ. Geol. 90, 281–307.

Heinrich, C.A., Günther, D., Audétat, A., Ulrich, T., Frischknecht, R., 1999. Metal fractionation between magmatic brine and vapor, determined by microanalysis of fluid inclusions. Geology 27, 755–758.

Heinrich, C.A., Pettke, T., Halter, W.E., Aigner-Torres, M., Audetat, A., Gunther, D., Hanttendorf, B., Bleiner, D., Guillong, M., Horn, I., 2003. Quantitative multi-element analysis of minerals, fluid, and melt inclusions by laser ablation-inductively coupled plasma-mass spectrometry. Geochim. Cosmochim. Acta 67, 3473–3496.

Hezarkhani, A., Williams-Jones, A.E., Gammons, C.H., 1999. Factors controlling copper solubility and chalcopyrite deposition in the Sungun porphyry copper deposit, Iran. Mineralium Deposita 34, 770–783.

Hiess, J., Nutman, A.P., Bennett, V.C., Holden, P., 2008. Ti-in-zircon thermometry applied to contrasting Archean metamorphic and igneous systems. Chem. Geol. 247, 323–338.

Hofmann, A.W., 1988. Chemical differentiation of the Earth: the relationship between mantle, continental crust, and oceanic crust. Earth Planet. Sci. Lett. 90, 297–314.

Holzheid, A., Borisov, A., Palme, H., 1994. The effect of oxygen fugacity and temperature on solubilities of nickel, cobalt, and molybdenum in silicate melts. Geochim. Cosmochim. Acta 58, 1975–1981.

Hou, Z., Yang, Z., Lu, Y., Kemp, A., Zheng, Y., Li, Q., Tang, J., Yang, Z., Duan, L., 2015. A genetic linkage between subduction- and collision-related porphyry Cu deposits in continental collision zones. Geology 43, 247–250.

Hou, Z., Zhang, H., 2015. Geodynamics and metallogeny of the eastern Tethyan metallogenic domain. Ore Geol. Rev. 70, 346–384.

Hu, R.Z., Bi, X.W., Jiang, G.H., Chen, H.W., Peng, J.T., Qi, Y.Q., Wu, L.Y., Wei, W.F., 2012. Mantle-derived noble gases in ore-forming fluids of the granite-related Yaogangxian tungsten deposit, Southeastern China. Miner. Deposita 47, 623–632.

Huang, J., Zhao, D., 2006. High-resolution mantle tomography of China and surrounding regions. J. Geophys. Res. 111, B09305.

Huang, R., Audétat, A., 2012. The titanium-in-quartz (TitaniQ) thermobarometer: a critical examination and re-calibration. Geochim. Cosmochim. Acta 84, 75–89.

Hurtig, N.C., Williams-Jones, A.E., 2014. An experimental study of the solubility of MoO_3 in aqueous vapour and low to intermediate density supercritical fluids. Geochim. Cosmochim. Acta 136, 169–193.

Ichiki, M., Baba, K., Obayashi, M., Utada, H., 2006. Water content and geotherm in the upper mantle above the stagnant slab: interpretation of electrical conductivity and seismic P-wave velocity models. Phys. Earth Planet. Inter. 155, 1–15.

Jahn, B.M., Auvray, B., Shen, Q.H., Liu, D.Y., Zhang, Z.Q., Dong, Y.J., Ye, X.J., Zhang, Q.Z., Cornichet, J., Mace, J., 1988. Archean crustal evolution in China: the Taishan complex, and evidence for juvenile crustal addition from long-term depleted mantle. Precambr. Res. 38, 381–403.

Jugo, P.J., 2009. Sulfur content at sulfide saturation in oxidized magmas. Geology 37, 415–418.

Jugo, P.J., Wilke, M., Botcharnikov, R.E., 2010. Sulfur K-edge XANES analysis of natural and synthetic basaltic glasses: implications for S speciation and S content as function of oxygen fugacity. Geochim. Cosmochim. Acta 74, 5926–5938.

Kelemen, P.B., Hanghøj, K., Greene, A.R., 2007. 318-One view of the geochemistry of subduction-related magmatic arcs, with an emphasis on primitive andesite and lower crust. Treatise Geochem. 3, 1–70.

Kelley, K.A., Cottrell, E., 2009. Water and the oxidation state of subduction zone magmas. Science 325, 605–607.

Kendrick, M.A., Burgess, R., Pattrick, R.A.D., Turner, G., 2001. Fluid inclusion noble gas and halogen evidence on the origin of Cu-porphyry mineralising fluids. Geochim. Cosmochim. Acta 65, 2651–2668.

Keppler, H., Wyllie, P., 1991. Partitioning of Cu, Sn, Mo, W, U, and Th between melt and aqueous fluid in the systems haplogranite-H_2O-HCl and haplogranite-H_2O-HF. Contrib. Miner. Petrol. 109, 139–150.

Kesler, S.E., Wilkinson, B.H., 2008. Earth's copper resources estimated from tectonic diffusion of porphyry copper deposits. Geology 36, 255–258.

Klemm, L.M., Pettke, T., Heinrich, C.A., 2007. Hydrothermal evolution of the El Teniente deposit, Chile: porphyry Cu-Mo ore deposit from low-salinity magmatic fluids. Econ. Geol. 102, 1021–1045.

Klemm, L.M., Pettke, T., Heinrich, C.A., 2008. Fluid and source magma evolution of the Questa porphyry Mo deposit, New Mexico, USA. Miner. Deposita 43, 533–552.

Komabayashi, T., Omori, S., Maruyama, S., 2004. Petrogenetic grid in the system MgO-SiO_2-H_2O up to 30 GPa, 1600 °C: applications to hydrous peridotite subducting into the Earth's deep interior. J. Geophys. Res. 109, B03206.

Komiya, T., Maruyama, S., 2007. A very hydrous mantle under the western Pacific region: implications for formation of marginal basins and style of Archean plate tectonics. Gondwana Res. 11, 132–147.

Kong, Q.Y., Zhang, T.Z., Yu, X.F., Xu, J.X., Pan, Y.L., Li, X.S., 2006. Deposits in Shandong Province. Shandong Science and Technology Press, Jinan, pp. 1–902 (in Chinese).

Lan, T.G., Fan, H., Hu, F.F., Yang, K.F., Wang, Y., 2011a. Genesis of the Weishan REE deposit, Shandong Province: evidences from Rb-Sr isochron age, LA-MC-ICPMS Nd isotopic compositions and fluid inclusions. Geochimica 40, 428–442 (in Chinese with English abstract).

Lan, T.G., Fan, H.R., Hu, F.F., Tomkins, A.G., Yang, K.F., Liu, Y.S., 2011b. Multiple crust-mantle interactions for destruction of the North China Craton: geochemical and Sr-Nd-Pb-Hf isotopic evidence from Longbaoshan alkaline complex. Lithos 122, 87–106.

Lan, T.G., Fan, H.R., Santosh, M., Hu, F.F., Yang, K.F., Yang, Y.H., Liu, Y.S., 2013. Crust-mantle interaction beneath the Luxi Block, eastern North China Craton: evidence from coexisting mantle- and crust-derived enclaves in a quartz monzonite pluton. Lithos 177, 1–16.

Landtwing, M.R., Pettke, T., Halter, W.E., Heinrich, C.A., Redmond, P.B., Einaudi, M.T., Kunze, K., 2005. Copper deposition during quartz dissolution by cooling magmatic-hydrothermal fluids: the Bingham porphyry. Earth Planet. Sci. Lett. 235, 229–243.

Langmuir, C.H., Vocke, R.D., Hanson, G.N., 1978. A general mixing equation with applications to Icelandic basalts. Earth Planet. Sci. Lett. 37, 380–392.

Lecumberri-Sanchez, P., Steele-MacInnis, M., Bodnar, R.J., 2012. A numerical model to estimate trapping conditions of fluid inclusions that homogenize by halite disappearance. Geochim. Cosmochim. Acta 92, 14–22.

Lecumberri-Sanchez, P., Steele-MacInnis, M., Weis, P., Driesner, T., Bodnar, R.J., 2015. Salt precipitation in magmatic-hydrothermal systems associated with upper crustal plutons. Geology 43, 1063–1066.

Lee, C.A., Luffi, P., Chin, E.J., Bouchet, R., Dasgupta, R., Morton, D.M., Roux, V.L., Yin, Q.Z., Jin, D., 2012. Copper systematics in arc magmas and implications for crust-mantle differentiation. Science 336, 64–68.

Li, B.F., Yuan, S.R., 1991. Geological characteristics of porphyry Cu-(Mo) deposits in Zouping area, Shandong Province. Geol. Prospect. 27, 7–12 (in Chinese).

Li, H.Y., Xu, Z.W., Lu, X.C., Chen, L.H., Liu, S.M., Yang, X.N., Zhang, J., Li, H.C., Chen, W., 2008. Evolution of Mesozoic volcanic rocks in the Zouping basin, western Shandong Province: constraints for mantle sources. Acta Petrologica Sinica 24, 2537–2547 (in Chinese with English abstract).

Li, J.W., Bi, S.Y., Selby, D., Chen, L., Vasconcelos, P., Thiede, D., Zhou, M.F., Zhao, X.F., Li, Z.K., Qiu, H.N., 2012. Giant Mesozoic gold provinces related to the destruction of the North China craton. Earth Planet. Sci. Lett. 349-350, 26–37.

Li, S.R., Santosh, M., 2014. Metallogeny and craton destruction: records from the North China Craton. Ore Geol. Rev. 56, 376–414.

Li, Z.X., Li, X.H., 2007. Formation of the 1300-km-wide intracontinental orogen and postorogenic magmatic province in Mesozoic South China: a flat-slab subduction model. Geology 35, 179–182.

Liu, P.R., Xiong, Y.X., Ma, X.D., Wang, K.F., Dong, Y.Y., Li, M., 2013a. SHRIMP zircon U-Pb and molybdenite Re-Os age of the copper polymetallic deposit in Zouping volcanic basin, Shandong Province. Geol. Bull. China 32, 1621–1630 (in Chinese with English abstract).

Liu, S., Hu, R.Z., Gao, S., Feng, C.X., Qi, L., Zhong, H., Xiao, T.F., Qi, Y.Q., Wang, T., Coulson, L.M., 2008a. Zircon U-Pb geochronology and major, trace elemental and Sr-Nd-Pb isotopic geochemistry of mafic dykes in western Shandong Province, East China: constrains on their petrogenesis and geodynamic significance. Chem. Geol. 255, 329–345.

Liu, S.M., Xu, Z.W., Lu, X.C., Li, H.Y., Wang, H., Yang, X.N., Zhao, Z.X., 2013b. Formation, evolution and mineralization of ore-forming fluid for copper deposit in Zouping volcanic area in Shandong. J. Geol. 37, 521–529 (in Chinese with English abstract).

Liu, Y.S., Gao, S., Yuan, H.L., Zhou, L., Liu, X.M., Wang, X.C., Hu, Z.C., Wang, L.S., 2004. U-Pb zircon ages and Nd, Sr and Pb isotopes of lower crustal xenoliths from North China Craton: insights on evolution of lower continental crust. Chem. Geol. 211, 87–109.

Liu, Y.S., Hu, Z.C., Gao, S., Günther, D., Xu, J., Gao, C.G., Chen, H.H., 2008b. In situ analysis of major and trace elements of anhydrous minerals by LA-ICP-MS without applying an internal standard. Chem. Geol. 257, 34–43.

Liu, Y.S., Hu, Z.C., Zong, K.Q., Gao, C.G., Gao, S., Xu, J., Chen, H.H., 2010. Reappraisement and refinement of zircon U-Pb isotope and trace element analyses by LA-ICP-MS. Chin. Sci. Bull. 55, 1535–1546.

Ludwig, K.R., 2003. User's Manual for Isoplot 300: a geochronolgical Toolkit for Microsoft Excel. Berkeley Geochronol. Center Spec. Publ. 4, 25–32.

Lugmair, G.W., Harti, K., 1978. Lunar initial $^{143}Nd/^{144}Nd$: differential evolution of the lunar crust and mantle. Earth Planet. Sci. Lett. 39, 349–357.

Mamyrin, B.A., Tolstikhin, I.N., 1984. Helium isotopes in nature. Dev. Geochem. 3, 1–273.

Mao, J., Pirajno, F., Cook, N., 2011. Mesozoic metallogeny in East China and corresponding geodynamic settings – an introduction to the special issue. Ore Geol. Rev. 43, 1–7.

Mao, J., Pirajno, F., Lehmann, B., Luo, M., Berzina, A., 2014. Distribution of porphyry deposits in the Eurasian continent and their corresponding tectonic settings. J. Asian Earth Sci. 79, 576–584.

Mao, J., Zhang, Z., Zhang, Z., Du, A., 1999. Re-Os isotopic dating of molybdenites in the Xiaoliugou W-(Mo) deposit in the northern Qulian Mountains and its geological significance. Geochim. Cosmochim. Acta 63, 1815–1818.

Martin, H., Smithies, R.H., Rapp, R., Moyen, J.F., Champion, D., 2005. An overview of adakite, tonalite-trondhjemite-granodiorite (TTG), and sanukitoid: relationships and some implications for crustal evolution. Lithos 79, 1–24.

Maruyama, S., Isozaki, Y., Kimura, G., Terabayashi, M., 1997. Paleogeographic maps of the Japanese Islands: plate tectonic synthesis from 750 Ma to the present. The Island

Arc 6, 121–142.
Maruyama, S., Okamoto, K., 2007. Water transportation from the subducting slab into the mantle transition zone. Gondwana Res. 11, 148–165.
Meng, Q.R., Zhang, G.W., 2000. Geologic framework and tectonic evolution of the Qinling orogen, central China. Tectonophysics 323, 183–196.
Menzies, M.A., Fan, W., Zhang, M., 1993. Palaeozoic and Cenozoic lithoprobes and the loss of > 120 km of Archaean lithosphere, Sino-Korean craton, China. Geol. Soc., Lond., Spec. Publ. 76, 71–78.
Miller, C.F., Mcdowell, S.M., Mapes, R.W., 2003. Hot and cold granites? Implications of zircon saturation temperatures and preservation of inheritance. Geology 31, 529–532.
Moore, J.G., Fabbi, B.P., 1971. An estimate of the juvenile sulfur content of basalt. Contrib. Miner. Petrol. 33, 118–127.
Mungall, J.E., 2002. Roasting the mantle: slab melting and the genesis of major Au and Au-rich Cu deposits. Geology 30, 915–918.
Ohmoto, H., 1972. Systematics of sulfur and carbon isotopes in hydrothermal ore deposits. Econ. Geol. 67, 551–578.
Ohmoto, H., Lasaga, A.C., 1982. Kinetics of reactions between aqueous sulfates and sulfides in hydrothermal systems. Geochim. Cosmochim. Acta 46, 1727–1745.
Ohmoto, H., Rye, R.O., 1979. Isotopes of sulfur and carbon. In: Barnes, H.L. (Ed.), Geochemistry of Hydrothermal Ore Deposits. John Wiley & Sons, New York, pp. 509–567.
Oppenheimer, C., Scaillet, B., Martin, R.S., 2011. Sulfur degassing from volcanoes: source conditions, surveillance, plume chemistry and earth system impacts. Rev. Mineral. Geochem. 73, 363–421.
Ouyang, H.G., Mao, J.W., Santosh, M., Zhou, J., Zhou, Z.H., Wu, Y., Hou, L., 2013. Geodynamic setting of Mesozoic magmatism in NE China and surrounding regions: perspectives from spatio-temporal distribution patterns of ore deposits. J. Asian Earth Sci. 78, 222–236.
Pettke, T., Oberli, F., Heinrich, CA., 2010. The magma and metal source of giant porphyry-type ore deposits, based on lead isotope microanalysis of individual fluid inclusions. Earth Planet. Sci. Lett. 296, 267–277.
Pirajno, F., Zhou, T., 2015. Intracontinental porphyry and Porphyry-Skarn mineral systems in Eastern China: scrutiny of a special case “Made-in-China”. Econ. Geol. 110, 603–629.
Pokrovski, G.S., Borisova, A.Y., Harrichoury, J.C., 2008. The effect of sulfur on vapor-liquid fractionation of metals in hydrothermal systems. Earth Planet. Sci. Lett. 266, 345–362.
Qin, J., Din, J., Zhang, D., Rusk, B., Liu, C., Zhang, Q., 2012. Tectonic settings of porphyry Cu-Mo-Au deposits in the Himalayan-Tibetan orogen, East Tethys. Int. Geol. Rev. 54, 302–312.
Qiu, J., Lo, C.H., McInnes, B.I.A., Zhou, J., 2000. Potash-rich magmatism and associated Gold-Copper mineralization in the Yishu deep fault zone and its vicinity, eastern China. Resour. Geol. 50, 269–280.
Redmond, P.B., Einaudi, M.T., Inan, E.E., Landtwing, M., Heinrich, C.A., 2004. Copper deposition by fluid cooling in intrusion-centered systems: new insights from Bingham porphyry ore deposit, Utah. Geology 32, 217–220.
Reed, M.H., Palandri, J., 2006. Sulfide mineral precipitation from hydrothermal fluids. Rev. Mineral. Geochem. 61, 609–631.
Ren, J., Tamaki, K., Li, S., Zhang, J., 2002. Late Mesozoic and Cenozoic rifting and its dynamic setting in eastern China and adjacent areas. Tectonophysics 344, 175–205.
Richards, J.P., 2003. Tectono-magmatic precursors for porphyry Cu-(Mo-Au) deposit formation. Econ. Geol. 98, 1515–1533.
Richards, J.P., 2009. Postsubduction porphyry Cu-Au and epithermal Au deposits: products of remelting of subduction-modified lithosphere. Geology 37, 247–250.
Richards, J.P., 2011a. Magmatic to hydrothermal metal fluxes in convergent and collided margins. Ore Geol. Rev. 40, 1–26.
Richards, J.P., 2011b. High Sr/Y arc magmas and porphyry Cu ± Mo ± Au deposits: just add water. Econ. Geol. 106, 1075–1081.
Richards, JP, 2014. Discussion of Sun et al. (2013): The link between reduced porphyry copper deposits and oxidized magmas. Geochim. Cosmochim. Acta 126, 643–645.
Richards, J.P., 2015a. Tectonic, magmatic, and metallogenic evolution of the Tethyan orogen: from subduction to collision. Ore Geol. Rev. 70, 323–345.
Richards, J.P., 2015b. The oxidation state, and sulfur and Cu contents of arc magmas: implications for metallogeny. Lithos 233, 27–45.
Richards, J.P., Kerrich, R., 2007. Special Paper: adakite-like rocks: their diverse origins and questionable role in metallogenesis. Econ. Geol. 102, 537–576.
Richards, J.P., Spell, T., Rameh, E., Razique, A., Fletcher, T., 2012. High Sr/Y magmas reflect arc maturity, high magmatic water content, and porphyry Cu ± Mo ± Au potential: examples from the Tethyan Arcs of Central and Eastern Iran and Western Pakistan. Econ. Geol. 107, 295–332.
Ridolfi, F., Renzulli, A., Puerini, M., 2010. Stability and chemical equilibrium of amphibole in calc-alkaline magmas: an overview, new thermo-barometric formulations and application to subduction-related volcanoes. Contrib. Miner. Petrol. 160, 45–66.
Roedder, E., 1992. Fluid inclusion evidence for immiscibility in magmatic differentiation. Geochim. Cosmochim. Acta 56, 5–20.
Rosso, K.M., Bodnar, R.J., 1995. Microthermometric and Raman spectroscopic detection limits of CO_2 in fluid inclusions and the Raman spectroscopic characterization of CO_2. Geochim. Cosmochim. Acta 59, 3961–3975.
Rowe, M.C., Kent, A.J.R., Nielsen, R.L., 2009. Subduction influence on oxygen fugacity and trace and volatile elements in basalts across the Cascade Volcanic Arc. J. Petrol. 50, 61–91.
Rudnick, R.L., Fountain, D.M., 1995. Nature and composition of the continental crust: a lower crustal perspective. Rev. Geophys. 33, 267–309.
Rusk, B.G., Lowers, H.A., Reed, M.H., 2008. Trace elements in hydrothermal quartz: relationships to cathodoluminescent textures and insights into vein formation. Geology 36, 547–550.
Rye, R.O., 1993. The evolution of magmatic fluids in the epithermal environment: the stable isotope perspective. Econ. Geol. 88, 733–752.
Rye, R.O., Bethke, P.M., Wasserman, W.D., 1992. The stable isotope geochemistry of acid sulfate alteration. Econ. Geol. 87, 225–262.
Seedorff, E., Dilles, J.H., Proffett, Jr., J.M., Einaudi, M.T., Zurcher, L., Stavast, W.J.A., Johnson, D.A., Barton, M.D., 2005. Porphyry deposits: characteristics and origin of hypogene features. Economic Geology 100th Anniversary Volume, pp. 251–298.
Seo, J.H., Guillong, M., Heinrich, C.A., 2012. Separation of molybdenum and copper in porphyry deposits: the roles of sulfur, redox, and pH in ore mineral deposition at Bingham Canyon. Econ. Geol. 107, 333–356.
Shinohara, H., 1994. Exsolution of immiscible vapor and liquid phases from a crystallizing silicate melt: implications for chlorine and metal transport. Geochim. Cosmochim. Acta 58, 5215–5221.
Sillitoe, R.H., 2010. Porphyry copper systems. Econ. Geol. 105, 3–41.
Smoliar, M.I., Walker, R.J., Morgan, J.W., 1996. Re-Os ages of group IIA, IIIA, IVA and VIB iron meteorites. Science 271, 1099–1102.
Söderlund, U., Patchett, P.J., Vervoort, J.D., Isachsen, C.E., 2004. The ^{176}Lu decay constant determined by Lu-Hf and U-Pb isotope systematics of Precambrian mafic intrusions. Earth Planet. Sci. Lett. 219, 311–324.
Steele-MacInnis, M., Lecumberri-Sanchez, P., Bodnar, R.J., 2012. HokieFlincs_H2O-NaCl: a Microsoft Excel spreadsheet for interpreting microthermometric data from fluid inclusions based on the PVTX properties of H_2O-NaCl. Comput. Geosci. 49, 334–337.
Stein, H.J., Markey, R.J., Morgan, J.W., Du, A.D., Sun, Y., 1997. High precise and accurate Re-Os ages for molybdenite from the east Oinling molybdenum belt, Shanxi province, China. Econ. Geol. 92, 827–835.
Stein, H.J., Markey, R.J., Morgan, J.W., Hannah, J.L., Schersten, A., 2001. The remarkable Re-Os chronometer in molybdenite: how and why it works. Terra Nova 13, 479–486.
Stuart, F.M., Burnard, P.G., Taylor, R.P., Turner, G., 1995. Resolving mantle and crustal contributions to ancient hydrothermal fluids: He-Ar isotopes in fluid inclusions from Dae Hwa W-Mo mineralisation, South Korea. Geochim. Cosmochim. Acta 59, 4663–4673.
Sun, S.S., McDonough, W.F., 1989. Chemical and isotopic systematics of oceanic basalts: implications for mantle composition and processes. Geol. Soc., Lond., Spec. Publ. 42, 313–345.
Sun, W., Audétat, A., Dolejš, D., 2014. Solubility of molybdenite in hydrous granitic melts at 800 °C, 100–200 MPa. Geochim. Cosmochim. Acta 131, 393–401.
Sun, W.D., Ding, X., Hu, Y.H., Li, X.H., 2007. The golden transformation of the Cretaceous plate subduction in the west Pacific. Earth Planet. Sci. Lett. 262, 533–542.
Sun, W.D., Liang, H.Y., Ling, M.X., Zhan, M.Z., Ding, X., Zhang, H., Yang, X.Y., Li, Y.L., Ireland, T.R., Wei, Q.R., Fan, W.M., 2013. The link between reduced porphyry copper deposits and oxidized magmas. Geochim. Cosmochim. Acta 103, 263–275.
SXLLAF (Shandong Xinguangxin Limited Liability Accounting Firm), 2010. Mining rights assessment report of Zouping copper deposit, Shandong Province. Jinan, pp. 1–30 (in Chinese).
Takagi, T., Tsukimura, K., 1997. Genesis of oxidized- and reduced-type granites. Econ. Geol. 92, 81–86.
Tang, L.C., 1990. Geological characteristics of the pegmatitic Cu-Au deposit in the Zouping volcanic basin, Shandong Province. Geol. Rev. 36, 85–87 (in Chinese).
Tapster, S., Condon, D.J., Naden, J., Noble, S.R., Petterson, M.G., Roberts, N.M.W., Saunders, A.D., Smith, D.J., 2016. Rapid thermal rejuvenation of high-crystallinity magma linked to porphyry copper deposit formation; evidence from the Koloula Porphyry Prospect, Solomon Islands. Earth Planet. Sci. Lett. 442, 206–217.
Thomas, J.B., Watson, E.B., Spear, F.S., Shemella, P.T., Nayak, S.K., Lanzirotti, A., 2010. TitaniQ under pressure: the effect of pressure and temperature on the solubility of Ti in quartz. Contrib. Miner. Petrol. 160, 743–759.
Trail, D., Watson, E.B., Tailby, N.D., 2011. The oxidation state of Hadean magmas and implications for early Earth’s atmosphere. Nature 480, 79–82.
Trail, D., Watson, E.B., Tailby, N.D., 2012. Ce and Eu anomalies in zircon as proxies for oxidation state of magmas. Geochim. Cosmochim. Acta 97, 70–87.
Ulrich, T., Heinrich, C.A., 2001. Geology and alteration geochemistry of the porphyry Cu-Au deposit at Bajo de la Alumbrera, Argentina. Econ. Geol. 96, 1719–1742.
Ulrich, T., Mavrogenes, J., 2008. An experimental study of the solubility of molybdenum in H_2O and KCl-H_2O solutions from 500° to 800°C, and 150 to 300 MPa. Geochim. Cosmochim. Acta 72, 2316–2330.
Vavra, G., Gebauer, D., Schmid, R., Compston, W., 1996. Multiple zircon growth and recrystallization during polyphase Late Carboniferous to Triassic metamorphism in granulites of the Ivrea Zone (Southern Alps): an ion microprobe (SHRIMP) study. Contrib. Miner. Petrol. 122, 337–358.
Wang, H., Fu, B., Xu, Z., Lu, X., Lu, J., Li, H., Qu, W., Yang, X., Chen, W., Zhang, J., 2015. Geology, geochemistry, and geochronology of the Wangjiazhuang porphyry-breccia Cu (-Mo) deposit in the Zouping volcanic basin, eastern North China Block. Ore Geol. Rev. 67, 336–353.
Wang, Q., Wyman, D.A., Xu, J.F., Zhao, Z.H., Jian, P., Xiong, X.L., Bao, Z.W., Li, C.F., Bai, Z.H., 2006. Petrogenesis of Cretaceous adakitic and shoshonitic igneous rocks in the Luzong area, Anhui Province (eastern China): implications for geodynamics and Cu-Au mineralization. Lithos 89, 424–446.
Wang, Q., Wyman, D.A., Xu, J.F., Zhao, Z.H., Jian, P., Zi, F., 2007. Partial melting of thickened or delaminated lower crust in the middle of eastern China: implications for Cu-Au mineralization. J. Geol. 115, 149–161.
Wark, D.A., Watson, E.B., 2006. TitaniQ: a titanium-in-quartz geothermometer. Contrib. Miner. Petrol. 152, 743–754.
Watson, E.B., Harrison, T.M., 2005. Zircon thermometer reveals minimum melting conditions on earliest earth. Sciences 308, 841–844.
Watson, E.B., Harrison, T.M., 1983. Zircon saturation revisited: temperature and

composition effects in a variety of crustal magma types. Earth Planet. Sci. Lett. 64, 295–304.
Watson, E.B., Wark, D.A., Thomas, J.B., 2006. Crystallization thermometers for zircon and rutile. Contrib. Miner. Petrol. 151, 413–433.
Webster, J.D., 1997. Exsolution of magmatic volatile phases from Cl-enriched mineralizing granitic magmas and implications for ore metal transport. Geochim. Cosmochim. Acta 61, 1017–1029.
Westra, G., Keith, S.B., 1981. Classification and genesis of stockwork molybdenum deposits. Econ. Geol. 76, 844–873.
Wilkinson, J.J., 2013. Triggers for the formation of porphyry ore deposits in magmatic arcs. Nat. Geosci. 6, 917–925.
Williams-Jones, A.E., Heinrich, C.A., 2005. Vapor transport of metals and the formation of magmatic-hydrothermal ore deposits. Economic Geology 100th Anniversary Special Paper 100, 1287–1312.
Wilson, A.J., Cooke, D.R., Harper, B.J., Deyell, C.L., 2007. Sulfur isotopic zonation in the Cadia district, southeastern Australia: exploration significance and implications for the genesis of alkalic porphyry gold-copper deposits. Miner. Deposita 42, 465–487.
Windley, B.F., Maruyama, S., Xiao, W.J., 2010. Delamination/thinning of sub-continental lithospheric mantle under Eastern China: the role of water and multiple subduction. Am. J. Sci. 310, 1250–1293.
Wones, D.R., 1981. Mafic silicates as indicators of intensive variables in granitic magmas. Min. Geol. 31, 191–212.
Wood, B.J., Bryndzia, L.T., Johnson, K.E., 1990. Mantle oxidation state and its relationship to tectonic environment and fluid speciation. Science 248, 337–345.
Woodhead, J., Hergt, J., 2005. A preliminary appraisal of seven natural zircon reference materials for in situ Hf isotope determination. Geostand. Geoanal. Res. 29, 183–195.
Wright, J.B., 1969. A simple alkalinity ratio and its application to questions of non-orogenic granite genesis. Geol. Mag. 106, 370–384.
Wu, F.Y., Lin, J.Q., Wilde, S.A., Zhang, X.O., Yang, J.H., 2005. Nature and significance of the Early Cretaceous giant igneous event in eastern China. Earth Planet. Sci. Lett. 233, 103–119.
Wu, F.Y., Yang, Y.H., Xie, L.W., Yang, J.H., Xu, P., 2006. Hf isotopic compositions of the standard zircons and baddeleyites used in U-Pb geochronology. Chem. Geol. 234, 105–126.
Wu, Y., Zheng, Y., 2004. Genesis of zircon and its constraints on interpretation of U-Pb age. Chin. Sci. Bull. 49, 1554–1569.
Xia, Q.K., Hao, Y., Li, P., Deloule, E., Coltorti, M., Dallai, L., Yang, X., Feng, M., 2010. Low water content of the Cenozoic lithospheric mantle beneath the eastern part of the North China Craton. J. Geophys. Res. 115, B07207.
Xia, Q.K., Liu, J., Liu, S.C., Kovácsb, I., Feng, M., Dang, L., 2013. High water content in the Mesozoic lithospheric mantle of the North China Craton and implications for its destruction. Earth Planet. Sci. Lett. 361, 85–97.
Xiao, W., Windley, B.F., Hao, J., Zhai, M., 2003. Accretion leading to collision and the Permian Solonker suture, Inner Mongolia, China: Termination of the Central Asian Orogenic belt. Tectonics 22, 8-1-8-20.
Xiao, Y., Zhang, H.F., Fan, W.M., Ying, J.F., Zhang, J., Zhao, X.M., Su, B.X., 2010. Evolution of lithospheric mantle beneath the Tan-Lu fault zone, eastern North China Craton: evidence from petrology and geochemistry of peridotite xenoliths. Lithos 117, 229–246.
Xie, G., Mao, J., Li, W., Zhu, Q., Liu, H., Jia, G., Li, Y., Zhang, J., 2016. Different proportion of mantle-derived noble gases in the Cu-Fe and Fe skarn deposits: He-Ar isotopic constraint in the Edong district, Eastern China. Ore Geol. Rev. 72, 343–354.
Xie, L.W., Zhang, Y.B., Sun, J.F., Wu, F.Y., 2008. In situ simultaneous determination of trace elements, U-Pb and Lu-Hf isotopes in zircon and baddeleyite. Chin. Sci. Bull. 53, 1565–1573.
Xu, W.L., Hergt, J.M., Gao, S., Pei, F.P., Wang, W., Yang, D.B., 2008. Interaction of adakitic melt-peridotite: implications for the high-Mg# signature of Mesozoic adakitic rocks in the eastern North China Craton. Earth Planet. Sci. Lett. 265, 123–137.
Xu, W.L., Zhou, Q.J., Pei, F.P., Yang, D.B., Gao, S., Li, Q.L., Yang, Y.H., 2013. Destruction of the North China Craton: Delamination or thermal/chemical erosion? Mineral chemistry and oxygen isotope insights from websterite xenoliths. Gondwana Res. 23, 119–129.
Xu, W.W., Zheng, T.Y., Zhao, L., 2011. Mantle dynamics of the reactivating North China Craton: constraints from the topographies of the 410-km and 660-km discontinuities. Sci. China Earth Sci. 54, 881–887.
Xu, Y.G., 2014. Recycled oceanic crust in the source of 90-40 Ma basalts in North and Northeast China: evidence, provenance and significance. Geochim. Cosmochim. Acta 143, 49–67.
Xu, Y.G., Li, H.Y., Pang, C.J., He, B., 2009. On the timing and duration of the destruction of the North China Craton. Chin. Sci. Bull. 54, 3379–3396.
Xu, Y.G., Ma, J.L., Huang, X.L., Iizuka, Y., Chung, S.L., Wang, Y.B., Wu, X.Y., 2004. Early Cretaceous gabbroic complex from Yinan, Shandong Province: petrogenesis and mantle domains beneath the North China Craton. Int. J. Earth Sci. 93, 1025–1041.
Xu, X.W., Mao, Q., Li, X.H., Pirajno, F.M., Qu, X., Deng, G., Chen, D.Z., Zhang, B.L., Dong, L.H., 2014. Copper-zinc albite porphyry in the Hersai porphyry copper deposit, East Junggar, China: a transition between late magmatic and hydrothermal porphyry copper deposit. Ore Geol. Rev. 61, 141–156.
Yan, J., Chen, J.F., Xie, Z., Gao, T.S., Foland, K.A., Zhang, X.D., Liu, M.W., 2005. Studies on petrology and geochemistry of the late Cretaceous basalts and mantle-derived xenoliths from eastern Shandong. Acta Petrologica Sinica 21, 99–112 (in Chinese with English abstract).
Yang, D.B., Xu, W.L., Pei, F.P., Yang, C.H., Wang, Q.H., 2012. Spatial extent of the influence of the deeply subducted South China Block on the southeastern North China Block: constraints from Sr-Nd-Pb isotopes in Mesozoic mafic igneous rocks. Lithos 136-139, 246–260.
Yang, J.H., Wu, F.Y., Wilde, S.A., 2003. A review of the geodynamic setting of large-scale Late Mesozoic gold mineralization in the North China Craton: an association with lithospheric thinning. Ore Geol. Rev. 23, 125–152.
Yang, J.H., Wu, F.Y., Wilde, S.A., Belousova, E., Griffin, W.L., 2008. Mesozoic decratonization of the North China block. Geology 36, 467–470.
Yang, Q.L., Zhao, Z.F., Zheng, Y.F., 2012a. Modification of subcontinental lithospheric mantle above continental subduction zone: constraints from geochemistry of Mesozoic gabbroic rocks in southeastern North China. Lithos 146-147, 164–182.
Yang, Q.L., Zhao, Z.F., Zheng, Y.F., 2012b. Slab-mantle interaction in continental subduction channel: geochemical evidence from Mesozoic gabbroic intrusives in southeastern North China. Lithos 155, 442–460.
Yang, X.M., 2012. Sulfur solubility in felsic magmas: implications for genesis of intrusion related gold mineralization. Geosci. Can. 39, 17–32.
Yang, Y.H., Zhang, H.F., Chu, Z.Y., Xie, L.W., Wu, F.Y., 2010. Combined chemical separation of Lu, Hf, Rb, Sr, Sm and Nd from a single rock digest and precise and accurate isotope determinations of Lu-Hf, Rb-Sr and Sm-Nd isotope systems using Multi-collector ICP-MS and TIMS. Int. J. Mass Spectrom. 290, 120–126.
Yang, Z., Hou, Z., Xu, J., Bian, X., et al., 2014. Geology and origin of the post-collisional Narigongma porphyry Cu-Mo deposit, southern Qinghai. Tibet. Gondwana Research 26, 536–556.
Ying, J.F., Zhou, X.H., Zhang, H.F., 2004. Geochemical and isotopic investigation of the Laiwu-Zibo carbonatites from western Shandong Province, China and implications for their petrogenesis and enriched mantle source. Lithos 75, 413–426.
Yuan, S.R., Li, B.F., 1987. The basic characteristics of the volcano structure of the Zouping Basin, Shandong Province. Geol. Rev. 33, 5–11 (in Chinese with English abstract).
Yuan, S.R., Li, B.F., 1988. The characteristics of alteration of the Wangjiazhuang porphyry deposit, Zouping, Shandong Province. Geol. Rev. 34, 36–43 (in Chinese with English abstract).
Zhai, M., Santosh, M., 2013. Metallogeny of the North China Craton: link with secular changes in the evolving Earth. Gondwana Res. 24, 275–297.
Zhai, M.G., Santosh, M., 2011. The Early Precambrian odyssey of the North China Craton: a synoptic overview. Gondwana Res. 20, 6–25.
Zhang, H.F., Sun, M., Zhou, X.H., Fan, W.M., Zhai, M.G., Yin, J.F., 2002. Mesozoic lithosphere destruction beneath the North China Craton: evidence from major-, trace-element and Sr-Nd-Pb isotope studies of Fangcheng basalts. Contrib. Miner. Petrol. 144, 241–253.
Zhang, H.F., Zhu, R.X., Santosh, M., Ying, J.F., Su, B.X., Hu, Y., 2013. Episodic widespread magma underplating beneath the North China Craton in the Phanerozoic: implications for craton destruction. Gondwana Res. 23, 95–107.
Zhang, J., Xu, Z.W., Li, H.Y., Liu, S.M., Yang, X.N., Lu, X.C., Li, H.C., 2008a. The mineralization geochemistry of the Wangjiazhuang copper deposit in Zouping County, Shandong Province, and a discussion on its genesis. Geol. Rev. 54, 466–476 (in Chinese with English abstract).
Zhang, J., Xu, Z.W., Li, H.Y., Liu, S.M., Zhu, B.B., Lu, X.C., Li, H.C., 2008b. Geochemistry and genesis of the ore-bearing intrusions in the Wangjiazhuang copper deposit, Zouping, Shandong Province. J. Nanjing Univ. (Nat. Sci.) 44, 632–641 (in Chinese with English abstract).
Zhang, X.M., Zhang, Y.Q., Ji, W., 2007. Fault distribution patterns of the Luxi Block, Shandong, and Mesozoic sedimentary-magmatic-structural evolution sequence. J. Geomech. 13, 163–172 (in Chinese with English abstract).
Zhang, Y.Q., Dong, S.W., Shi, W., 2003. Cretaceous deformation history of the middle Tan-Lu fault zone in Shandong Province, eastern China. Tectonophysics 363, 243–258.
Zhao, D., Isozaki, Y., Maruyama, S., 2017. Seismic imaging of the Asian orogens and subduction zones. J. Asian Earth Sci. http://dx.doi.org/10.1016/j.jseaes.2017.06.016.
Zhao, G., Cawood, P.A., Li, S., Wilde, S.A., Sun, M., Zhang, J., He, Y., Yin, C., 2012. Amalgamation of the North China Craton: key issues and discussion. Precambr. Res. 222-223, 55–76.
Zhao, G., Wilde, S.A., Cawood, P.A., Sun, M., 2001. Archean blocks and their boundaries in the North China Craton: lithological, geochemical, structural and P-T path constraints and tectonic evolution. Precambr. Res. 107, 45–73.
Zheng, J.P., 2009. Comparison of mantle-derived materials from different spatiotemporal settings: implications for destructive and accretional processes of the North China Craton. Chin. Sci. Bull. 54, 3397–3416.
Zhou, X.M., Li, W.X., 2000. Origin of Late Mesozoic igneous rocks in Southeastern China: implications for lithosphere subduction and underplating of mafic magmas. Tectonophysics 326, 269–287.
Zhu, R.X., Fan, H.R., Li, J.W., Meng, Q.R., Li, S.R., Zheng, Q.D., 2015. Decratonic gold deposits. Sci. China Earth Sci. 58, 1523–1537.
Zhu, R.X., Xu, Y.G., Zhu, G., Zhang, H.F., Xia, Q.K., Zheng, T.Y., 2012a. Destruction of the North China Craton. Sci. China Earth Sci. 55, 1565–1587.
Zhu, R.X., Yang, J.H., Wu, F.Y., 2012b. Timing of destruction of the North China Craton. Lithos 149, 51–60.